Blade Tonal Noise Reduction Using Tail Articulation at High Reynolds Number

by

Daniel Lee Macumber

Submitted to the Department of Mechanical Engineering
in partial fulfillment of the requirements for the degree of

Master of Science in Mechanical Engineering

at the

MASSACHUSETTS INSTITUTE OF TECHNOLOGY

February 2005

Author ....
Department of Mechanical Engineering
January 14th, 2005

Certified by...
Anuradha M. Annaswamy
Senior Research Scientist
Thesis Supervisor

Accepted by ....
Lallit Anand
Chairman, Department Committee on Graduate Students

Blade Tonal Noise Reduction Using Tail Articulation at High Reynolds Number

by

Daniel Lee Macumber

Submitted to the Department of Mechanical Engineering
on January 14th, 2005, in partial fulfillment of the
requirements for the degree of
Master of Science in Mechanical Engineering

Abstract

The biologically inspired method of tail articulation is investigated as a means of reducing tonal noise due to the stator wake blade interaction in underwater vehicles. This work is experimental in nature and conducted in the closed channel water tunnel at Naval Undersea Warfare Center in Newport, Rhode Island. Tail articulation is carried out with a life scale stator model with hinged flapping tail designed to (i) operate in freestream velocities corresponding to Reynolds number in the range 75,000 $< Re <$ 300,000 and (ii) operate at frequencies up to 30 Hz in order to investigate the range of Strouhal number $0.0 < St < 0.35$. Velocity measurements in the active stator wake are carried out by Laser Doppler Velocimetry, LDV, and Particle Image Velocimetry, PIV, in order to investigate the effects of tail articulation. Time averaged measurements of the stator wake by LDV show that Strouhal number of the tail articulation has a dominant effect on the time mean stator drag. Instantaneous phase averaged measurements of the stator wake by PIV show three regimes of the stator wake as Strouhal number is increased; quasi-steady wake spreading, vortex roll up, and strong vortex wake. A low order model describing the creation and convection of vorticity by tail articulation is developed which describes wake phenomena observed in experimental measurements. A two dimensional blade force simulation coupled with the reduced order tail articulation model is used to perimetrically search for a tail motion resulting in lower unsteady blade forces. Finally, a three dimensional unsteady propeller simulation using both experimental wake velocity data by PIV and simulated wake velocity data generated by the reduced order tail articulation model is used to predict the effect of tail articulation on radiated noise. These simulations indicate that reduction of radiated noise by 5 dB or more is possible using tail articulation.

Thesis Supervisor: Anuradha M. Annaswamy
Title: Senior Research Scientist

Acknowledgments

This work is supported by the Office of Naval Research University/Laboratory Initiative project on Active Control of Blade Tonals (N00014-03-0777).

The completion of this thesis is a milestone that I have been working towards for a long time and I could not have made it here by myself. I would like to thank the many people who have helped me to achieve my goal. I would like to thank my advisor, Dr. Anuradha Annaswamy, for her thoughtful and caring direction on this project. I would like to thank Daehyun Wee and Dr. Ahmed Ghoniem for taking the time to answer all of the questions I asked. I would like to thank Dr. Stephen Huyer at NUWC for going above and beyond to adapt the PUF code to my work. I would like thank Dr.'s David Beal and Charles Henoch at NUWC for their insight, sarcasm and countless hours spent in the dark taking pictures of small white dots. I would like to thank MIT for the brief drink from the firehose. I would like to thank my parents and family who gave me every opportunity to succeed until I was ready to seize one on my own. I would like to thank my wife Kathryn for her love, patience, humor, and understanding. You have inspired growth in me where there was nothing before. I would to thank God who has made all things, whose love is perfect and whose strength has carried me.

Ephesians 6:10 Finally, be strong in the Lord and in the strength of His might.

Contents

List of Figures

*Author's Note [1]

---

[1] Many of the figures in this work are difficult to present in the black and white required in this thesis. The reader is invited to request an electronic copy of this thesis from the MIT library for a presentation of the same material in color.

List of Tables

Nomenclature

a, b, c, d Length of bars in four bar mechanism

A Wake width or tail displacement

α Angle of attack

β Blade pitch angle

c_0 Speed of sound

C_d Coefficient of drag

C_l Coefficient of lift

δ Boundary layer thickness, Equation 5.2

D Drag force

e Eccentricity

$ESPL$ Effective sound pressure level, Equation 5.7

f Frequency

F Force

γ Point vortex strength, Figure 5-2

Γ Airfoil bound circulation

G Grashoff number, Equation 2.1

k Reduced frequency, Equation 4.2

L Lift force

$\dot{L}$ Time derivative of lift force

L_{chord} Stator chordlength

L_{tail} Length of hinged tail

$\hat{n}$ Normal direction vector

ν Kinematic viscosity

ω Vorticity, Equation 4.1

Ω Blade rate

P' Acoustic pressure, Equation 1.1

ϕ Potential function

q Point source strength, Figure 5-2

Q Torque

r Radial distance

r_{blade} Radius of propeller blade

r_{ij} Radial distance from j to i

Re Reynold number, Equation 1.3

ρ Density of water

s Airfoil arc length coordinate

S Airfoil span

St Strouhal number, Equation 1.2

$\hat{t}$ Tangential direction vector

T Thrust

θ Angular displacement

u Fluid velocity in the $\hat{x}$ direction

v Fluid velocity in the $\hat{y}$ direction

w Fluid velocity in the $\hat{z}$ direction

U Freestream u velocity

U_{blade} Nominal propeller blade inflow

$\hat{x}$ Direction of the tunnel flow

$\hat{y}$ Direction transverse to the tunnel flow

$\hat{z}$ Direction of gravity

Chapter 1

Introduction

1.1 Background and Problem Definition

The modern SISUP, Swirl Inducing Stator Upstream of Propeller, underwater vehicle consists of a torpedo shaped body with a row of stators mounted upstream of a rear mounted propeller. When turning, the blades of the propeller, or rotor, generate a forward thrust force as well as a torque which tends to spin the vehicle. The upstream stator blades are set to pre-swirl the inflow to the rotor. This counteracts the spin that the propeller induces on the rotor outflow as well as sets an optimal angle of attack between the rotor inflow and the propeller blade. This configuration results in more efficient thrust as less work is done to increase the angular momentum of the outflow and because separation due to high rotor blade angle of attack is avoided. Figure 1-1 is a schematic of a propeller blade section where β is the local blade pitch angle, α the local angle of attack, Ω the blade rate, U the freestream velocity, L the lift force, D the drag force, Q the rotor torque and T is the thrust force used for propelling the vehicle.

If the effect of the stator row were simply to uniformly pre-swirl the inflow into the rotor blades the propeller would generate efficient steady thrust. However, this is not exactly the case. In a viscous fluid, the no slip boundary condition results in a surface drag force on a moving streamlined body. Drag forces on stators, as well as other upstream appendages such as antenna or structural struts, remove energy from

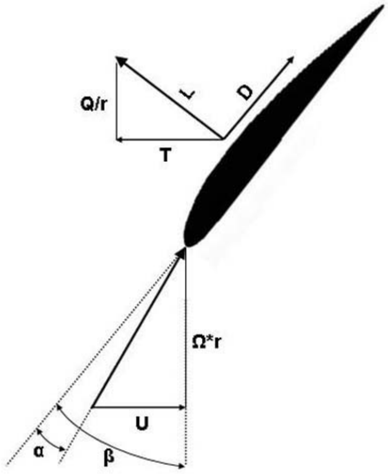

Figure 1-1: Forces acting on propeller blade section

the moving fluid which results in a wake velocity defect that persists downstream. The inflow to the rotor is then nonuniform due to the uneven spatial distribution of upstream appendages. As a propeller blade passes through regions of varying inflow velocity the effective angle of attack on the blade changes and the blade experiences unsteady forces. Unsteady forces on a solid body in a fluid are a source of directly radiated noise [29]. If the most significant unsteady force acting on the propeller blade section is L then the expression for directly radiated noise far from the body may be written:

$$P'\left(\vec{r},t\right) = \frac{1}{4\pi r}\nabla\cdot\vec{F}\left(t - {}^{r}\!/_{c_0}\right) \approx k_0\dot{L} \tag{1.1}$$

where P' is the acoustic pressure, r is the distance from the source to the observer, $\vec{F}$ is the force vector acting on the body, c_0 is the speed of sound in the medium, k_0 is a suitably chosen constant, and $\dot{L}$ is the time derivative of the lift force. Because the motion of the propeller is periodic in time the noise generated by the wake blade interaction is tonal noise at harmonics of the blade passing rate. This component of noise is particularly disadvantageous in military applications as it can be used to identify or locate the vehicle. Unsteady periodic forces are also undesirable as they may excite structural vibrations of the vehicle and contribute to fatigue of the blades and propeller assembly. Noise radiated due to secondary vibrations in the vehicle assembly is referred to as indirectly radiated noise.

Experiments have shown that the stator-wake blade interaction is the primary source of tonal noise on a SISUP underwater vehicle. If the velocity defect due to upstream appendages could be eliminated then the tonal noise emitted would be significantly reduced. Alternatively, if the propeller inflow were controlled correctly then the noise produced could be reduced or altered to confuse identification of the vehicle. Several ideas have been proposed for reducing or altering tonal noise emission in underwater vehicles. SISUP configurations with different numbers of stators than of rotor blades, 7 stators and 9 blades for example, have a theoretical first harmonic of the first multiple of both numbers, in this case 63 times the blade rate. Uneven spacing between stator and propeller blades should also effect the spectrum of radiated noise. However, experiments and simulations have both shown that the primary blade passing rate harmonics tend to come through in both of these configurations. Rapidly modulating the propeller's rate, called dithering, has the potential to reduce tonal noise but results in unsteady propulsive forces. Finally propulsion without propellers, such as biologically inspired propulsion, is an attractive option but must be able to meet all mission criteria.

1.2 Biomimetic Tail Articulation

The ease and effectiveness with which swimming animals use fins for propulsion and trajectory control have led scientists to believe that the motion of a fish's fin is well tuned to optimally interact with the surrounding fluid. There exist many different types of fish swimming which are well classified but can generally be broken down into two categories; Body and/or Caudal Fin (BCF) or Median and/or Paired Fin (MPF) [35]. BCF swimming is the most common type of fish propulsion in which the fish's caudal fin and portions of the body undergo an undulating motion [21]. Eels wiggle with a wavelength shorter than their bodies, pushing an added mass of fluid backward along their bodies. Other fish, such as tuna, employ BCF swimming with wavelengths longer than their bodies, relying on the formation of vorticity for propulsion. The majority of fish use BCF motions as their primary thrust mechanism. MPF motions, on the other hand, employ the pectoral, dorsal and other fins. These fins are often capable of a wide range of active deformations and precise trajectories which enable fine fluid manipulation through complex hydrodynamic interactions. MPF motions are generally used for swimming at low speeds, maneuvering or stabilization rather than for primary propulsion.

Engineering efforts have been made to replicate the motions of swimming fish in order to exploit the same fluid interactions that fish use so effectively. Much of this work has focused on the use of fins oscillating in pitch and heave for efficient propulsion and has been modelled after BCF swimming. Propulsive forces and efficiencies of hydrofoils moving in both heave and pitch have been studied extensively [2], [28], [10]. A key result of this work has been the identification of a nondimensional number common to many types of oscillating propulsive motions. The Strouhal number, St, is defined as:

$$St = \frac{fA}{U} \tag{1.2}$$

where f is the frequency of vortex formation in the wake and A the width of the wake. The Strouhal number provides a measure of the relative spacing of vortices in the wake. In the classic example of vortex shedding by a cylinder, St with A defined as the diameter of the cylinder rather than wake width remains constant at 0.2 over a large range of flow speeds. Studies have shown that a large range of fish and swimming animals beat their tails in a common range of St, namely $0.25 < St < 0.35$ [34]. It was also found in [32] that a wide range of bats, birds and insects beat their wings in this same range of St as fish during cruising flight. Experimental tests have shown that flapping foils produce their most efficient thrust when operating in this range of St [34]. This observation has emboldened engineers to replicate the BCF mode of swimming as means of propulsion in several vehicles from a motorized version of a bluefish tuna [3] to plans for an ocean-liner powered by flapping foils [33].

However, the aim of this project is not to replace the propeller as the primary means of propulsion in the typical AUV vehicle. The SISUP propeller is a well developed technology and is effective for many types of missions. Rather, the inspiration from biology in this project is to add extra fins to the vehicle which are not used primarily for propulsion but for noise control. This is a weak corollary to the addition of specialized MPF fins for auxiliary purposes in fish biology. A schematic of the proposed addition of a tail affixed to the trailing edge of the stator blade is shown in Figure 1-2.

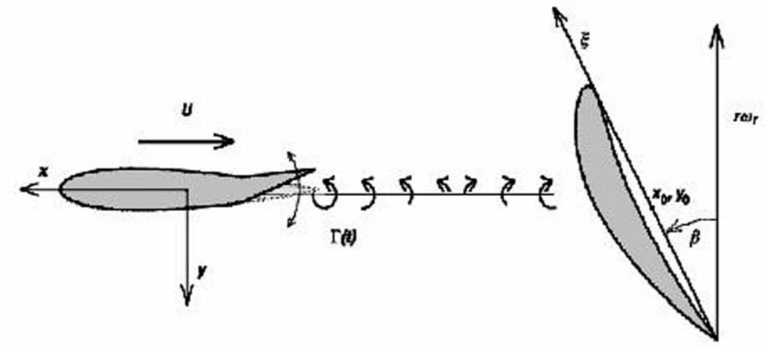

Figure 1-2: Tail articulation for blade tonal noise reduction

1.3 Previous Research

The use of the tail articulation for blade tonal noise reduction was first proposed and studied numerically by W. Krol et. al [20]. Krol modelled tail articulation as an arbitrary vorticity source at the stator trailing edge and the shed vorticity was assumed to convect with the freestream velocity. With these assumptions a second order differential equation describing the propeller lift due to vorticity in the wake was written and solved with $\dot{L}$ set to zero. The ideal vorticity input computed by this model was of a general nonsinusoidal, nonperiodic form and the noise reduction predicted was significant.

D. Opila performed experimental measurements of the effect of tail articulation on a stator wake [26], [27]. Point measurements by hot film anemometry in an open channel water tunnel showed that tail articulation is capable of reducing the wake deficit behind a stator blade up to 60%. Defining St with A as the maximum tail tip deflection rather than wake width, Opila found that optimal wake reduction by sinusoidal motion also occurs in the range of $0.25 < St < 0.35$. Furthermore, Opila showed that tail motions based loosely on the optimal vorticity input found by Krol proved more effective at wake reduction than sinusoidal motions. Due to limitations with the experimental apparatus these measurements were made at low speeds, $U = 4$ cm/s, and correspondingly low Reynolds number, $Re = 4{,}000$. The Reynolds number is an important dimensionless number for a large variety of fluid problems and is defined as:

$$Re = \frac{Ul}{\nu} \tag{1.3}$$

where l the associated length scale and ν the kinematic viscosity of the fluid. The Reynolds number provides a ratio of viscous to inertial forces in the fluid. At lower Re large scale viscous forces are more important than at higher Re and a transition from laminar to turbulent flow is associated with increasing Re.

Opila also investigated the potential for the use of conducting polymer, CP, actuators for tail articulation. These type of actuators have many advantages over traditional actuators in their lower weight, cost, mechanical complexity and self noise. However, at the time of Opila's work CP technology was not advanced enough to meet the basic force, displacement, and bandwidth requirements of tail articulation. Therefore, while Opila was successful at creating flapping actuators out of CP materials, the tail articulation in his experiments was carried out by a stepper motor.

Chapter 2

Tail Articulation Experiment

2.1 Experimental Concept

The experimental work at low *Re* by Opila [26], [27] confirmed that tail articulation is able to reduce the wake deficit behind the stator. Because the wake deficit blade interaction is responsible for tonal blade noise Opila hypothesized that tail articulation may also be able to reduce tonal noise. However, Opila's calculations did not show as large of a potential for noise reduction as that presented in the numerical work of Krol et. al [20]. This result is not surprising as Krol's work was based on an overly simplified model of tail articulation. The work by Opila was therefore a step in the right direction towards using tail articulation for noise reduction on a real vehicle, however an equally large step remains. It is unknown if the wake reduction reported by Opila was due mainly to viscous fluid forces which will be greatly reduced at the significantly higher *Re* most AUV vehicles operate at. Therefore, this experimental work will attempt to extend the work of Opila to more realistic operating conditions in order to test the applicability of tail articulation to real vehicles. A second goal of this research is to gain greater understanding of the effect of tail articulation on the stator wake. This information is necessary to fill in the final missing block in Krol's model, the one between tail motion and distribution of wake vorticity. Both Opila and Krol assumed that vorticity in the wake would simply propagate downstream with no wake alignment. This is known to be incorrect, but the extent of vortex interaction in the flow regimes of interest is unknown. Instantaneous measurements of the flowfield behind the active stator will be necessary to characterize the interactions of vortices in the wake. Because of the complex nature of three dimensional vortex interaction and difficulty of three dimensional flowfield measurement, a two dimensional analysis is preferred and the experiments are to be designed accordingly.

At the time this experiment was planned CP technology was still not advanced enough to provide the necessary actuation, especially with higher flow speeds leading to higher force and bandwidth requirements. Therefore, emphasis will not be placed on use of polymer actuators in the current experiments. It is hoped that continuing improvements in CP technology, along with the better understanding of tail articulation gained through this experiment, will lead to the final integration of a polymer actuator for tail articulation.

2.2 Experimental Facility

The first stage of the experiment design process was to identify available water tunnel facilities capable of high speed flow. The Marine Hydrodynamics Laboratory at MIT has a water tunnel with a 20" square cross section and a maximum flow speed of 30 ft/s. The Naval Undersea Warfare Center in Newport, Rhode Island, NUWC-NPT, has a research water tunnel with a 12" square cross section and a maximum flow speed of 30 ft/s. Both facilities are equipped with closed loop velocity control and have removable plexiglass windows for tunnel access. With access to both facilities it was decided that any design should accommodate both tunnels for maximum flexibility in testing. However, due to the heavy volume of research at MIT all tests were carried out at the NUWC facility.

The NUWC water tunnel slowly expands in the downstream direction to account for boundary layer growth on the walls, minimizing the acceleration of fluid in the 10' long test section. The tunnel has a 3:1 ratio contraction section and a 6" thick honeycomb mesh with 0.25" cells, giving a 0.5% maximum turbulence intensity in the center of the tunnel. The tunnel is powered by a 24" single stage impeller with a 600 Hp electric motor. Two 3500 gal water storage tanks, one for fresh water and the other for salt, are used for filling and draining the tunnel. The tunnel must be thoroughly flushed after any saltwater runs to avoid contamination.

2.3 Setting Experimental Parameters

In order to compare this work to Opila's an uncambered hydrofoil with a 1/3 chordlength trailing edge flapping section was again chosen for the stator model. However, in order to increase the baseline wake deficit, which becomes thinner as Re increases, a thicker NACA 0020 profile was chosen. The apparatus was designed with future tests in mind, the most important of which being the eventual test with a force instrumented propeller behind the flapping stator. The sponsor asked that the stator span only one half of the test channel, so that it is possible to pass one blade of a two bladed propeller through the stator wake at a time. This constraint along with the 12" test section limited the stator's maximum span, S, to 6".

A ratio of S to chordlength, L_{chord}, of 6:1 is preferred for two dimensional approximations in flapping foil experiments [4]. However, the constraint on S from tunnel size would require L_{chord} of 1" and tail length, L_{tail}, of 1/3". Building a working mechanism at this scale would have proven difficult. Instead L_{chord} of 3" and L_{tail} of 1" were chosen, leading to ratio of S:L_{chord} of only 2:1. While this ratio is less than ideal, it is a reasonable compromise as long as three dimensional effects are experimentally verified to be minimal before continuing the two dimensional wake assumption. Re of approximately 300,000 was given as realistic operating condition by the sponsor. With the L_{chord} fixed, it is possible to calculate Re as a function of freestream velocity, U, Table 2.1.

U (m/s)	1	2	3	4
Re	75,000	150,000	225,000	300,000

Table 2.1: Re as a function of U (m/s)

The range of $0.25 < St < 0.35$ was assumed to be of interest, with St again defined with A as the tail tip deflection rather than the wake width. For a specified St the set of U, f and A loses one degree of freedom and a choice of two parameters determines the value of the third. U was set by the requirements on Re and A was desired to be less than 20 degrees as large tail deflections may involve very different fluid interactions, such as massive separation. The only experimental parameter left is f and it is fixed by the previous parameters. Table 2.2 shows f as a function of U and A with St set to 0.25.

	U (m/s)			
A (deg)	1	2	3	4
5	56.5	112.9	169.4	225.9
10	28.3	56.7	85.0	113.4
20	14.4	28.8	43.2	57.6

Table 2.2: f (Hz) as function of U (m/s) and A (deg) for $St = 0.25$

2.4 Experimental Apparatus

2.4.1 Actuator

It was recognized that the desired tail frequencies computed in Table 2.2 were quite high and would be a challenge to meet. Opila found wake reduction to be mainly St dependent but this assumption must be tested again at higher Re. For this reason at least one change in levels of U and A in the optimal St range was required. Therefore, the absolute minimum frequency requirement was chosen to be the second lowest frequency in Table 2.2, $f = 28.8$ Hz. The design process started by looking for actuators capable of providing the authority to complete a desired move profile at the minimum required frequency. The most generic desired move profile is of the form:

$$A = sin(2\pi f t)$$

With this move profile maximum velocities are proportional to the operating frequency and maximum accelerations to the square of the frequency. The simplest and first actuator arrangement considered was an electric motor with its shaft rigidly coupled to the tail. In this arrangement the motor controller simply drives the motor to match the desired tail output. However, no stepper motors or servo motors were found capable of the torque necessary to oscillate ± 20 degrees at 28.8 Hz, even with no external inertial load. Gear ratio reducers, which are typically used to increase torque while reducing speed were not feasible because the oscillatory motion requires high velocities. The opposite device, a gear ratio increaser, is capable of reducing torque to increase velocity. However, small errors in motor position relate to large errors in tail position and so a gear increaser was not chosen. Finding that meeting the frequency requirements with a directly coupled motor was very difficult, an alternative approach was considered.

Mechanical devices have been designed to perform specialized computation for centuries and remain useful even in the age of digital computing. The crank rocker is a two dimensional mechanical system consisting of four bars connected by pin joints, with one bar fixed to the ground, shown in Figure 2-1.

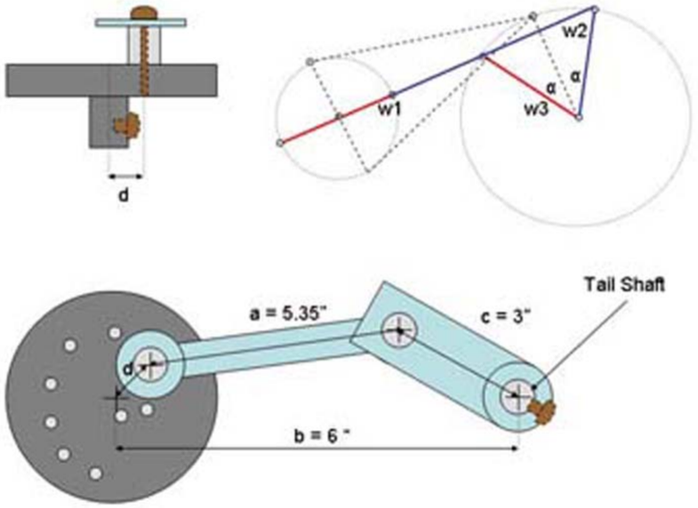

Figure 2-1: Schematic of four bar linkage

This system has four degrees of freedom (x and y for each joint) with three links, each capable of resisting force in one direction. With one more degree of freedom than constraints the crank rocker is an unstable mechanism. This means that it is free to deform in one direction without causing strain in any of the four bars. The direction of this deformation is a function of the position of the four bars and is termed a mechanism of deformation. The most important measure of a crank rocker device is the Grashof condition, G, of the system which is defined as:

$$(b + d \leq a + c) \Rightarrow G \tag{2.1}$$

where b is the length of the longest bar, d is the length of the shortest bar and a, c are the lengths of the two intermediate bars. If the Grashof condition is not met for a four bar linkage, then no link will be capable of making a complete revolution with respect to the ground plane. However, if G is met then at least one link will be capable of making a full revolution with respect to the ground plane. Further, if the longest bar is the one fixed to the ground, then the shortest bar is the one capable of a full rotation. In this configuration the angle of the output link is a periodic function of the angle of the shortest, or input, link. It is possible to pick a configuration of bar links for which this function is a sinusoid about a mean value with amplitude less than 45 degrees. However, machining four separate links for each flapping amplitude to be tested would have proven costly and time consuming. Therefore, it was decided to make link d the only adjustable link and pick fixed values for bars a, b, and c which best preserved the sinusoidal relationship for all values of d, which is the shortest link. Link b, the longest link, was set to 6" in order to fix the physical length scale to one that was easy to work with yet not overly large in order to reduce the inertia of the moving links.

a	b	c	d
5.35	6.00	3.00	$d(A)$

Table 2.3: Length (in) of the four bars in crank rocker mechanism

With these values for links a, b and c the best value for d was calculated for various desired values of A. The eccentricity of the motion, e, was defined as the angle of the output link at the maximum position minus the angle at the minimum position. This is a measure of the deviation of the actual motion from the desired sinusoidal relationship and is less than 5% for all cases.

A (deg)	5	10	15	20	25	30	35
d (in)	0.261	0.520	0.776	1.026	1.268	1.500	1.718
e (deg)	-0.269	-0.481	-0.556	-0.430	-0.017	0.791	2.108

Table 2.4: Length of adjustable link d (in) and eccentricity e (deg) as function of A (deg)

Instead of machining separate input links for each of the cases in Table 2.4 an equivalent input link was made as a circular part with holes drilled at varying radii to set the length of link d. In this design the inertia of link d is maximized while the inertia of links a and c are minimized. An aluminum mounting plate was made with two bearings, one for the motor shaft and one for the tail shaft, to set the length of link b. The motor bearing also removes side loads from motor shaft, which is critical for the motor life. Because the angle of the output link is periodic with the angle of the input link, a constant angular velocity of the input link corresponds to a constant frequency flapping motion. Therefore, for steady state sinusoidal flapping the requirements for the motor became a constant speed requirement, with the motor torque to be maximized in order to accelerate the inertia of links a and c. It was also seen that while active control of the motor velocity can modulate the flapping frequency, the four-bar characteristics fix the flapping amplitude. The two singular positions of the crank rocker also make reversals in direction to obtain arbitrary amplitude flapping difficult to plan. Therefore, the crank rocker mechanism, while useful for sinusoidal motions, is not versatile enough to perform the nonsinusoidal motions that Opila found to increase wake deficit reduction. For this reason it was decided to use a servo controlled motor which would be able to provide the high speeds necessary for very fast sinusoidal motions with the crank rocker, but also perform nonsinusoidal motions at lower speeds while directly coupled to the tail. It was now possible to pick a motor that could exceed the revised specifications. A Kollmorgen Goldline XT brushless servo motor was selected with a maximum speed of 6000 rpm and a continuous stall torque of .44 Nm. Because the motor was not connected directly to the output shaft while using the crank rocker, the actual flap angle was measured with a Stegman C16 2000 point per revolution encoder. A National Instruments 7344 motion control card with four channels of servo/stepper control was chosen to drive the motor as well as read the tail encoder position. This control card was chosen because it provides several auxiliary channels of A/D and D/A conversion as well as the capability to control more than one motor at once. This capability will be useful in the final propeller interaction test.

2.4.2 Stator with Tail Flap

After selecting an appropriate motor and control hardware the task of designing a stator with a flapping tail remained. The first step was to determine how best to machine a hydrofoil with specific NACA 0020 profile and hinged tail flap. Bending of sheet metal, similar to the way that real airplane wings are made, was attractive because it is inexpensive and would allow multiple stators to be constructed easily. However, this method was decided against after considering the task of preventing flow through the airfoil. Rapid prototyping methods such as Stereolithography or Selective Laser Sintering were also considered. However, many of the materials used in these processes were not compatible with water, were too soft, had poor tolerances or were unsuitable in other ways. In the end wire Electrical Discharge Machining, wire EDM, was chosen as the method for fabricating the stator and tail. Wire EDM is a relatively expensive material processing method, but it is precise and able to cut intricate designs. This was important in order to minimize the gap between the stator and tail as well as to machine a very sharp trailing edge to reduce additional viscous effects. The stator and tail were machined from a single block of 6” aluminum. The parts were hard anodized after production to protect the thin layer of aluminum oxide which prevents the aluminum from rusting. While hot pink or green parts would have been attractive, the color black was chosen to decrease laser reflection safety hazards in the laboratory. The stator and tail were custom made to print by PC Machine Shop of Manchester, NH; Appendix B.

After designing the stator, tail and crank rocker mechanism it was necessary to modify an existing plexiglass water tunnel window in order to mount the system to the water tunnel. The 2' head of water above the tunnel test section pressurizes the water inside the tunnel section, causing water to flow out of cracks in the tunnel. Therefore, a low friction water tight seal around the tail shaft hole in the water tunnel plate was desired to prevent leaks. Designers who had previously worked with the water tunnel suggested that a very precise seal is not necessary as the pressure inside the water channel drops by Bernoulli's equation as the freestream velocity increases. They suggested using a crude seal around the tail shaft and running the tunnel constantly while filled to prevent leaking. A 1/16" thick piece of rubber cut by razor blade to the shape of the airfoil with an oversized hole stamped out for the tail shaft was used as a seal between the airfoil and tunnel window. With this imprecise seal it is important to always mount the plate on top of the water tunnel to prevent leakage through the tail shaft opening. The entire assembly fit together on the water tunnel on the first try, a computer model of the assembly is shown in Figure 2-2. However, it was apparent that the shaft was over constrained as it had to be forced somewhat to fit through the three bearings. This was a design flaw that could be corrected by replacing part of the shaft with a flexible connection, however this has not been done at this time.

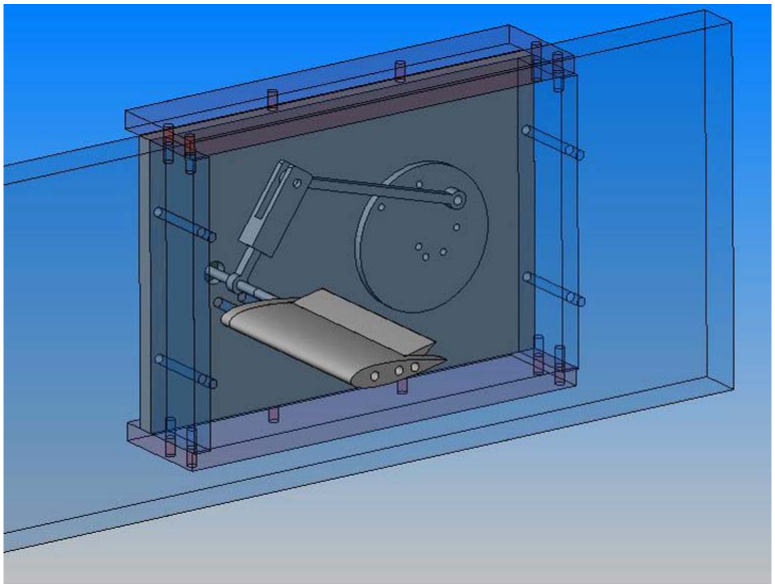

Figure 2-2: Computer design model of the active stator assembly

Chapter 3

Wake Velocity Measurements with Tail Articulation using LDV

3.1 Theory

Fluids have several physical quantities such as temperature, pressure, and velocity; measurement of these quantities may give insight into a particular fluid phenomenon. Because the wake velocity defect behind the stator is directly responsible for unsteady blade forces it is reasonable to measure the velocity field behind the active stator to quantify the potential for noise reduction. If the two dimensional flow assumption made in Chapter 2 holds true, then only two orthogonal components of velocity must be measured to understand the flow behind the tail. Furthermore, tail articulation is a dynamic process and when measuring unsteady flow characteristics it is desired to use a sensor with response time much faster than changes in the flow. Hot-wire anemometry was used by Opila [26] to make velocity measurements in the wake of the active stator. In this technique a wire is held at a constant temperature and fluid velocity is inferred from the rate that heat is convected away by the moving fluid. Specially designed probes can measure two components of velocity with very fast response times and this technique is appropriate for measurements of the stator wake. However, hot-wire anemometry requires physically placing the probe into the region of interest in the fluid. This is prohibitively difficult to do in the closed channel water tunnel. For this reason laser measurement techniques, which have become prevalent in measurements of unsteady fluid behavior, will be used in this work. Two separate laser measurement techniques are available at NUWC and will be used to study velocity in the wake of the active stator in these experiments. The first technique, presented in this chapter, is used to measure two components of velocity at a single point. The second technique, presented in Chapter 4, is able to capture two components of instantaneous velocity over a two dimensional grid.

Laser Doppler Velocimetry, LDV, is a non-invasive fluid velocity measurement technique made possible by the invention of continuous wave gas lasers [8]. The technique works by inferring fluid velocity from the measurement of the Doppler frequency shift in light reflected off of a moving particle carried along by the fluid. Two laser beams of the same frequency are made to intersect at their thinnest beam diameter. These beams interfere with each other, creating a line of alternating fringes of light and dark. The spacing of these fringes is a function of the beam convergence angle and the wavelength of the laser light. When a particle randomly passes through this beam intersection, called the measurement volume, a burst of light is reflected as the particle moves between the fringes. The velocity of the particle determines the frequency of the alternating light and dark reflections, which are collected by a photomultiplier. Because the fringes are aligned in one direction, only one component of the particle velocity is measured by each laser pair. Multiple components of velocity can be measured in the same volume by using laser beams of different color for each velocity component and filtering by color at the photomultiplier. Negative velocity would normally result in a negative frequency shift and this cannot be differentiated from a positive shift of the same magnitude. However, slightly increasing frequency with a Bragg cell in one of the intersecting laser beams creates a beating pattern of the fringes in the measurement volume, eliminating directional ambiguity. Modern signal processing techniques allow the velocity of the particle to be determined accurately with the burst signal even if the particle moves quickly out of the measurement volume or accelerates through it. A large number of random burst measurements must be taken before the LDV measurement becomes statistically meaningful and these statistics are estimated as the measurement progresses. If a large enough set of bursts are recorded at random sampling times then the frequency spectrum of variations in the flow velocity may also be estimated.

3.2 LDV Hardware

The LDV measurement system at NUWC consists of a Lexel 10 watt continuous Argon-Ion laser, a Dantec 55X35 color separator and fiber manipulator, a 60 mm Dantec FiberFlow probe head, two Dantec 57X08 photomultipliers, two Dantec 57N11 BSA signal processors, and the required Dantec BSA Flow Software. The light from the laser is split into two components, blue and green, by the color separator and then focussed into fiber optic polarization preserving cables leading to the probe head. The blue light has a wavelength of 488 nm and the green light a wavelength of 514.5 nm. The probe head is factory aligned with a beam spacing of 38 mm, beam diameter of 1.35 mm, and focal length of 400 mm. These parameters create a measurement volume at the focal length which is an ellipsoid 4.1 mm long in the laser axis direction and 0.19 mm wide in the two measurement directions. Light reflected off of particles in the measurement volume is collected and amplified by the photomultipliers before being processed by the BSA units. The probe head is mounted to a three axis traverse system which allows the laser head to be accurately positioned in order to measure velocity at different volumes in the tunnel. The software is used to configure the BSA units, control the traverse movement, and record velocity data from the BSA units after each measurement point.

3.3 Experimental Procedure

Before taking LDV measurements the traverse axes were first aligned to the water tunnel. This step is necessary to relate the traverse coordinate system to the flow coordinate system, which is of interest. The fluid coordinate system is defined with $\hat{x}$ in the direction of the tunnel flow, $\hat{y}$ transverse to the tunnel and $\hat{z}$ downwards in the direction of gravity. The origin was chosen to be halfway down the stator at the trailing edge. Shims were used to level the traverse, aligning the $\hat{z}$ axis with the tunnel. To parallel the traverse to the tunnel in the $\hat{x}$ direction, the traverse was repeatedly moved back and forth through its full travel in the $\hat{x}$ direction. The table was adjusted until the traverse measured an equal distance to the tunnel at the maximum and minimum x positions. Once the traverse was correctly aligned the wheels of the table were locked in place to prevent the table from moving. The LDV system used is shown in Figure 3-1.

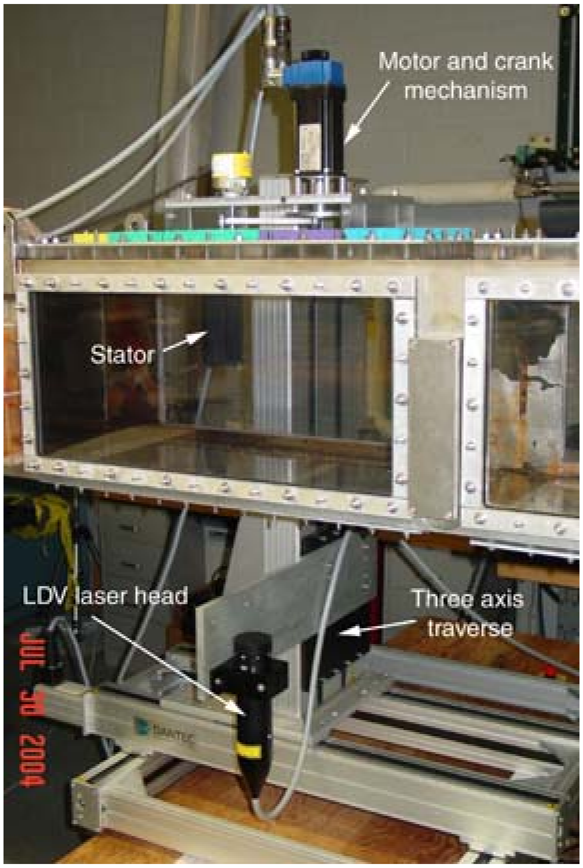

Figure 3-1: LDV setup

After the stator was installed in the test section the water tunnel was filled. Valves at both ends of the tunnel were opened while filling to allow trapped air to escape and then closed to prevent air from entering back into the tunnel. Before the tunnel was filled to the top of the test section the flow was seeded with approximately 200 mL of a solution containing 3M Scotchlite glass micro spheres. These particles are neutrally buoyant, white in color and the particle size is a distribution with mean diameter of 40 μm and an upper 95% limit of 120 μm. The laser is installed on a circuit which requires interlocks on the doors of the test facility be closed before the laser can be turned on. Before any tests can proceed all doors to the laboratory are closed and safety warning signs are posted.

3.4 Tunnel Calibration

The NUWC water tunnel's electric motor is equipped with closed loop velocity control which maintains the motor's rotational speed at a set value. It was necessary to calibrate the freestream velocity in the experimental section to the tunnel motor's speed. To do this LDV measurements were taken in the middle of the section used for the flapping experiment with no apparatus installed. The tunnel was started and run at 150 rpm while the LDV probe was carefully rotated until the u component of velocity measured was maximized, aligning the probe axis with the tunnel flow. During calibration, measurements were taken over 100 seconds in an attempt to catch any medium to low frequency oscillations in the freestream velocity, none were noted. After each measurement the tunnel speed set point was changed to a new value and the tunnel was allowed 5 minutes to come to full speed before the next measurement began. The relationship between tunnel speed and U was quite linear over the range 25-550 rpm, Figure 3-2. The slope of the line in Figure 3-2 is 0.0143 (m/s)/rpm. The LDV measurements were in close agreement with a previous tunnel calibration taken with static pitot tube measurements. However, the linear best fit line to the tunnel calibration did not pass through the origin but instead through U = -0.06 m/s at zero tunnel speed. This implies that viscous effects become important at low speeds and the relationship is no longer linear. The turbulent RMS velocity was found to be approximately 0.5% for each tunnel speed measured.

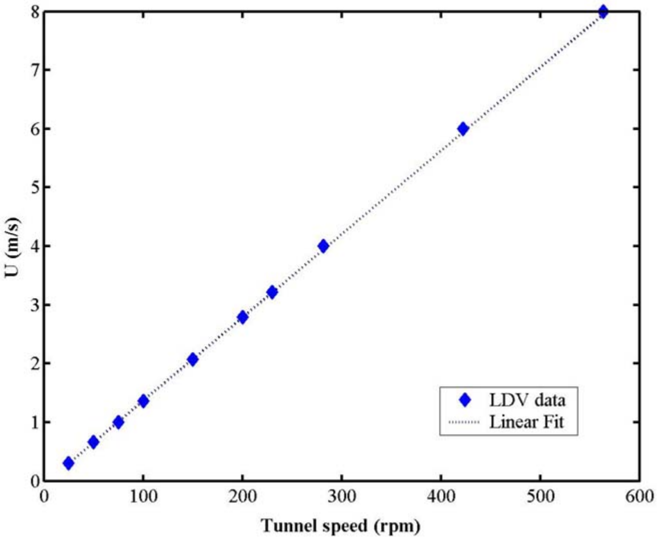

Figure 3-2: U (m/s) vs tunnel speed (rpm)

3.5 Baseline Measurements

The first step in this experiment was to test the two dimensional assumption in the flow behind the flapping stator. To do this the LDV system was initially positioned underneath the tunnel, recording the u and w components of velocity. The crank mechanism was set for $A = 10$ degree sinusoidal motions and the tail was flapped at f up to 1252 rpm. In each case the wake was measured one chordlength downstream for 100 s before the traverse was moved through 25 points in the $\hat{y}$ direction. At this stage, it was assumed that the wake was symmetric about the stator, therefore only half of the wake was measured. This assumption was disregarded in subsequent measurements after asymmetries in the wake were noticed. The maximum normalized w/U component of velocity in the active wake was found to be between 1-2% for each case, allowing for a two-dimensional analysis.

After the two dimensional assumption was shown to be valid in the wake of the flapping stator the LDV traverse was set up to measure the u and v components of velocity. To do this the LDV system was repositioned to point in from the side of the tunnel. The baseline stator wake across the tunnel was measured at four tunnel speeds, Figure 3-4. The wake deficit due to a static tail deflection A of 5, 10, and 20

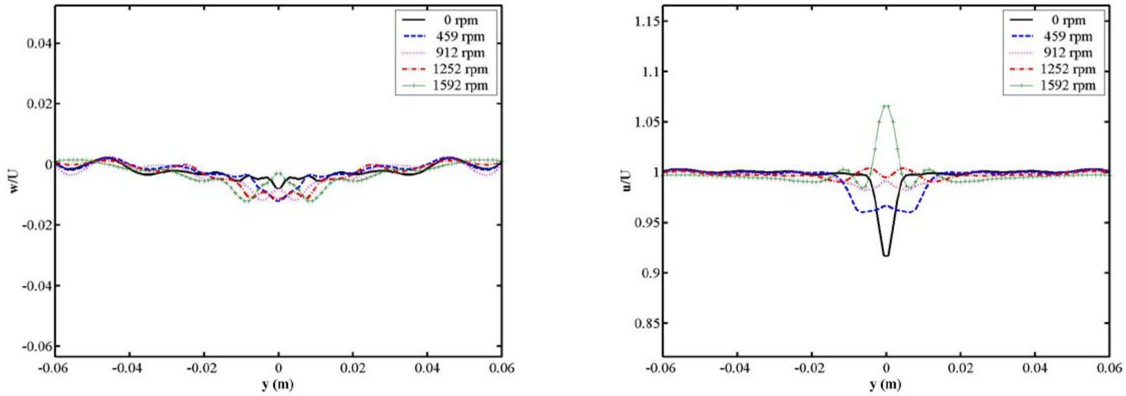

w/U u/U

Figure 3-3: Active wake recorded from underneath tunnel for $A = 10$ (deg), $U = 1$ (m/s) and varying f (rpm)

degrees was also measured in Figure 3-5.

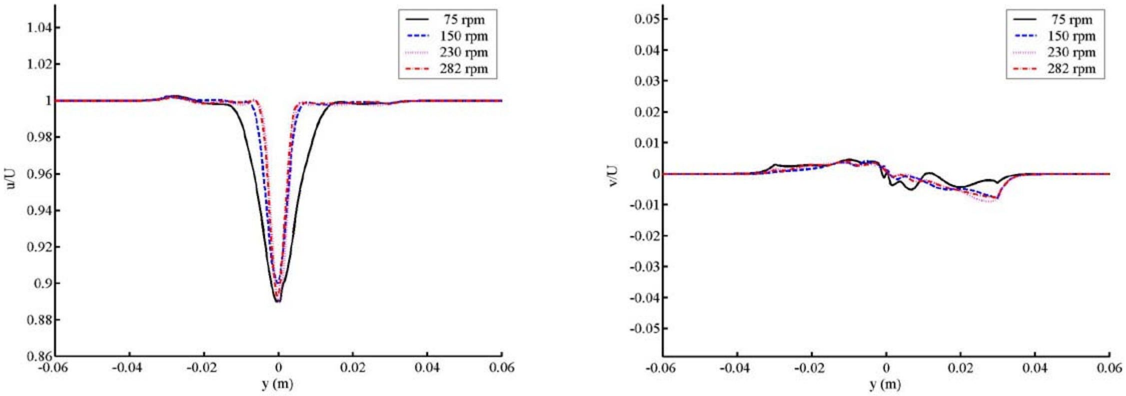

u/U v/U

Figure 3-4: Baseline wake for varying tunnel speed (rpm)

3.5.1 Frequency Domain Measurements

As previously mentioned, the LDV measurement system is able to provide an estimate of the frequency spectrum of the wake velocity components measured. In the baseline measurements a spike in the spectrum at 50 Hz was noticed at low flow speeds. This frequency did not noticeably shift with changes in U at low speeds but would suddenly disappear at flow speeds above $U = 1.5$ m/s. This possibly indicates that at low speeds

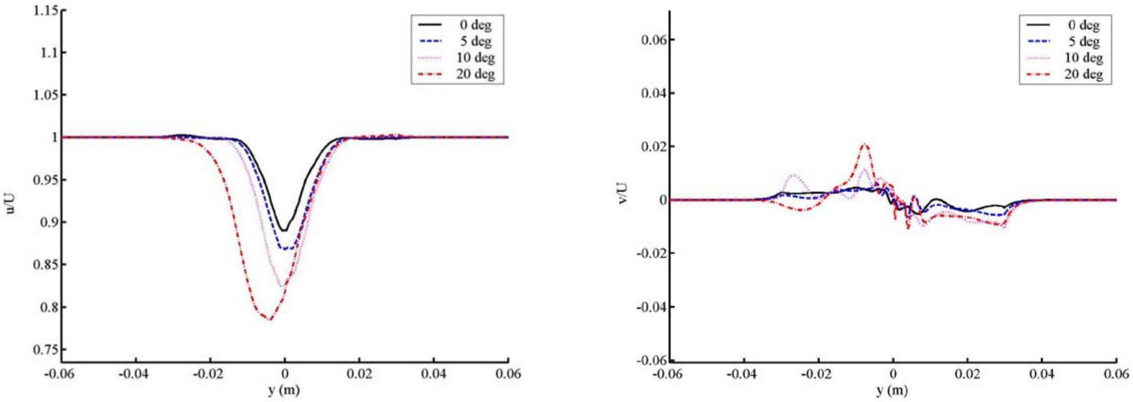

u/U v/U

Figure 3-5: Baseline wake for varying static tail deflection A (deg)

the stator has a preferred shedding frequency which disappears around 1.5 m/s as the flow transitions to fully turbulent. This transition may explain why the normalized baseline wake at $U = 1$ m/s appears wider than those at $U = 2$ or 4 m/s.

3.6 Active Articulation Measurements

3.6.1 Sinusoidal Move Profiles

Investigation into the wake due to tail articulation began with the sinusoidal move profile. Because tests at this Re had not been made before it was not possible to make any assumptions about St dependence. Therefore, the experimental parameters to be varied became f, A, and U. Several levels for each of these factors were chosen in hopes of capturing any interesting behavior in the wake that might occur. The full factorial experimental design was chosen to avoid making assumptions about coupled effects between experimental factors. These three separate degrees of freedom resulted in a fairly large experimental plan with 63 test cases. Each factor and the levels tested are shown in Table 3.1. The levels of f tested were chosen to have certain frequency beating characteristics which are discussed in Chapter 4.

At this point in the project it became necessary to develop a naming system which could uniquely define each experimental case in order to store experimental data

f (rpm)	0	112	225	459	912	1252	1705
U (m/s)	1	2	3	4			
A (deg)	5	10	20				

Table 3.1: Experimental levels of f (rpm), A (deg) and U (m/s)

efficiently. This naming convention is *rpm*deg*tunnel, where rpm corresponds to f (rpm), deg corresponds to A (deg) and tunnel corresponds to the tunnel speed (rpm). Unless otherwise noted in the filename the tail motion is assumed to be a sinusoid driven by the crank rocker mechanism. A name of 0rpm0deg150tunnel corresponds to a non-flapping case with zero steady state tail deflection and a tunnel speed of 150 rpm. A name of 912rpm10deg75tunnel corresponds to a sinusoidal flapping case with frequency of 912 rpm, maximum tail deflection of 10 degrees and a tunnel speed of 75 rpm. Because the freestream velocity in the NUWC water tunnel proved to be repeatable the tunnel speed may be used interchangeably with the corresponding freestream velocity value. The levels of tunnel speed used and the corresponding U values are given in Table 3.2.

tunnel speed (rpm)	75	150	230	282
U (m/s)	1	2	3	4

Table 3.2: Levels of tunnel speed (rpm) and corresponding U (m/s)

Because LDV is a point measurement technique the time required to test each case in the experimental matrix scales with the number of points measured in the wake for each case. This makes LDV an inefficient choice for measuring velocity on two dimensional grids but relatively efficient at measuring line profiles as in Figures 3-3 and 3-5. In addition, synchronization between the LDV measurement and the tail position, so that data is recorded only when the tail was in a certain portion of its motion, was not possible with the equipment available at NUWC. Therefore, the role of LDV in this research was to identify regions of interest in the tail articulation matrix by taking time mean line measurements of the stator wake. This data allows for insight into the overall effect of tail articulation, which is then used to reduce the experimental matrix necessary for the more time consuming PIV measurements in Chapter 4. Data was analyzed as the LDV experiment proceeded and the LDV experimental plan was adapted to fill in between points where the wake varied quite a bit. The amount of data collected in these tests is too great to be fully presented here. Instead a limited but indicative set is presented. Figures 3-6 through 3-8 show the effect of sinusoidal tail articulation on the normalized u/U and v/U components of the stator wake. It is seen that the u/U component remains relatively symmetric about the stator and that the wake deficit decreases as f increases. Then at some critical frequency the wake deficit is almost entirely removed and at even higher f the deficit becomes reversed. This effect is roughly the same for all levels of A, however the width of the wake is dependant on A. It is also seen that the v/U component of the wake is asymmetric and becomes significant as the tail frequency is increased. Finally, the effect of increasing U, which is not shown here, results in somewhat thinner wakes due to the thinner boundary layers, similar to Figure 3-4. The u/U and v/U progressions at higher U are similar to Figures 3-6 through 3-8, except that the wake reversal occurs at higher f and St as U is increased.

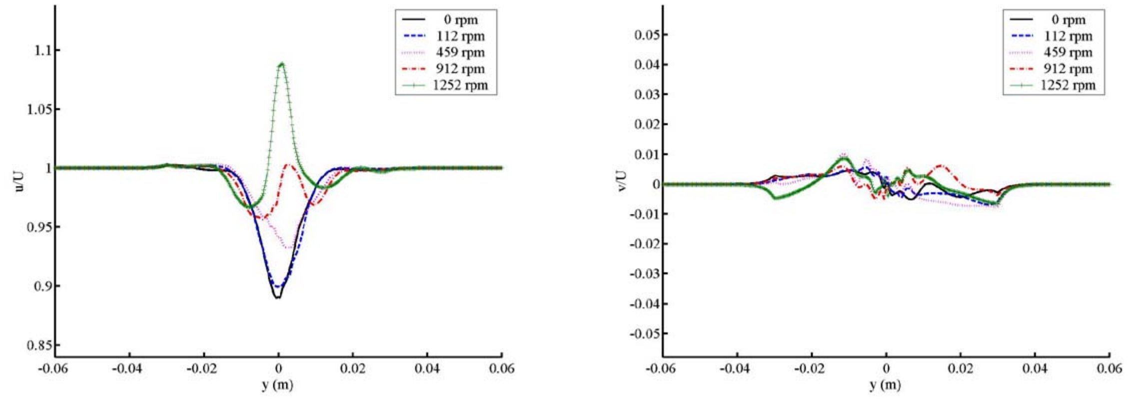

u/U v/U

Figure 3-6: Active wake for $A = 5$ (deg), $U = 1$ (m/s) and varying f (rpm)

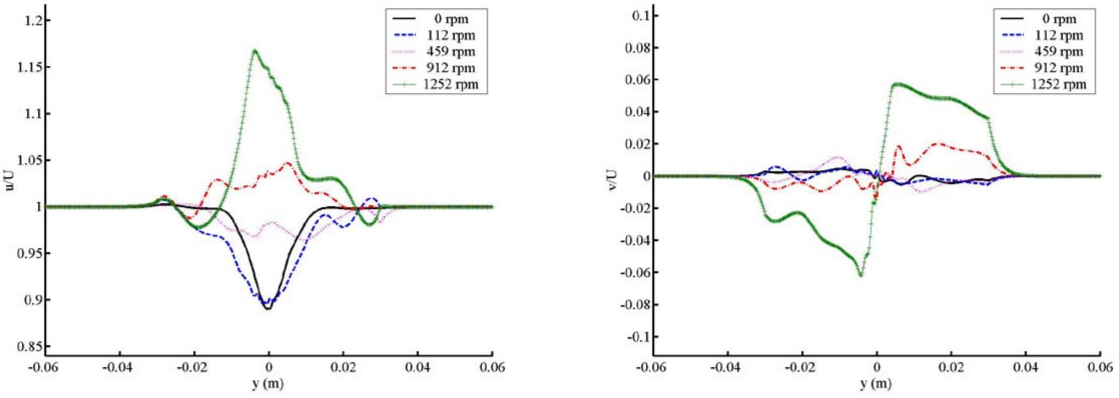

u/U v/U

Figure 3-7: Active wake for $A = 10$ (deg), $U = 1$ (m/s) and varying f (rpm)

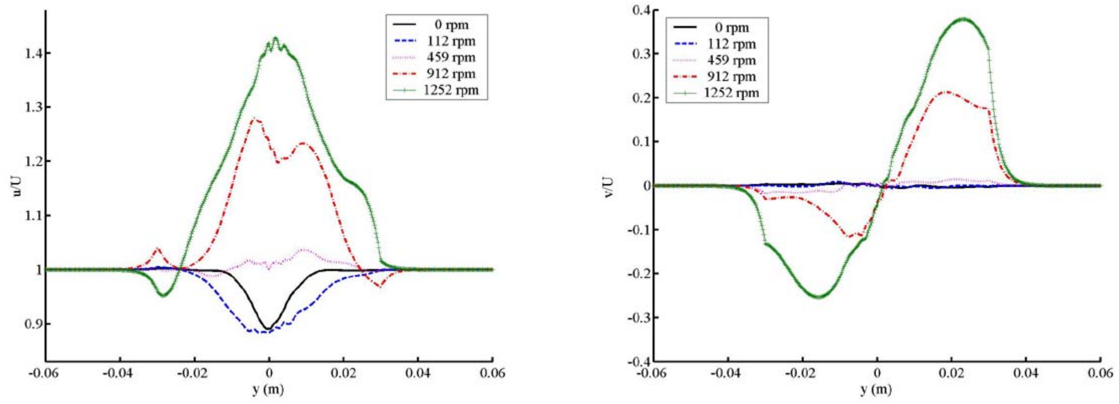

u/U v/U

Figure 3-8: Active wake for $A = 20$ (deg), $U = 1$ (m/s) and varying f (rpm)

3.6.2 Nonsinusoidal Periodic Move Profiles

After completing the sinusoidal experimental matrix there was a desire to continue on in the same way to test periodic nonsinusoidal motions. However, the space of possible nonsinusoidal tail motions is infinite and it was not advisable to perform a full factorial experiment. Therefore, an effort was made to parameterize the space of periodic nonsinusoidal motions in order to get a handle on the complexity involved. Two types of general nonsinusoidal motions were devised. The first type is referred to as the Modified Sinusoid and is defined by a single parameter, n. As n goes to zero the tail motion becomes like a square wave, while as n goes to infinity the tail motion becomes like an train of alternating impulses. The Modified Sinusoid is shown in Figure 3-9 for various values of n. This function can be written analytically as the sign of a sinusoid function multiplied by the absolute value of the sinusoid to the n^{th} power:

$$\theta = [\sin(wt)] * |\sin^n(wt)|$$

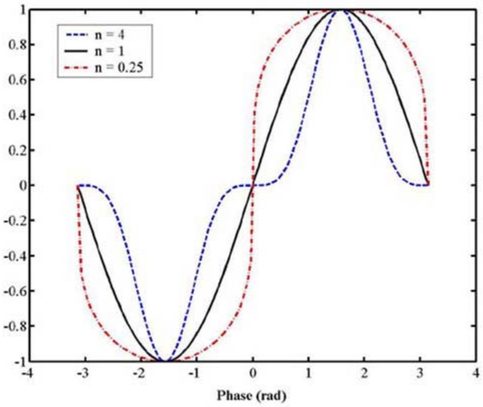

Figure 3-9: Modified Sinusoid for various values of n

The second type of parameterized motion is referred to as the Generalized Sinusoid and is based loosely off of the optimal tail motion found in [20]. This motion is constructed by 'stretching' and 'squishing' of a sinusoid. A parameter called $Theta$ defines the phase at which the function crosses the zero axis and a parameter called $Ratio$ defines the ratio of the minimal value to the maximum value. A Generalized Sinusoid with $Theta = 1$ and $Ratio = 1$ is a sinusoid. The effects of changing these parameters on the Generalized Sinusoid are shown in Figure 3-10. The Generalized Sinusoid was not be written analytically, rather it was constructed by periodic splines through the parametrically defined points. Although not used in this work, it is noted that a motion could be constructed using all three parameters; n, $Theta$, and $Ratio$.

A small experimental matrix with both U and A fixed was chosen to investigate the effect of changing the additional parameters of these nonsinusoidal motions. However, clear trends were difficult to distinguish with LDV as the wake profile often changed

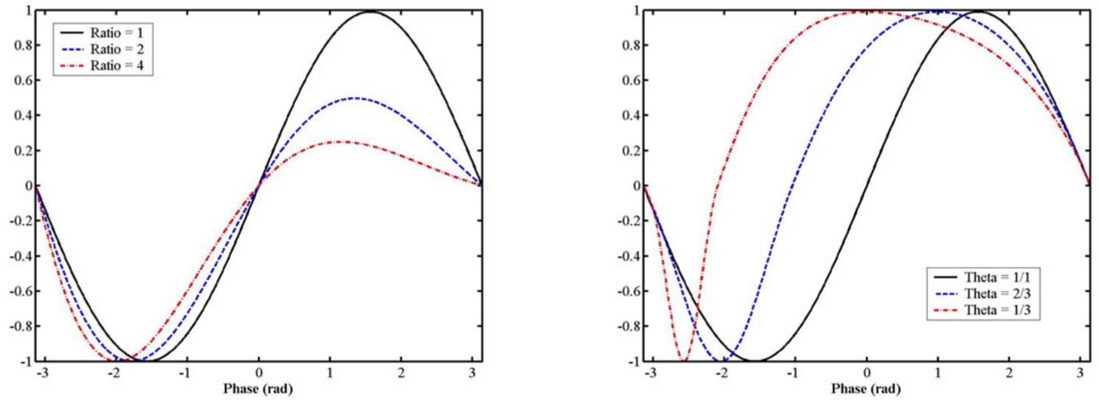

Ratio *Theta*

Figure 3-10: Generalized Sinusoid for various values of *Ratio* and *Theta*

dramatically when varying the experimental nonsinusoidal move parameters. For this reason the investigation of nonsinusoidal tail articulation was left to be completed with PIV measurements, which capture more information for each test case.

3.6.3 Frequency Domain Measurements

Frequency domain measurements were also taken during active tail articulation. For sinusoidal motions a spike in power at the primary tail frequency was observed. A secondary peak at the second harmonic was observed to become more important as the tail frequency increased and the wake deficit was reversed. This result was not surprising as the wake was expected to change with the tail motion. However, this observation led to a question which had no obvious answer. The spectrum observed in the wake for sinusoidal motions related to the Fourier transform of the tail motion, which for sinusoids is a single peak at the primary frequency. The Fourier transform of the generalized transients in the Section 3.6.2 may be very different from that of a sinusoid, would the velocity spectrum in the wake of nonsinusoidal tail motions be related to the Fourier transform of the tail motion? After examining LDV experimental data the answer was inconclusive. Some nonsinusoidal motions produced peaks only at the first and second harmonic like sinusoidal motions, even if the motion contained other frequency components. Other nonsinusoidal motions produced spectra which had peaks at the second harmonic but not the first. In no cases was the wake spectra the same as the Fourier transform of the tail motion, but in many cases it was different than the sinusoidal wake spectra. The relationship between motion and wake spectra was unclear, indicating that velocity in the wake is not a simple function of the tail motion.

3.7 Effect of Tail Articulation on Mean C_d

An analysis was desired which could tie together the large amount of data collected in Section 3.6.1 into a single result, leading to a better overall understanding of tail articulation. The plots in Figures 3-6 through 3-8 suggested that the reversal of the wake deficit was a key action of tail articulation. It was desired to find a quantity which could reflect the amount of wake reversal in a single and meaningful value. To do this a time mean control volume around the stator was imagined as shown in Figure 3-11.

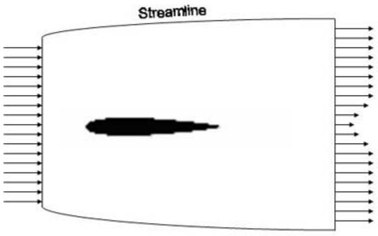

Figure 3-11: Time mean control volume around stator

Fluid flows through the boundaries of the control volume as shown, with no flow through the upper and lower surfaces which are chosen as streamlines. Assuming incompressible flow and applying mass conservation through the control volume:

$$0 = \oint \rho S * u \cdot \hat{n} ds = pS \left(\int_{y\min}^{y\max} u dy - \int_{y1}^{y2} U dy \right) \tag{3.1}$$

where ρ is the fluid density, $\hat{n}$ is the outward pointing normal to the control surface, s is the perimeter of the control surface, and S is the span of the surface into the page. Because the control volume is chosen to conserve mass, the change in momentum of fluid through the control volume may be found as:

$$\sum F_x = D = \oint \rho S u * u \cdot \hat{n} dA = pS \left(\int_{y\min}^{y\max} u^2 - (U * u) dy \right) \tag{3.2}$$

where F_x is the force in the $\hat{x}$ direction, and D is the surface drag. Because no other external forces act on the control volume and the pressure is assumed to be equal on all sides of the control volume, the change in momentum through the control volume is due only to drag forces on the stator. The coefficient of drag, C_d is then defined:

$$C_d = \frac{2D}{\rho U^2 S L_{chord}} = \frac{2}{L_{chord}} \int_{y\min}^{y\max} \left(\frac{u}{U}\right)^2 - \left(\frac{u}{U}\right) dy \tag{3.3}$$

C_d is plotted as a function of St for the experimental data taken in Section 3.6.1 in Figure 3-12.

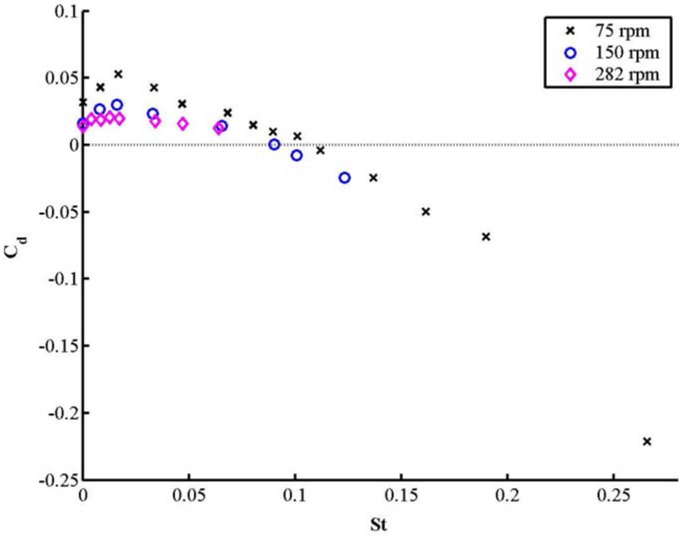

Figure 3-12: C_d vs St for varying tunnel speed (rpm)

Figure 3-12 is the most telling result of the LDV experiment. It groups the effects of the separate experimental factors into the single dimensionless quantity St and shows a clear trend with the quantity C_d. The plot makes three distinct regions of tail articulation visible. It is seen that for values of St less than 0.02, tail articulation acts to increase the effective drag on the stator. This may be seen in the widening of the wake at low frequencies in Figures 3-6 through 3-8. It may also be noted that this low frequency action is similar to the static deflection of the tail in Figure 3-5. As St increases the value of C_d begins to decrease until at $St \approx 0.1$, C_d goes to zero. At this point the mean wake behind the stator has been removed, tail articulation is adding just enough energy to compensate for the viscous drag. Further increasing St causes C_d to become negative, meaning that tail articulation is producing thrust in this range of St. Because no measurements of efficiency have been made there is no way to comment whether the range $0.25 < St < 0.35$ has a special significance in this experiment. It may be noted that the curve for C_d is noticeably higher for $U = 1$ m/s case than for the $U = 2$ or 4 m/s cases. This may be explained by the transition to fully turbulent flow as discussed in Section 3.5.1. However, all three curves behave very similarly indicating that aside from a few minor differences, such as wake width which is a function of Re, the time mean effect of tail articulation does collapse to a function of St for sinusoidal tail articulation.

Chapter 4

Wake Velocity Measurements with Tail Articulation using PIV

4.1 Theory

The experimental data collected by LDV in Chapter 3 provides an overall understanding of the effect of tail articulation on wake deficit reduction. However, because the measurements were of time mean wake velocity the previous experiments cannot provide a picture of the unsteady effect of tail articulation. This information is critical for understanding the dynamic effects of tail articulation which will be relevant to the wake blade interaction which is in itself an unsteady process. Therefore, in this chapter a measurement technique capable of capturing unsteady wake velocity functions will be used. Like LDV, Particle Image Velocimetry, PIV, is a non-invasive fluid measurement which measures the velocity of particles suspended in the fluid. However, the PIV measurement technique is more intuitive than that of LDV. In PIV, particles in a two dimensional plane are photographed at known times. These particles are then tracked between image frames to give estimates of the local fluid velocity in the measurement plane. In order to capture the position of the particles at a specific time a pulsed laser is used to illuminate the image plane during the image capture. This results in a clear picture of the particles at each time rather than imaging them as a series of streaks. The time interval between images must be long enough that the particles move a discernable amount between the images. However, the interval must also be short enough that particles can easily be tracked between frames so that velocity estimates remain accurate.

Traditionally, the desired time interval between image captures has been much faster than the available camera frame rate. Therefore, it has not been possible to continuously sample images at the desired rate. Two PIV techniques have been developed to deal with this problem. The most basic technique allows two laser pulses to occur during a single frame capture, double exposing each frame. A fundamental difficulty with this method is in determining which particles in the frame were captured during the first pulse and which come from the second. Velocity field estimates help to determine which direction the particles should be moving but in general a directional ambiguity exists. A second approach eliminates the directional ambiguity but requires more precise synchronization between the camera and laser pulses. In this technique the two laser pulses are set to "straddle" two separate image captures. The first laser pulse occurs at the end of the first frame and the second pulse at the beginning of the second frame, with the total time difference equal to the desired interval. With this technique each frame is exposed only once so there is no ambiguity as to which particles came first or second. As digital photography technology has progressed the available frame rate has increased towards the rate desired for particle captures. The most modern PIV systems use digital video cameras to capture particle images in a continuous series, rather than limiting the capture to image pairs. This allows a great deal of data to be recorded quickly and increases accuracy in the processing because particles can be tracked through more than two frames.

4.2 PIV Hardware

The PIV system available at the NUWC water tunnel consists of a TSI high resolution 1024x1024 CCD camera, a TSI LaserPulse 610030 synchronizer, and two pulsed Nd:YAG New Wave MiniLase III lasers. In each laser a flashlamp excites Neodymium atoms in a YAG rod to an energy level where light is emitted. As long as a electrooptic device called a Q-switch remains closed this energy is not allowed to leave the chamber, causing energy to build up in the rod. When a high voltage signal is applied to the Q-switch the light is allowed to leave the chamber where it encounters a mirror and is reflected back and forth through the rod, setting up a synchronized lasing. This high power beam quickly overcomes losses imposed by the output reflector and leaves the laser chamber as a high power pulse lasting approximately 7 ns. The primary laser wavelength is 1064 nm. However, frequency conversion by KTP crystal is used to change over half of the output light into the lower visible frequencies of 532, 355, and 266 nm. An optical beam spreader converts the laser beam into a diverging two dimensional light sheet. The light sheet is aligned level to the tunnel, halfway down the stator and centered one chordlength downstream. This allows particle displacements in the $\hat{x}$ and $\hat{y}$ directions to be measured. Particle movement in the $\hat{z}$ direction will cause the particle to move out of the light sheet plane. Particles lost due to movement out of the plane will cause trouble for the PIV tracking software. Fortunately the wake behind the active stator is acceptably two dimensional and this effect will be minimal. Unfortunately, the camera available at NUWC is about 10 years old with a maximum frame rate of approximately 2 Hz and so is not capable of the frame rate required for continuous image capture PIV. The maximum repetition rate of each laser is 10 Hz, so two lasers are required with one laser timed to fired 200 μs before the other to achieve the desired image time interval. The synchronizer is capable of timing both laser pulses with the camera's frame capture to enable frame straddling. A picture of the PIV apparatus is shown in Figure 4-1.

A calibration plate is used to relate particle displacements measured in pixels by the camera to real world displacements. The calibration plate has mating holes drilled which match the bolts on the water tunnel. This allows the calibration plate to be repeatedly installed in the same position relative to the stator. A 5x5 grid of black crosses with 1" spacing is printed onto an overhead transparency and super glued to a u-beam fixed to the calibration plate. This allows the calibration grid to be placed in the same plane in the tunnel as the laser light sheet. The calibration plate is installed when setting up the camera and the tunnel is filled until water completely covers

Figure 4-1: PIV setup

the calibration plane. The camera is adjusted until the calibration grid is square, centered, in focus and filling as much of the camera field of view as possible. When the final camera adjustment is complete a picture of the calibration plate is recorded. The camera is held by a tripod which is affixed to a heavy steel plate with waterproof silicon caulk to prevent the camera from moving after calibration.

4.3 Experimental Procedure

After calibration the stator apparatus is installed and the tunnel is seeded with particles as in Chapter 3. The challenge in PIV is the coordination between the camera, laser pulses and the motion of the stator. Details of the hardware setup may be found in Appendix C, an overview of the experimental procedure is given here. The time interval between images pairs in this experiment is 200 μs. The camera runs

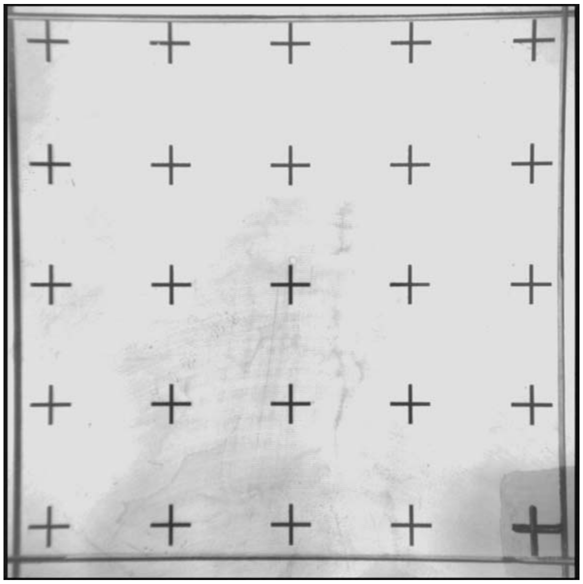

Figure 4-2: PIV calibration image

continuously on an internal clock with a period of 530 ms. The synchronizer receives the clock signal from the camera and synchronizes the laser signals to straddle the camera frames, but does not yet send these signals to the lasers. At the beginning of each experimental run a LabView program is used to interface the motion controller and start the tail motion. The tail is allowed to run at full speed for at least 20 periods to allow start up transients in the wake to disappear. After this time a button is pressed on the LabView program to start the PIV measurement process. The motion controller sends a signal to the synchronizer which enables the laser pulses and begins the capture of images from the camera. A time stamp is recorded for each image pair that is captured. A high speed interrupt in the LabView program also records the tail position and time stamp each time the Q-Switch signal is sent to the first laser. The number of images recorded during each run is limited to 16 pairs by the available memory of the computer running the Insight software. After the maximum number of images are recorded the motion controller sends another signal to the synchronizer disabling the laser pulses. The motion and image time stamps are lined up to determine the tail position in each image pair, Figure 4-3. The periodic tail motion is divided into thirty equally spaced phase bins from -π to π and the fluid velocity field in each phase bin is taken as the average of the velocities of all processed image pairs which fall in that bin. This averaging is done to separate repeatable wake effects from random fluctuations due to turbulence. As the experiment progresses a histogram is kept showing the number of image pairs in each phase bin, Figure 4-4. The experiment continues until there are at least 8 image pairs in each phase bin. Because the tail frequency is much faster than the camera's frame rate, the tail frequency is chosen such that it beats with the camera's frame rate. This property is useful in that it helps to fill up the phase bins more evenly. Since there are 16 image pairs taken each run, the frequency beating is such that the phase of the tail changes by $\frac{2\pi}{16}$ during each camera sample period.

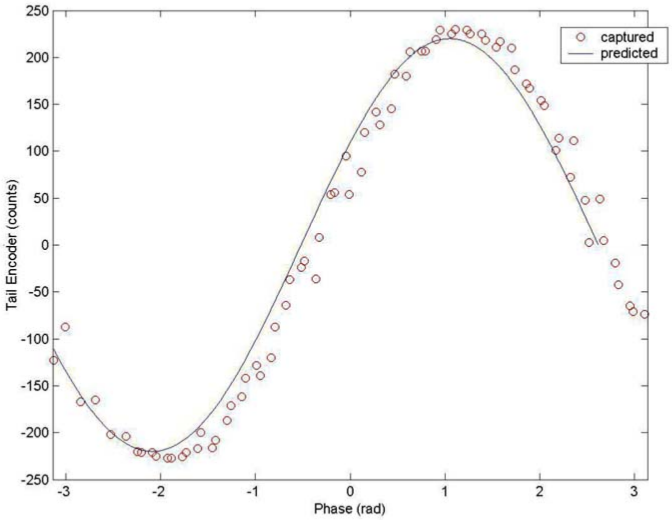

Figure 4-3: Captured tail positions

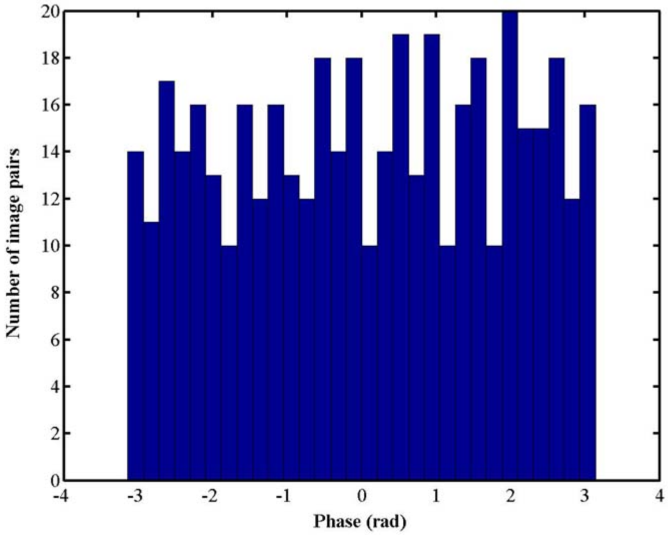

Figure 4-4: Histogram of image pairs per phase bin

4.4 Image Processing

4.4.1 PIV Software

After the PIV hardware is configured, the second but equally important PIV component is the software used to process the image pairs to determine velocities in the particle plane. Several commercial PIV processing software packages exist, but they are very expensive and do not allow the user full access to the processing algorithms. Therefore, the PIV processing software used in this research is an open source Matlab based package called MATPiv [30]. This software is freely available as source code from the author. This is advantageous as it allows the researcher to build user specific functions to interface the MATPiv software. A guide to the functions developed for this research is given in Appendix A. A brief overview of the PIV post-processing process is given here. The processing begins with individual image pairs taken 200 μs apart, a typical PIV image pair is shown in Figure 4-5.

Each image is stored in a black and white TIFF file, with intensity values given on a 1024x1024 grid. Rather than identify and track individual particles between the

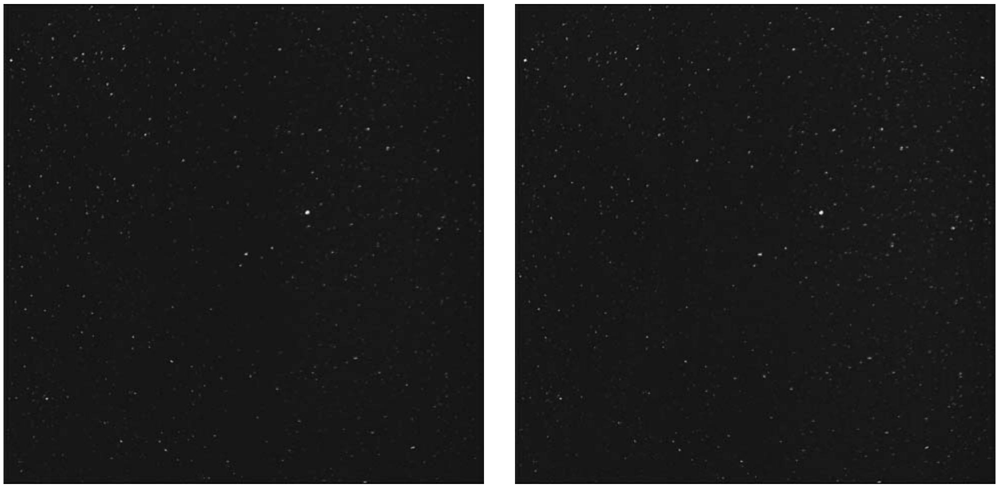
a000 a001

Figure 4-5: Typical PIV image pair

two images, MATPiv attempts to track groups of particles by grid cross-correlation. This analysis works best on highly seeded flows with relatively small particles. The processing starts by dividing both images into large grids, 128x128 pixels. The program computes the two dimensional cross-correlation between corresponding grid areas in the first and second image. The highest peak in the cross-correlation is taken as the best guess for the translation of the entire grid area in the time between laser pulses. This is equivalent to translating one grid over the other until the sum of the particle overlap is maximized. The cross-correlation is biased towards a zero displacement because the area of overlap between the grid areas is maximized at zero displacement. Cross-correlation can be normalized by dividing by the correlation of the windowing function to remove the bias, however this is not done as it also increases the sensitivity to noise near the grid boundaries. When using biased cross-correlation a general rule of thumb is that the particle displacements should not be more than 1/3 of the grid size in order avoid problems with low area overlap at the grid edges. At the next time step the grid size is reduced and the process is repeated, leading to a higher resolution of the local velocity. However, at the next time step each grid area in the second image is offset from the grid in the first image by the estimated displacement from the first pass. This method is useful for overcoming the bias towards zero displacement as the grid size becomes smaller because zero displacement between the offset grids corresponds to the current estimate of velocity [37]. This process is repeated until the final pass when the pixel displacement is estimated by a sub pixel gaussian interpolation of the cross-correlation [38]. In this research the final grid size is 16x16 pixels which relates to a 0.9x0.9 mm grid resolution in real world units. The challenge in this type of PIV processing is to deduce which grid displacement estimates are reasonable and which are due to numerical error, known as bad vectors, at each iteration. This step is crucial because the accuracy of the next pass depends on the accuracy of the current estimate. Therefore, before each iteration a series of filters is applied to the estimated data and vectors which fail are removed. The first filter is a signal to noise ratio filter which eliminates vectors if the ratio between the highest cross-correlation peak to the second highest is too low. A peak filter eliminates any vectors if the height of the highest peak is too low. A local filter removes vectors if their absolute value varies too much from the surrounding neighbors. A global filter removes any vectors that vary too much from the average of the entire data set. After suspect vectors are removed an interpolation scheme is used to fill in for vectors which have been removed. Picking the values of these filters is a difficult problem. Setting the filters too strictly may eliminate valid vectors while setting them too loosely may allow bad vectors to propagate through to the final velocity estimate.

4.4.2 Testing with Synthetic Images

The Visualization Organization of Japan is currently making an effort to provide standard PIV images for use in determining the accuracy and effectiveness of PIV processing software, [25]. Computer generated images of particles in a simulated shear flow near a wall are available from the group's website. Because the group also provides a known velocity field, these images were used to tune the filter parameters used to process the PIV data. In order to best emulate the experimental data from this experiment images were generated with an average of 500 particles per frame, average particle size of 4 pixels and an average particle displacement of 1.33 pixels. A small set of four image pairs was processed and the resulting velocities were averaged and compared to the known velocity field to give an error estimate as filter levels were changed. It was noted that even in cases with low relative error, the PIV processing routines had the most difficulty in areas of high shear. The final filter levels were set more loosely than had been previously estimated; minimum signal to noise = 1.4, minimum peak height = 0, maximum local deviation = 3.4, maximum global deviation = 3.

4.5 Baseline Measurements

4.5.1 Index of Refraction

Initial PIV measurements of the fluid velocity in the unobstructed test section showed an increase of u velocity by approximately 10% in the $\hat{x}$ direction. The cause of this acceleration was not understood at first and caused considerable confusion. It was thought that the processing software might incorrectly process flow at the edge of the interrogation area and this error might propagate through the calculations. It was also thought that boundary layer growth could be causing the flow in the center of the channel to accelerate. However, the PIV software correctly processed the computer generated test images and LDV data did not show any acceleration in the freestream velocity. Identification of the actual problem happened after a simple glance at the tunnel when it was half filled with water. It was seen that the difference in index of refraction between air and water played a trick on the image of the half submerged stator, Figure 4-6.

Calculations showed bending of camera rays due to the change in index of refraction would account for the increase in velocity seen in the preliminary measurements. The optimal method to compensate for the effects of index of refraction would be to build a camera housing which minimizes the distance that light rays from the tunnel travel in air before entering the camera lens. However, a solution implemented in software would take less time and be less expensive. Therefore, a nonlinear calibration was used to account for the effect of index of refraction. The nonlinear terms

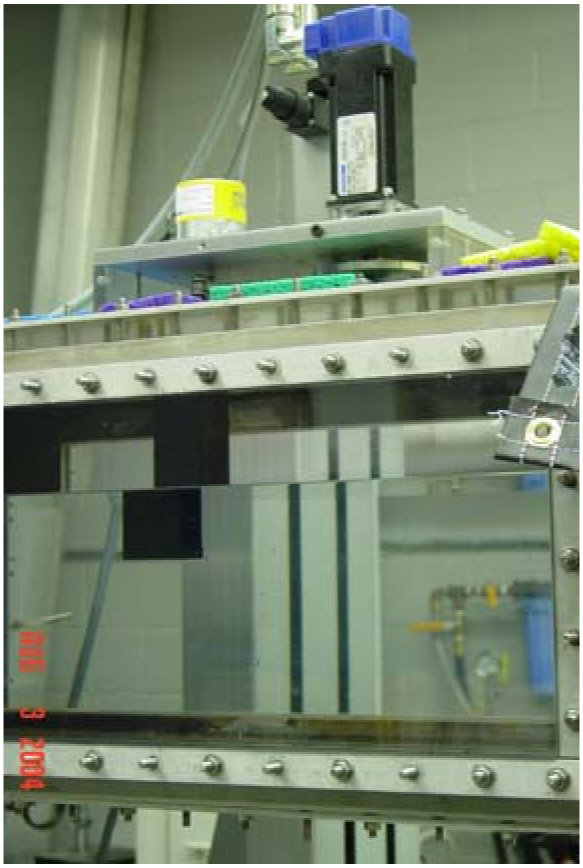

Figure 4-6: Effect of index of refraction

were found along with the linear terms by a least squares fit to the calibration grid. Because the effect of refraction is greatest at higher angles the nonlinearity is most noticeable at the edges of the image, seen in Figure 4-2. The calibration plate should fill as much of the image as possible in order for the calibration function to best account for these effects. After implementing the nonlinear calibration the PIV measurements of velocity in the unobstructed tunnel agreed to within 2% of the tunnel calibration in Section 3.4 and showed only minimal acceleration at the image corners.

4.5.2 Comparison with LDV data

After PIV measurements were shown to agree with the freestream velocity measurements made by LDV it was also desired to test how well the PIV measurements of the stator baseline wake agreed with the LDV data taken in Section 3.5. Because LDV measures the time mean velocity at each point in the wake a time mean comparison of LDV and PIV was appropriate. The first three cases investigated were the three baseline stator wake measurements from Section 3.5. Over three hundred PIV pairs were taken with no tail deflection for each of the three cases in Section 3.5. These image pairs were processed and the velocity averaged on the same line as the LDV measurement to give an estimate of the time mean velocity profile. The comparison of the wake measured by LDV with that by PIV is shown in Figures 4-7 through 4-9.

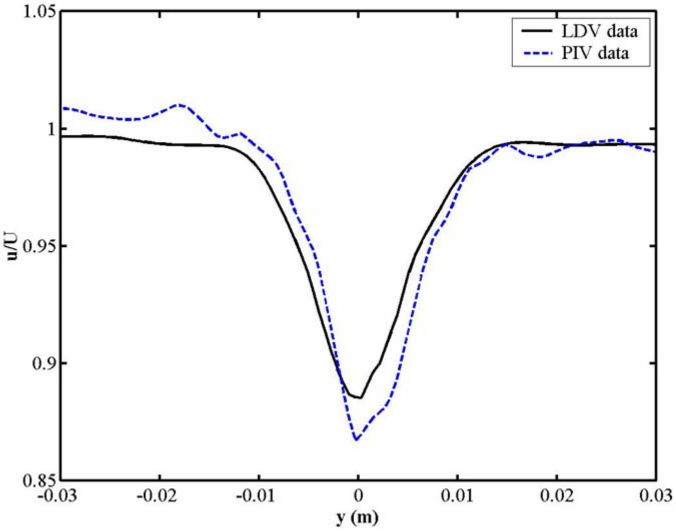

Figure 4-7: Baseline wake at $U = 1$ (m/s) with both LDV and PIV

It all cases the same general wake shape is seen with both measurement techniques. However, discrepancies between the velocities measured by the two techniques are apparent. At $U = 1$ m/s the PIV data shows a larger wake deficit than was measured by the LDV. At $U = 2$ and 4 m/s the normalized wake measured by PIV is less deep than that by LDV. This result, along with the tests in Section 4.4.2 shows that the MATPiv processing method is less accurate in regions of high shear in a flow. This effect is due partly to local filtering and also because the grid areas used for interrogation, while allowed an offset to account for particle translation between time

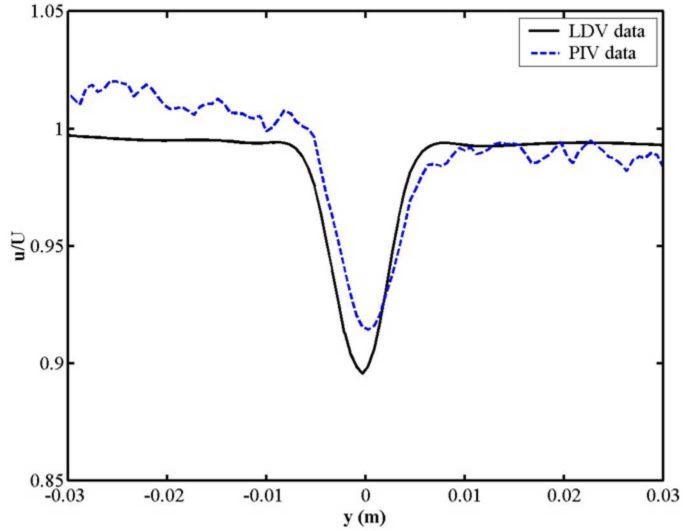

Figure 4-8: Baseline wake at $U = 2$ (m/s) with both LDV and PIV

steps, are not allowed to deform to account for shear. Thus the correlation between the fixed grids is not as high as that between Lagrangian grids which deform with shear. Adaptive PIV techniques have been developed which use estimates of local shear to account for the second order deformation of grids, but this technique was not used in this research. Rather, the qualitative effects of tail articulation will be seen in the PIV measurements, and slight errors in the actual fluid velocity field will be tolerated.

4.5.3 Vorticity Visualization of Baseline Wakes

It was noted earlier that the baseline wake deficit may be thought of being due to the shedding of vorticity from the stator's boundary layer and this topic should be expanded upon here. A particle suspended in a fluid has six degrees of freedom; three degrees of translation and three of rotation. The velocity of the particle is a familiar quantity and measures the rate of translation of the particle. Vorticity can be thought of as the rate of rotation of the particle. Mathematically, vorticity is defined as the

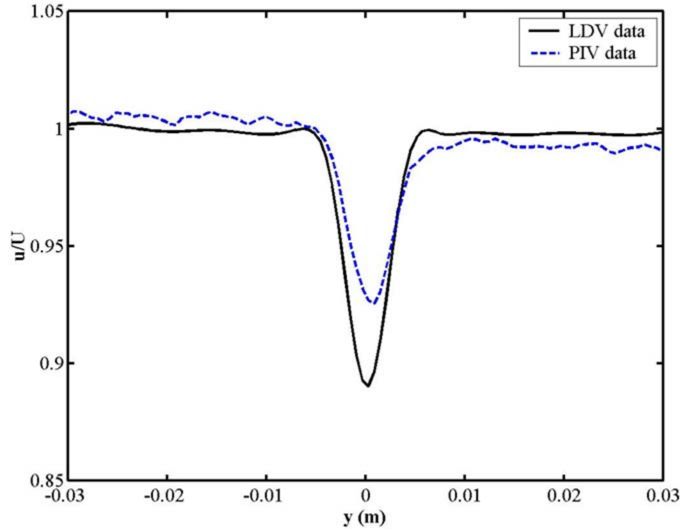

Figure 4-9: Baseline wake at $U = 3$ (m/s) with both LDV and PIV

curl of the velocity vector. If the velocity field is two dimensional, the expression for vorticity is greatly simplified:

$$\omega = \nabla \times \vec{u} = \left(\frac{\partial v}{\partial x} - \frac{\partial u}{\partial y} \right) \hat{z} \tag{4.1}$$

The simplification of two dimensional flow is that vorticity exists only in the $\hat{z}$ direction. In the stator boundary layer the u velocity changes rapidly in the $\hat{y}$ direction moving away from the stator, but v is very small and does not change rapidly in the $\hat{x}$ direction. The equation for vorticity shows that $\hat{z}$ vorticity is created in the boundary layer due to the change of u velocity in the $\hat{y}$ direction. This can be visualized by imagining a particle half in the boundary layer and half in the freestream. The portion of the particle in the freestream will move more quickly than the portion in the boundary layer, resulting in a rotation as well as net translation. The relationship between vorticity in the boundary layer and the baseline wake deficit is shown in Figure 4-10. Notice that the sign of the vorticity in 4-10 is related to the sign of the wake deficit, if the sign of shed vorticity were reversed the wake deficit also would be reversed.

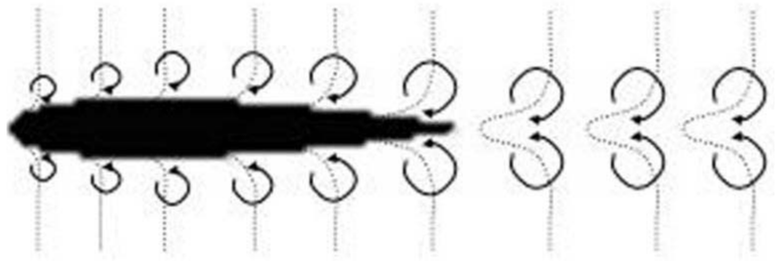

Figure 4-10: Wake deficit due to shedding of boundary layer vorticity

Because vorticity in a two dimensional flow exists in only one direction it may be thought of as a scalar and can be used to visualize the stator wake. As seen in Figure 4-10 this visualization can be quite meaningful. In more general terms it is possible to gain meaningful insight into the active wake by visualizing vorticity. Therefore, further plots of PIV data in this research display the vorticity field because it represents both components of velocity at once in a meaningful way. The baseline wakes are presented in this form in Figures 4-7 through 4-9. The right hand rule specifies that negative vorticity is into the page and positive vorticity is out of the page. The absolute value of vorticity increases as the freestream velocity increases. This is due to the thinner boundary layer and higher levels of shear that occur at high *Re*. It can also be seen that the wake tends to spread out and dissipate due to viscous forces as it is convected downstream.

4.6 Active Sinusoidal Articulation Measurements

The results in Section 3.7 showed that the effect of sinusoidal tail articulation on C_d can be separated into three regions by *St*. However, knowing the time mean effect of tail articulation does not necessarily provide much insight in the actual structure of the wake in each *St* region. Visualization of the unsteady wake by PIV measurement

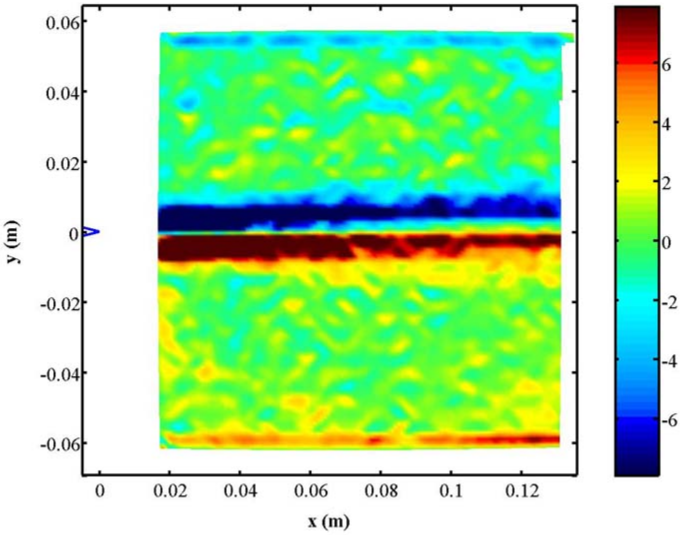

Figure 4-11: Vorticity (1/s) in baseline wake for $U = 1$ (m/s)

provides much more insight into the effect of tail articulation at different St. In order to relate tail motion to the vorticity in the wake, a blue line representing tail tip displacement convected downstream at U is plotted in Figures 4-14 through 4-25. This also gives a sense of the reduced frequency, k, which is the frequency (1/m) of disturbances in the stator wake:

$$k = \frac{f}{U} \tag{4.2}$$

A similar white line is also plotted representing the negative of tail tip velocity for reasons which will be made clear in Section 5.1.

4.6.1 Quasi-Steady Wake Spreading

At low St the time wake was seen to spread outwards in Section 3.7, increasing the effective C_d. Therefore, it was not surprising that the PIV measurements capture a quasi-steady wake pattern for tail articulations in the drag inducing range of St. In this region it seems that the region of fluid affected by the tail articulation is simply

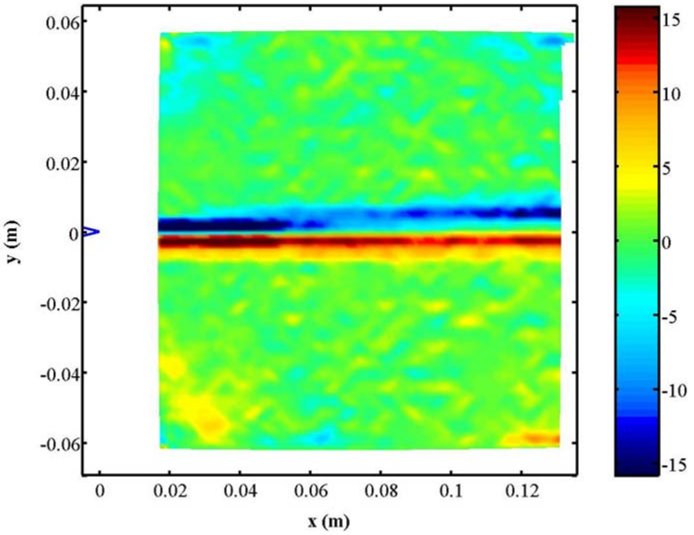

Figure 4-12: Vorticity (1/s) in baseline wake for $U = 2$ (m/s)

deflected back and forth with the motion of the tail, Figure 4-14. As St increases this region becomes wider, Figure 4-15. It should be noted that the wake alternates between a positive and negative vortex sheet rather than simply a deflection of the dual signed drag indicative vortex wake seen in Figures 4-11 and 4-13

4.6.2 Vortex Roll Up

The next region of interest identified in Section 3.7 was the St range where C_d begins to decrease and finally becomes zero. In this range the time mean wake deficit is almost completely reduced. PIV measurements in this range show that the deflected vortex sheet begins to roll up on itself in this St range, Figure 4-16. A case with a time mean drag of almost zero is shown in Figure 4-17. It is important to note that although the time mean wake is almost zero, the unsteady wake fluctuates strongly. This is unfortunate because a steady, zero fluctuation wake would be ideal for the propeller to pass through. Figures 4-16 and 4-17 show that even if tail articulation adds just enough energy to cancel out the wake deficit due to stator drag, the problem of timing the blade to optimally pass through the unsteady wake still remains.

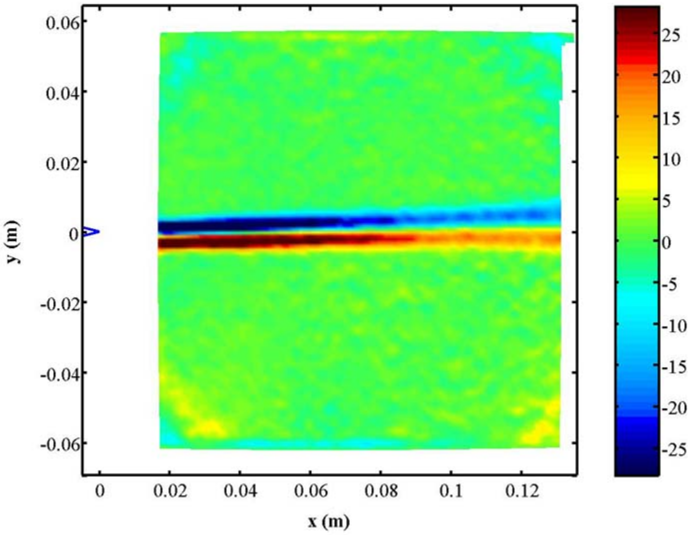

Figure 4-13: Vorticity (1/s) in baseline wake for $U = 3$ (m/s)

4.6.3 Strong Vortex Regime

The final St region of interest identified in Section 3.7 is the one where tail articulation produces thrust, resulting in a negative value for C_d. PIV measurements in this region show that the shed vortex sheet has completely rolled up into tight, discrete vortices. In this region k is high enough that several tail wavelengths are visible in the image plane at one time. It is noted that while vortices in the wake are formed and remain at the same frequency of the tail motion, their x position slightly lags behind the tail displacement trace. This effect may due to a physical time scale associated with diffusion of vorticity from the stator into the wake or viscous effects. However, it may also be a result of a delay or slight systemic experimental error in the PIV data collection or processing routines.

4.6.4 St Observed in Strong Vortex Wake

The St based on the tail displacement A is known for all of the PIV measurements. However, the question of what St vortices in the wake align themselves at remains.

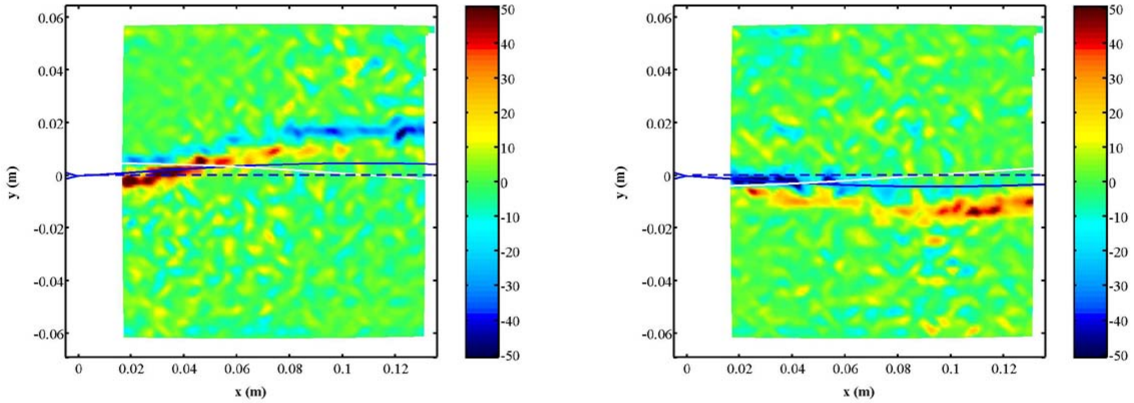

Tail phase = -π, bin 1 Tail phase = 0, bin 15

Figure 4-14: Vorticity (1/s) for f = 459 (rpm), A = 10 (deg), U = 3 (m/s), St = 0.023

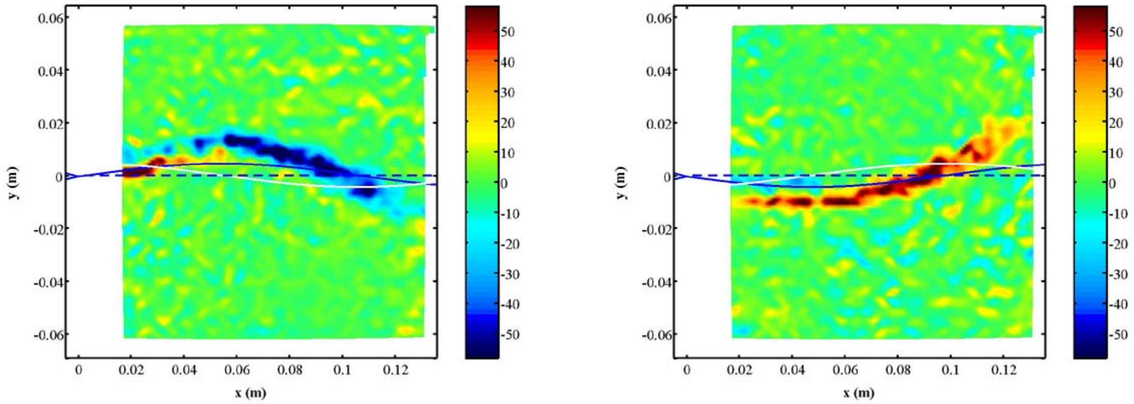

Tail phase = -π, bin 1 Tail phase = 0, bin 15

Figure 4-15: Vorticity (1/s) for f = 912 (rpm), A = 10 (deg), U = 3 (m/s), St = 0.045

To provide a quick estimate of the wake St, with A based on wake width, the centers of the first two vortices the PIV frame are tracked for the cases in the strong vortex regime. The center of each vortex is estimated by the center of vorticity, in the same manner center of mass is found. The wake St is then calculated at each phase with A as the distance between vortices rather than tail tip deflection. The results are shown in Figures 4-20 and 4-21. It is seen that the free wake St begins at about one half of the St based on tail tip deflection, meaning that vortex centers are initially spaced at about one half of the maximum tail tip displacement. Wake St is then seen to decrease steadily as the vortices convect downstream. The best fit line has a slope

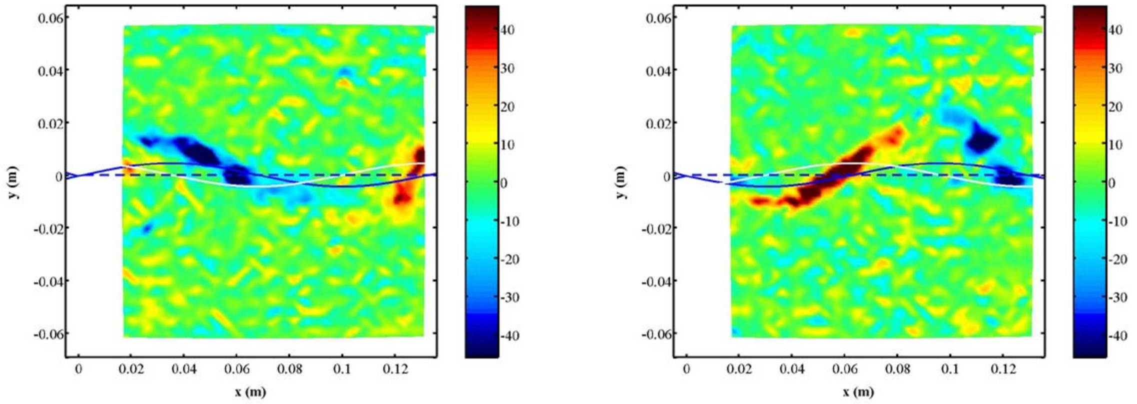

Tail phase = -π, bin 1　　Tail phase = 0, bin 15

Figure 4-16: Vorticity (1/s) for f = 912 (rpm), A = 10 (deg), U = 2 (m/s), St = 0.065

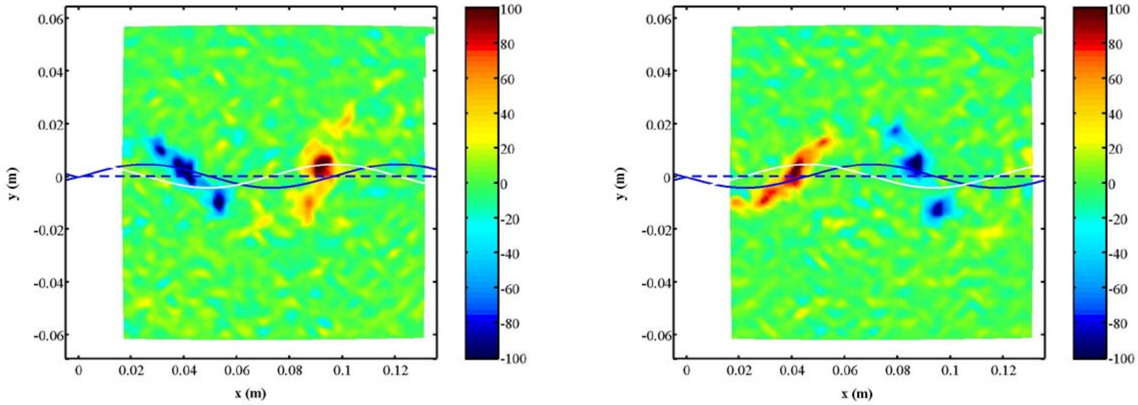

Tail phase = -π, bin 1　　Tail phase = 0, bin 15

Figure 4-17: Vorticity (1/s) for f = 1252 (rpm), A = 10 (deg), U = 2 (m/s), St = 0.089

of -0.51 (St/s) for the f = 912 rpm case and -0.56 (St/s) for the f = 1252 rpm case.

4.6.5 Active Nonsinusoidal Tail Articulation

The definition of St becomes less clear with nonsinusoidal motions, therefore relevant parameters in each of the following nonsinusoidal move profiles are set to $f = 11.36$ (Hz), $A = 10$ (deg), and $U = 1$(m/s). St based on these parameters is 0.101, however the wake dependance on St is most likely a separate function for each tail motion. Ideally f would be set to a value for which sinusoidal tail motions had been studied by

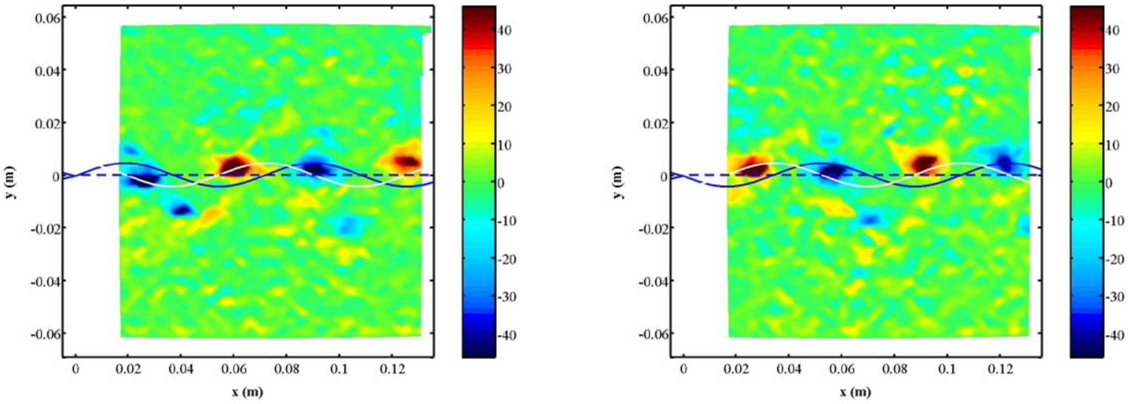

Tail phase = -π, bin 1 Tail phase = 0, bin 15

Figure 4-18: Vorticity (1/s) for f = 912 (rpm), A = 10 (deg), U = 1 (m/s), St = 0.136

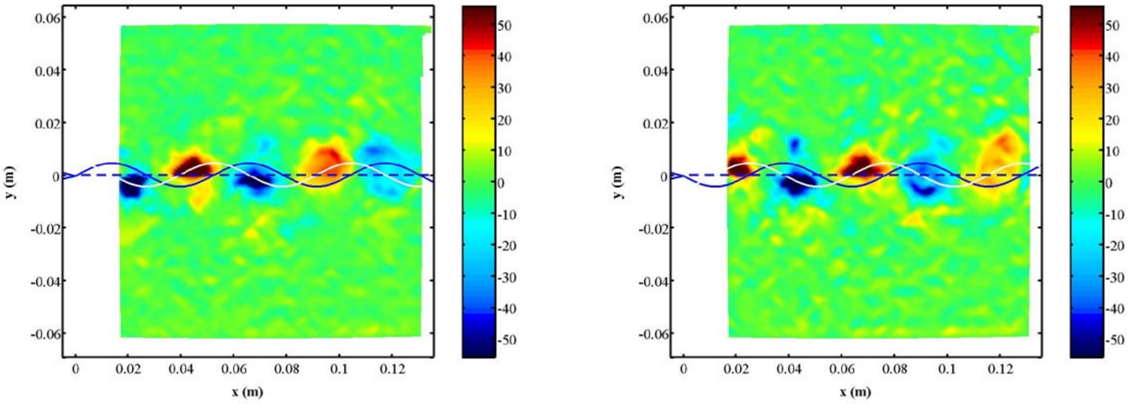

Tail phase = -π, bin 1 Tail phase = 0, bin 15

Figure 4-19: Vorticity (1/s) for f = 1252 (rpm), A = 10 (deg), U = 1 (m/s), St = 0.186

LDV and PIV. However, the servo controller used for nonsinusoidal tail articulation is limited in the frequencies of motions that it can support. The available servo frequency which best matched the camera frequency beating requirement was 11.36 Hz or 681.6 rpm. This frequency is acceptable because it is between two values of f for which sinusoidal motion wakes were measured. The first move profile shown is the Modified Sinusoid with $n = 0.25$, which is somewhat between a square wave and a sinusoid. The wake due to this move profile is shown in Figure 4-22. Vortices in the wake have rolled up into a strong thrust producing vortex wake. This similar to sinusoidal wake in the same thrust producing range of St.

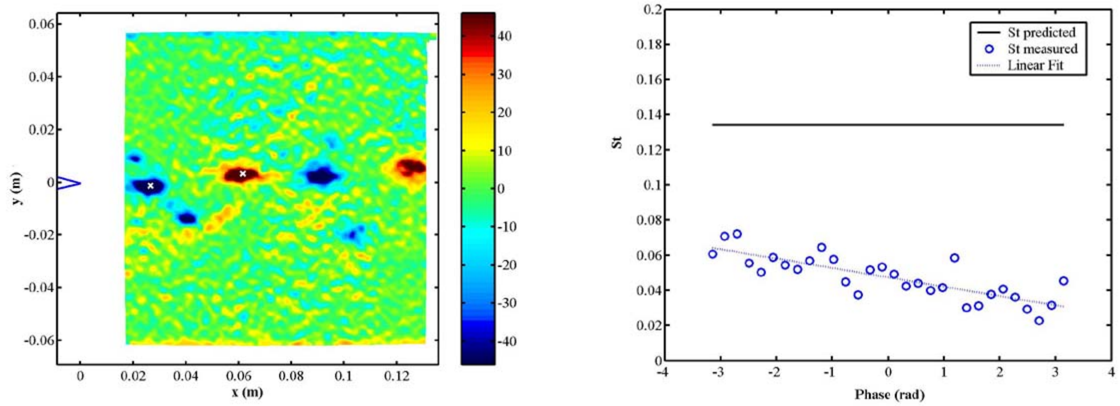

Tracked vortex centers

St vs phase (rad)

Figure 4-20: St in the wake for $f = 912$ (rpm), $A = 10$ (deg), $U = 1$ (m/s)

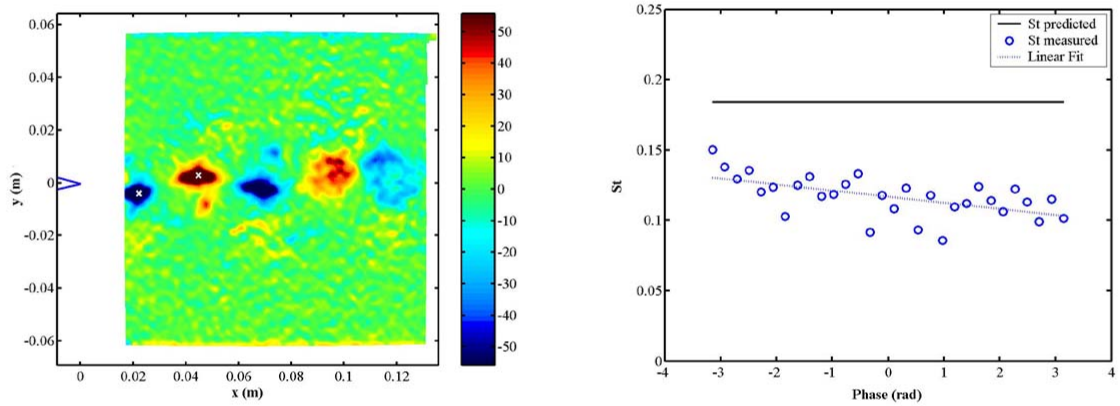

Tracked vortex centers

St vs phase (rad)

Figure 4-21: St in the wake for $f = 1252$ (rpm), $A = 10$ (deg), $U = 1$ (m/s)

The next tail motion studied is the Modified Sinusoid with $n = 4$ and is somewhat between a sinusoid and an impulse train. Although the vortex sheet rolls up into strong vortices the behavior of this wake is markedly different from previous wakes. The frequency of vortices in the wake is higher than for other tail motions, 4 vortices are formed each period rather than 2. This explains the increase in wake velocity frequency noted in Section 3.6.3. These vortices are unevenly spaced in the wake as pairs of alternating positive and negative vortices. Furthermore, the unequal spacing of these vortices results in a significant transverse velocity of the vortex pairs, which has not been noted in other cases.

The next tail motion studied is based on the Generalized Sinusoid with $Ratio =$

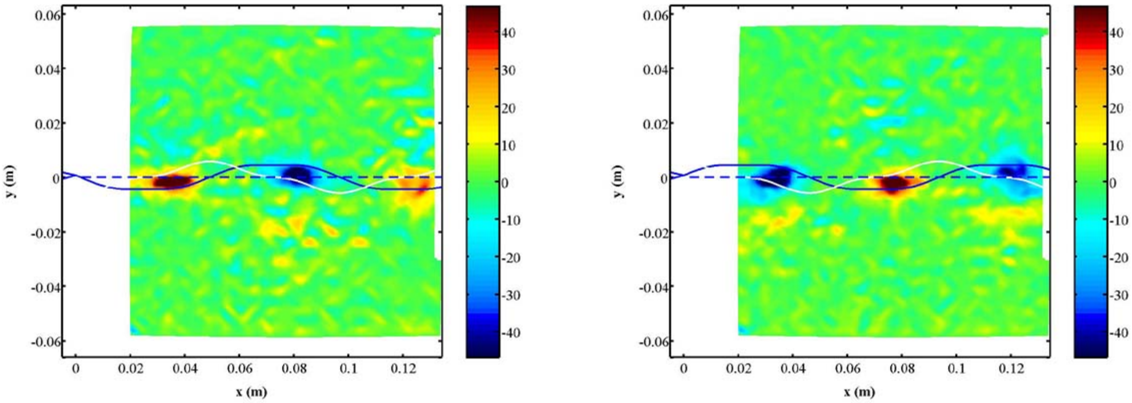

Tail phase = -π, bin 1 Tail phase = 0, bin 15

Figure 4-22: Vorticity (1/s) for Modified Sinusoid f = 11.36 (Hz), A = 10 (deg), U = 1 (m/s), n = 0.25

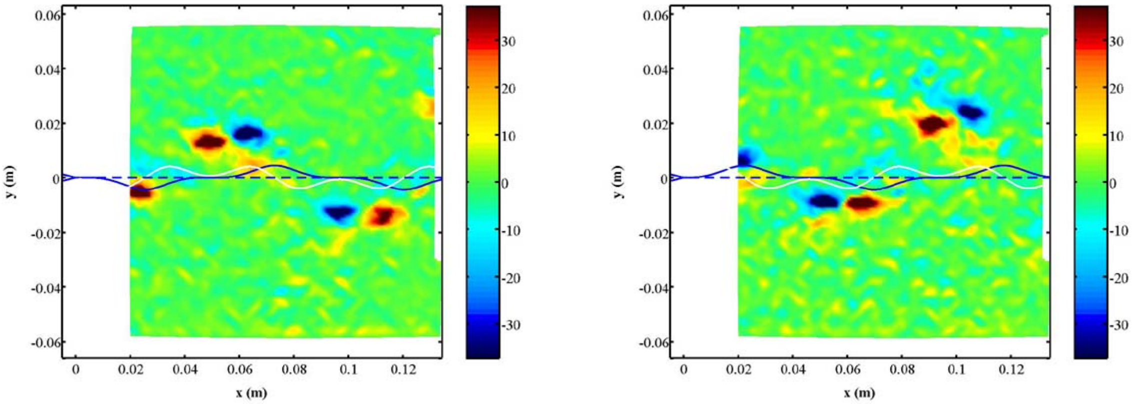

Tail phase = -π, bin 1 Tail phase = 0, bin 15

Figure 4-23: Vorticity (1/s) for Modified Sinusoid f = 11.36 (Hz), A = 10 (deg), U = 1 (m/s), n = 4

2 and $Theta$ = 1. This motion forms two vortices per period. However, one vortex seems to roll up more than the other, resulting in an uneven wake.

The final tail motion studied is also based on the Generalized Sinusoid with $Ratio$ = 1 and $Theta$ = 0.67. This motion forms two vortices per period, again unevenly spaced in the wake.

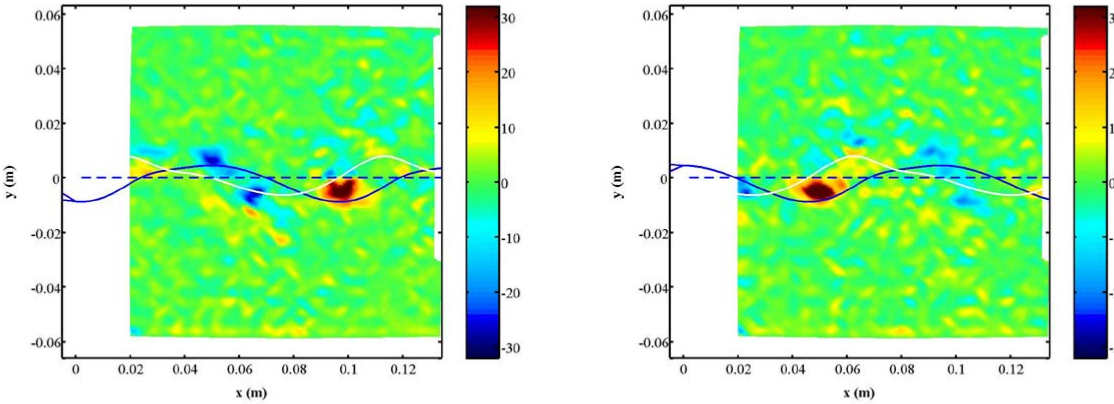

Tail phase = -π, bin 1

Tail phase = 0, bin 15

Figure 4-24: Vorticity (1/s) for Generalized Sinusoid $f = 11.36$ (Hz), $A = 10$ (deg), $U = 1$ (m/s), $Ratio = 2$ and $Theta = 1$

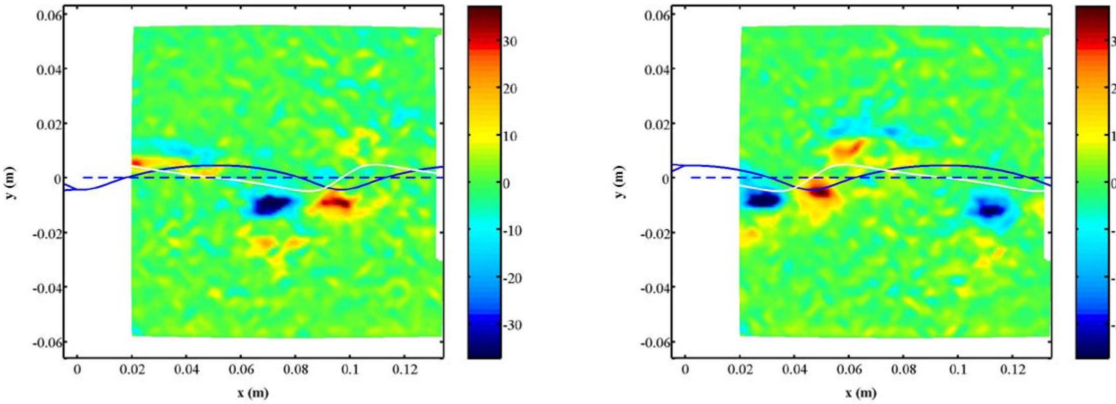

Tail phase = -π, bin 1

Tail phase = 0, bin 15

Figure 4-25: Vorticity (1/s) for Generalized Sinusoid $f = 11.36$ (Hz), $A = 10$ (deg), $U = 1$ (m/s), $Ratio = 1$ and $Theta = 0.67$

Chapter 5

Potential for Noise Reduction Using Tail Articulation

5.1 Reduced Order Model of Tail Articulation

As stated in Chapter 2, a primary goal of this experimental work is the creation of a reduced order model relating tail motion to the resulting unsteady wake. This model is needed in order to develop a closed loop control strategy for noise reduction by tail articulation. It is assumed that on the final vehicle either unsteady propeller forces or radiated noise will be measured and used as feedback to a real time control law governing the tail motion. There are two ways in which such a control law could be used to govern the tail motion on the final vehicle. The most advanced method would be to use a control law which completely defines the tail motion in real time for optimal noise reduction. A less advanced control system would use a pre-defined tail motion, altering the tail motion only slightly to reject disturbances. Either way, the effect that tail articulation will have on the stator wake and the effect that the stator wake will then have on the unsteady propeller forces must be known in order to correctly define the best tail motion for noise reduction. The tail articulation and blade interaction models are shown as blocks in Figure 5-1. These are analogous to traditional transfer functions, although they are nonlinear and time varying. Simple models of these effects are desired in order to simplify the tail motion optimization and control law. However, these models must sufficiently describe all essential characteristics of the real system.

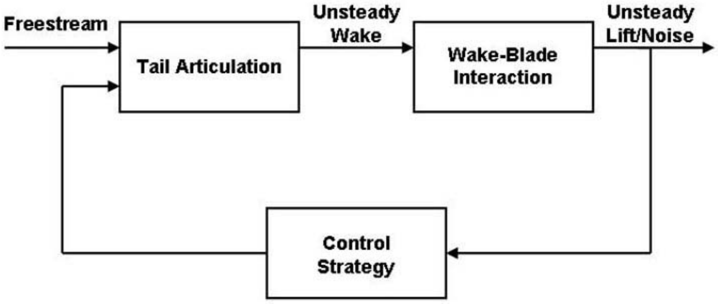

Figure 5-1: Block diagram of closed loop control strategy

As mentioned in Chapter 1, Krol et al [20] chose the simplest possible model to describe the wake due to tail articulation. The authors modelled tail articulation as an arbitrary vorticity input to the stator wake and assumed that the vorticity input at each time would simply be convected downstream with the freestream velocity. Because the position and strength of the shed vortex sheet was known the authors were able to derive a dynamic model directly relating radiated noise to the input vorticity. However, the PIV data presented in Section 4.5.3 shows that this model of vorticity convection is not very good. The vortex sheet behind the active stator moves in two dimensions, rolling up as it moves downstream to form large scale vortex structures at high St. The vortex sheet position is then a nonlinear function of the specific tail motion. This is especially obvious in the nonsinusoidal wake in Figure 4-23 where discrete vortex pairs induce transverse velocities on themselves. Therefore, a correct reduced order model must account for both the creation of vorticity and the nonlinear convection of vorticity in the wake.

The Navier-Stokes equations are the equations governing the full motion of a fluid and can either be written in terms of velocity or vorticity convection. However, the full equations are very difficult to solve and so do not provide an acceptable base for a reduced order model. Simplifying assumptions are often made which reduce the complexity of the Navier-Stokes equations and this is the starting place for many fluid problems. One well developed simplification of the Navier-Stokes equations is that of potential flow. The main assumptions of potential flow are that $\nu = 0$ and $\omega = 0$ everywhere in the flow. These are often reasonable assumptions in high Re aero/hydrodyamics problems where viscous effects are confined to a boundary layer around the solid body. However, even though large scale viscous forces become reduced at high Re effects due to small scale turbulent diffusion become more important and these effects are ignored in potential flow. The assumption that vorticity is zero everywhere in the flow is written:

$$\nabla \times \vec{u} = 0$$

The physical constraint of mass conservation for an incompressible fluid requires that the divergence also be zero:

$$\nabla \cdot \vec{u} = 0$$

Combining these constraints on the velocity field into one another it is seen that the velocity field in a potential flow can be written as the gradient of a single valued potential function, ϕ, which satisfies Laplace's equation:

$$\vec{u} = \nabla\phi = \left(\frac{\partial\phi}{\partial x}\hat{x}, \frac{\partial\phi}{\partial y}\hat{y}\right), \nabla^2\phi = 0$$

Notice that there is no time dependence in the solution of Laplace's equation. Fluid velocities in potential flow change instantly with changes in the boundary conditions, thus unsteady effects are neglected unless specially accounted for. Using potential flow to describe the creation and convection of vorticity by tail articulation may sound odd as vorticity does not exist by definition in a potential flow. However, the point source and point vortex, defined in radial coordinates in Figure 5-2, are two potential functions which can be used to represent many realistic velocity fields which do contain vorticity. The induced velocity field of each of these elements is irrotational and divergence free at every point in the plane except at the point $r = 0$, where a singularity exists. The strength of the induced velocity field decays with $\frac{1}{r}$

and is linear with the defined strength of the singularity, q for the source strength and γ for the vortex strength. Because the velocity fields of these elements satisfy the Laplace equation everywhere outside of the singularity the principle of superposition holds for these elements. Therefore, any combination of point sources and vortices defines a valid potential flow at all points except for the singularities.

Source
$\phi = \frac{q}{2\pi} \ln{(r)}, u_r = \frac{q}{2\pi r}, u_\theta = 0$

Vortex
$\phi = -\frac{\gamma}{2\pi}\theta, u_r = 0, u_\theta = -\frac{\gamma}{2\pi r}$

Figure 5-2: Potential source and vortex

The motion of a two dimensional vortex sheet has been studied extensively using the Lagrangian point vortex method in the context of potential flow [6], [19], [18]. The vortex sheet is approximated by a distribution of discrete point vortex elements, there are no source elements for physical reasons. Each of the free vortex elements has the kinematic condition that it move with local fluid velocity at its singularity. Therefore, the velocity of each discrete vortex element is simply the sum of the velocities induced by all of the other point vortices plus the freestream velocity. This may be written:

$$\begin{bmatrix} \dot{x}_i \\ \dot{y}_i \end{bmatrix} = \begin{bmatrix} U \\ V \end{bmatrix} + \sum_{j=1, j\neq i}^{N} \frac{\gamma_j}{r_{ij}^2} \begin{bmatrix} 0 & -1 \\ 1 & 0 \end{bmatrix} \begin{bmatrix} x_i - x_j \\ y_i - y_j \end{bmatrix} \tag{5.1}$$

where r_{ij} is the radial distance from vortex j to vortex i. Equation 5.1 can be thought of as showing the influence that one vortex element has on another. Notice the rotation matrix present in Equation 5.1, this matrix may be replaced by the identity matrix to give the influence between source elements. Several numerical techniques have been developed to ensure the numerical stability of vortex sheet simulations. One common technique is the application of a smoothing kernel to the induced velocity field so that it does not go to infinity as r goes to 0. However, care must be taken with this approach as the smoothing kernel introduces a physical length scale which must be in line with the physics of the actual problem. In this case the kernel length scale is taken to be δ, the boundary layer thickness at the stator trailing edge. Many analytical and empirical expressions for δ exist, the largest distinction being between laminar and turbulent flow conditions. However, in this work only one expression is used for simplicity, an empirical expression for the fully turbulent boundary layer [23]:

$$\delta = L_{chord}\frac{0.38}{Re^{0.2}} \tag{5.2}$$

Using this value of δ for the physical length scale a gaussian smoothing kernel is applied and the equation used to determine the velocity of each free vortex element is given by:

$$\begin{bmatrix} \dot{x}_i \\ \dot{y}_i \end{bmatrix} = \begin{bmatrix} U \\ V \end{bmatrix} + \sum_{j=1, j\neq i}^{N} \frac{\gamma_j \left(1 - \exp\left(-r_{ij}^2/\delta^2\right)\right)}{r_{ij}^2} \begin{bmatrix} 0 & -1 \\ 1 & 0 \end{bmatrix} \begin{bmatrix} x_i - x_j \\ y_i - y_j \end{bmatrix} \tag{5.3}$$

One commonly studied two dimensional vortex sheet case is the motion of a vortex sheet where all vortex elements have equal strength and spacing. This system has been proven to be unstable, known as the Kelvin-Helmholtz instability, meaning that an equal strength vortex sheet will roll up into discrete vortices after any perturbation [22]. The time scale of this roll up is a function of the vortex strength, smoothing kernel, and perturbation. Vortex sheets of varying strength are unstable as well, with patches of like signed vorticity rolling up together to form discrete vortices. This instability property of the two dimensional vortex sheet explains the dynamic vortex roll up observed in Chapter 4. Therefore, the point vortex method will be used as a starting point for the model of the wake due to active tail articulation.

With the potential vortex method to describe the motion of the vortex sheet the next problem in formulating the reduced order tail articulation block of Figure 5-1 is to describe the creation of vorticity by tail articulation. Computing the flow around airfoils is a well developed area in potential flow, with one important quantity being the bound circulation around the airfoil, Γ, where:

$$\Gamma = \oint \vec{u} \cdot ds$$

where s is the arc-length coordinate system around the airfoil. Γ can be related directly to the lift on the airfoil by:

$$L = \frac{1}{2}\rho U S \Gamma \tag{5.4}$$

Numerical methods for determining the circulation around an airfoil exist and will be discussed more in-depth in Section 5.4. Kelvin's theorem states that the circulation is constant around a material contour in potential flow. Therefore, any change in the bound circulation around the airfoil due to a change in lift requires that an opposite but equal amount of vorticity be shed into the wake [24]. These methods, discussed in Section 5.4, could be used to compute the amount of vorticity shed by tail articulation at each time for a specific tail motion. This vorticity could then be added into the wake as a potential vortex element and allowed to convect by Equation 5.3. This approach is well developed and is a reasonable path to take for a low order model of tail articulation [16]. However, the amount of vorticity shed at each time would have to be numerically computed for each tail motion. While the method would provide a unique solution for the wake due to each tail motion, it would not provide much insight into the mechanisms of tail articulation. Instead, simplifying assumptions about the vorticity shed by tail articulation are made which, although less accurate than numerical methods, provide a more tractable sense of how tail articulation works. The model presented below was derived with D. Wee [36] based off the method in [7].

For inviscid, incompressible flow the Navier-Stokes equations reduce to the Euler equation. Integrating the Euler equations around the stator gives:

$$\oint \frac{\partial u}{\partial t} \cdot \hat{s} ds = \oint (u \times \omega) \cdot \hat{s} ds - \left[\oint \left(\frac{1}{2} \nabla |u|^2 + \frac{1}{\rho} \nabla P \right) \cdot \hat{s} ds \right]$$

The term on the left hand side is the time derivative of the circulation, precisely the term which determines how vorticity is shed by Kelvin's theorem. The first term on the right hand side becomes $\int_S \omega u \cdot \hat{n} dS$ if the magnitude of the boundary layer vorticity is assumed constant around the stator. The terms in brackets on the right hand side are negligible to the same order as the curvature of streamlines and the difference in pressures on each side of the stator. If the no slip condition is enforced on the moving tail flap and small angles are assumed, the component of velocity normal to the stator surface is simply the velocity of the stator surface and the surface normal remains constant so that:

$$\oint \frac{\partial u}{\partial t} \cdot \hat{s} ds \approx -\frac{U L_{tail}}{\delta} v_{tip}$$

where v_{tip} is the velocity of the tail tip. This expression gives the vorticity shed by the stator as a constant multiplied by the velocity of the stator tail flap. The equation above is multiplied by one half from the equation in [36] due to the triangular velocity profile of the hinged tail flap. If the equation is discretized to be implemented numerically, then at each time step the net vorticity shed by the stator is:

$$\gamma_{net}(t) = -\frac{U L_{tip} \Delta t}{\delta} v_{tip}(t) \qquad (5.5)$$

where Δt is the discrete time length. Equation 5.5 is exactly what was desired for a reduced order model of the vortex wake due to tail articulation. It shows clearly the relevant parameters in tail articulation and their influence on the vorticity shed into the stator wake. It is seen that moving the tail faster will cause higher amounts of vorticity to be shed. This agrees with the observation in Chapter 4 that the magnitude of vorticity increases as f increases. This also explains why vortex sheet roll up occurs more strongly with increasing f. Imagining the discretized position of the tail as a series of step functions, every step in position requires an impulse in velocity which then introduces a discrete vortex element into the wake. Equation 5.5 also gives insight into the use of actuation other than tail articulation, such as the general deformation of the entire stator or use of suction and blowing instead of tail articulation. Initial simulations of the stator wake shed one vortex element per time step with strength given by Equation 5.5 and then convected all free vortices by Equation 5.3. This model proved quite successful at capturing the overall shape of the active wakes seen in Chapter 4. However, by shedding only one vortex per time step the model was not able to capture the baseline wake deficit. This is because, by Equation 5.5, when there is no tail articulation there is no net vorticity shed. Thus there will be no baseline wake effects behind the stator if only one vortex is shed at each time. If the reduced order model of tail articulation is used to find an optimal tail motion for reduction of unsteady blade forces it must be able to capture the baseline wake deficit. Figure 4-10 relates the shedding of boundary layer vorticity on top and bottom of the stator to the wake deficit. Therefore, when there is no tail motion the reduced order model of tail articulation should simply shed two baseline vortex elements from the stator to account for the baseline wake deficit. When there is tail motion and thus a net vorticity shed, half of the net vorticity can be added to the top baseline vortex and half to the bottom baseline vortex. As previously mentioned, there is a physical time scale associated with the diffusion of stator vorticity into the wake. However, in these simulations vorticity is shed into the wake instantaneously.

5.2 Reduced Order Model of the Baseline Wake

The remaining challenge in simulating the vortex wake is to estimate both the strength of the shed boundary layer vorticity and the initial separation between the shed baseline vortices, Figure 4-10. This should be done so that the simulated wake closely matches LDV and PIV measurements of the real wake deficit. As seen in Figure 3-5, static tail deflections result in a wake deficit that is both deflected and deeper. The deflection of the wake is partially due to the steady deflection of the tail tip and partially due to the influence of the starting vortex. The starting vortex is a common idea in potential flow, it is the amount of vorticity shed when an airfoil is impulsively started. Equation 5.5 accounts for the starting vortex as long as the tail tip is initially at zero deflection and is then impulsively changed to the final static deflection. The deepening of the stator wake, on the other hand, is indicative of an increase in γ_0 due static tail deflections. This is not surprising as the asymmetric pressure distribution over the lifting stator will affect the boundary layers on each side of the stator. A first order, linear dynamic model will most likely be sufficient to describe the change in γ_0 with tail deflection. However, sufficient PIV data has not been collected in order to develop this model. Therefore, the value of γ_0 will remain constant in these simulations and deepening of the wake deficit due to tail deflections will be unaccounted for.

The vortex strength shed from the boundary layer may be thought of as the amount of boundary layer vorticity, $\omega = \frac{\partial u}{\partial y} \approx \frac{U_\infty}{\delta}$, convected out of the stator boundary in a certain time, $\gamma_0 = \frac{1}{2}\omega\delta U\Delta t$. These equations lead to the absolute discrete vortex strength shed from top and bottom of the stator at each time step:

$$\gamma_0 = \frac{1}{2}U^2\Delta t \tag{5.6}$$

The separation between vortex elements will likely also be a function of both tail displacement and U. However, the assumption that this distance is constant is correct to the same order that γ_0 and δ are assumed constant. Therefore, using Equation 5.6 for the strength of the shed vorticity the initial separation between discrete vortex elements at the tail tip is found by matching experimental data in Chapter 3. It was found that by using the value of δ for this separation the simulated wake deficit matches that found in Figure 3-4 quite well. A comparison of these wakes is shown in Figure 5-3.

Note that in the reduced order model of tail articulation the number of vortex pairs shed per flapping period, N, and Δt are relevant parameters even when there is no active flapping. This is because these parameters, along with U, determine the relative spacing of vortex elements in the wake and thus the wake resolution. In Section 5.1, N of 48 is used and f is noted even when there is no active tail articulation. It should also be stated that the strength of each vortex element remains constant throughout the entire simulation. Techniques which attempt to account for viscous forces on

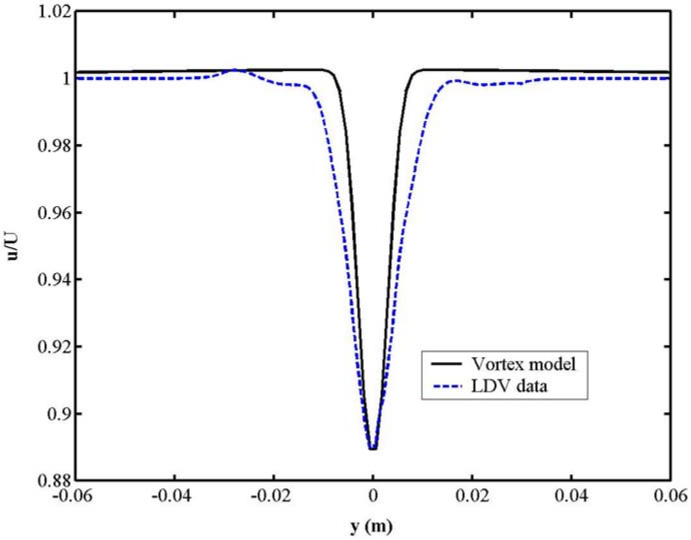

Figure 5-3: Baseline u/U for U = 1 (m/s)

the vortex elements, such as core spreading, were considered but not implemented in the current version of this simulation. The effect of core spreading by viscous forces is seen in the PIV measurements of the baseline stator deficit wake in Figures 4-11 through 4-13. Shed vortex elements are seen in the simulated baseline wake in Figure 5-4.

5.3 Reduced Order Model of Active Sinusoidal Articulation

Figures 5-5 through 5-16 are now presented, showing the position of vortex elements in the simulated wake for the cases that PIV data is given for in Section 4.6. In order to better relate the simulated wake to the data in Section 4.6, the relative size between the markers for positive and negative vortex elements is adjusted to reflect the net vorticity contained in each discrete vortex pair. If there is no net vorticity in the vortex pair then the positive shed boundary layer vortex, shown as a red circle, and the negative shed boundary layer vortex, shown as a blue square, will be the same size. If $\gamma_{net} > 6\gamma_0$ then only the positive vortex element is displayed, at a larger

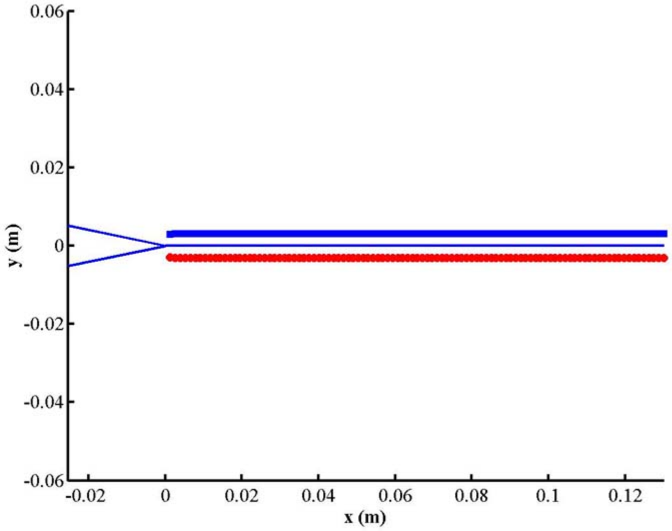

Figure 5-4: Vortex elements in baseline wake for $f = 912$ (rpm), $A = 0$ (deg), $U = 1$ (m/s)

size. Conversely, if $\gamma_{net} < -6\gamma_0$ then only the negative vortex element is displayed, again at a larger size. If $-6\gamma_0 < \gamma_{net} < 6\gamma_0$ then the relative size of each vortex in the shed pair is scaled to represent the net vorticity contained in the shed vortex pair.

5.3.1 Quasi-Steady Wake Spreading

At low St the simulated vortex wake is seen to spread out in a quasi-steady fashion. The wake deflects less for the lowest St case, Figure 5-5, than for the next higher St case, Figure 5-6, matching observations by PIV. The simulated vortex sheet also alternates between a net positive and net negative vortex sheet by Equation 5.5.

5.3.2 Vortex Roll Up

At cases of moderate St the simulated wake is seen to begin to roll up into discrete vortices. This is seen as the vortex core becomes tighter in the downstream vortex in both Figures 5-7 (just off the plot) and 5-8. This effect can be seen in the PIV data, but less so. However, the general orientation and position of the vortex sheet is very similar between the simulated and PIV plots.

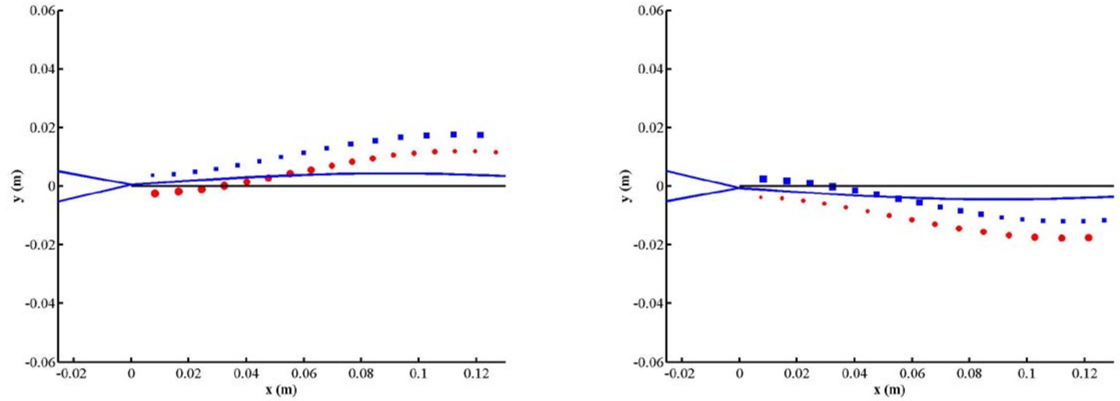

Tail phase = -π Tail phase = 0

Figure 5-5: Vortex elements for f = 459 (rpm), A = 10 (deg), U = 3 (m/s), St = 0.023

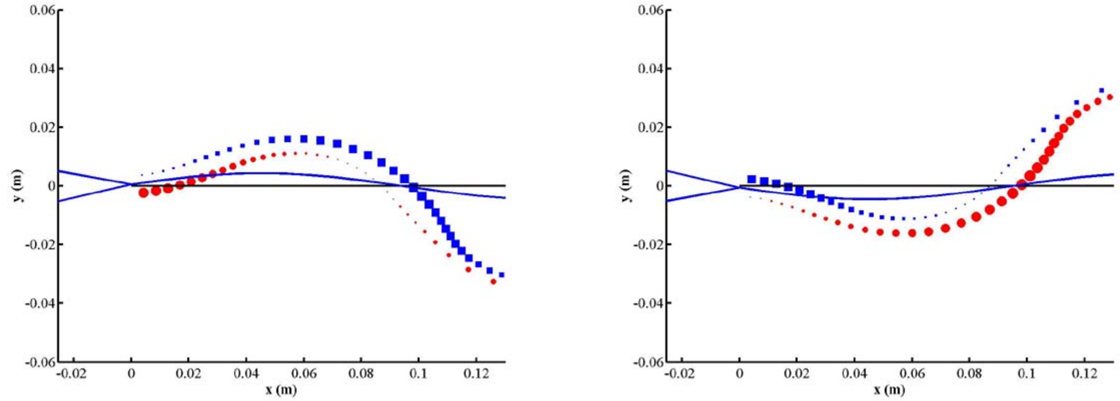

Tail phase = -π Tail phase = 0

Figure 5-6: Vortex elements for f = 912 (rpm), A = 10 (deg), U = 3 (m/s), St = 0.045

5.3.3 Strong Vortex Regime

Simulated wakes at high St roll up into tight discrete vortices. The issue of vortex lag discussed in Section 4.6.3 is not seen in the simulated wakes, Figures 5-9 and 5-10. Instead, the x position of the vortex centers appear to form and stay in line with the x position corresponding to zero tail displacement. For sinusoidal tail motions, the zero tail displacement corresponds to the highest tail velocity and thus the highest value of γ_{net}. It is possible that the lag phenomenon noted in Section 4.6.3 would be accurately described if the dynamic model were changed to account for the varying

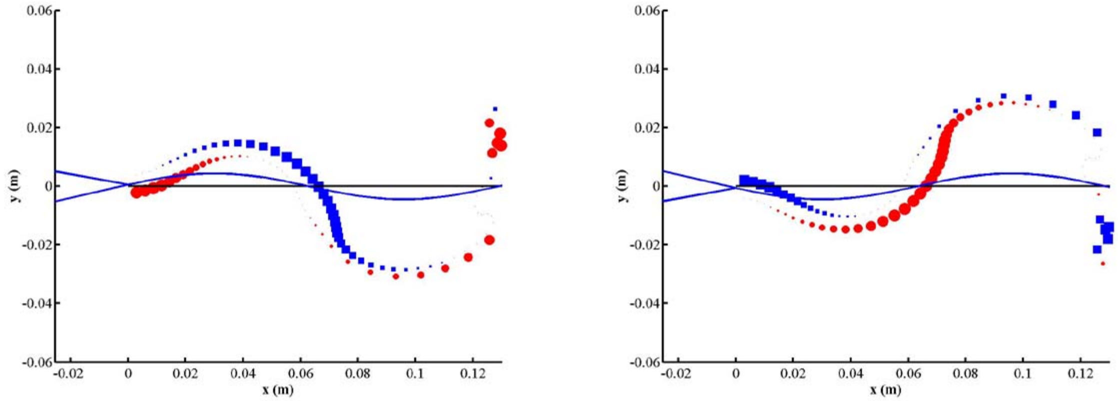

Tail phase = -π

Tail phase = 0

Figure 5-7: Vortex elements for f = 912 (rpm), A = 10 (deg), U = 2 (m/s), St = 0.065

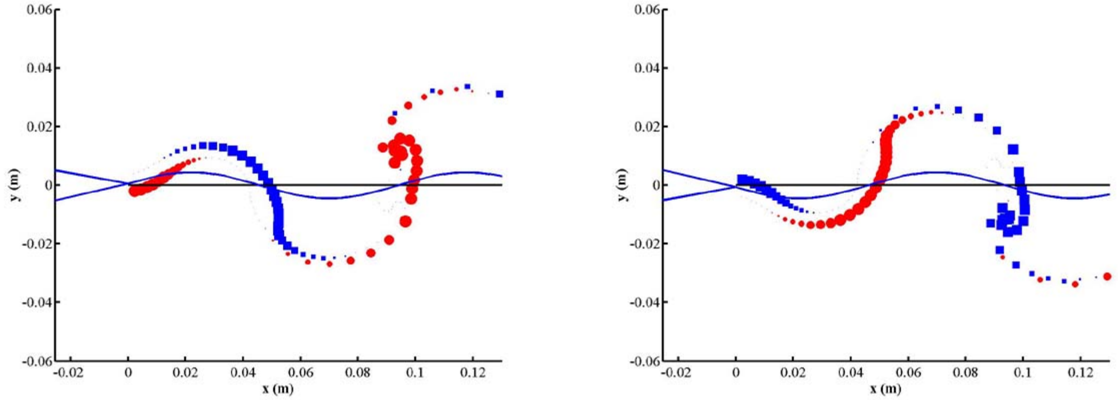

Tail phase = -π

Tail phase = 0

Figure 5-8: Vortex elements for f = 1252 (rpm), A = 10 (deg), U = 2 (m/s), St = 0.089

strength of γ_0, viscous forces, and the time scale of vorticity diffusion into the stator wake.

5.3.4 St Observed in Strong Vortex Wake

The measurement of St in the wake was repeated for the simulated strong vortex wake cases. To make a fair comparison with results in Section 4.6.4, simulated velocity data is calculated over the same grid that PIV data was recorded on and the same analysis in Section 4.6.4 is then performed. The simulated vorticity with tracked vortex centers

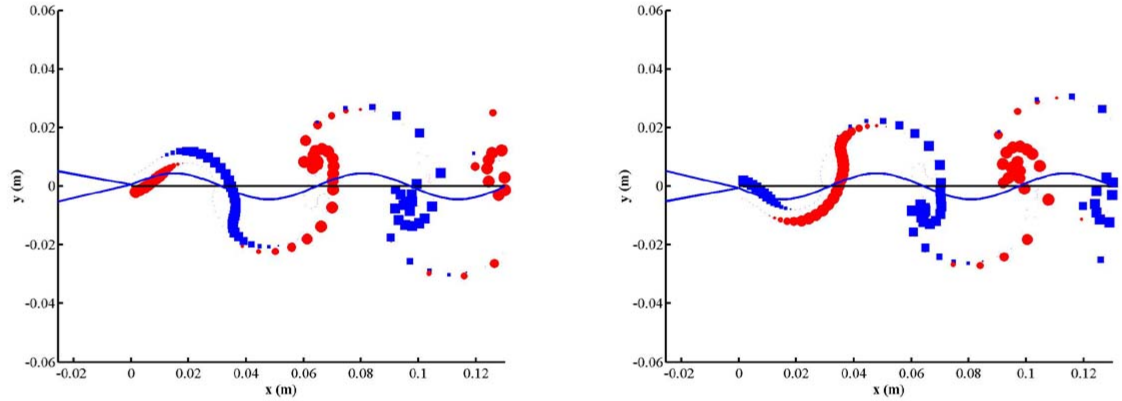

Tail phase = -π

Tail phase = 0

Figure 5-9: Vortex elements for f = 912 (rpm), A = 10 (deg), U = 1 (m/s), St = 0.136

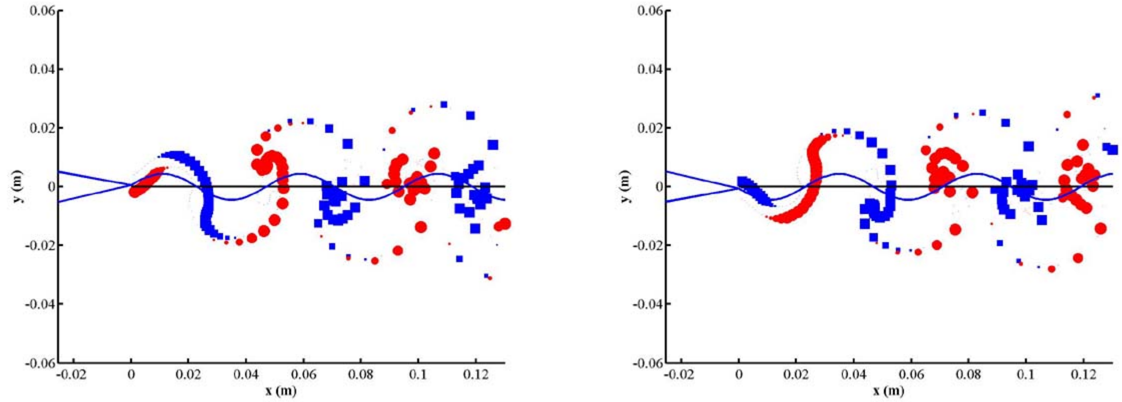

Tail phase = -π

Tail phase = 0

Figure 5-10: Vortex elements for f = 1252 (rpm), A = 10 (deg), U = 1 (m/s), St = 0.186

and St in the wake is shown for each case in Figures 5-11 and 5-12. It is found that St in the simulated wake is slightly more than half of that computed with A as tail tip deflection, agreeing with observations in Section 4.6.4. In the simulated wake there does not appear to be any decrease in St with time. This is likely due to the absence of viscous forces.

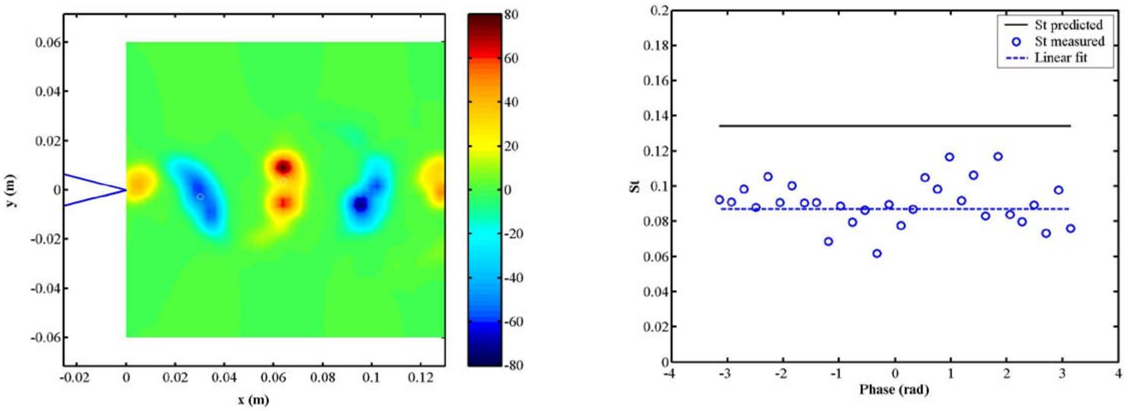

Tracked SIM vortex centers

St vs phase (rad)

Figure 5-11: St in the simulated wake for $f = 912$ (rpm), $A = 10$ (deg), $U = 1$ (m/s)

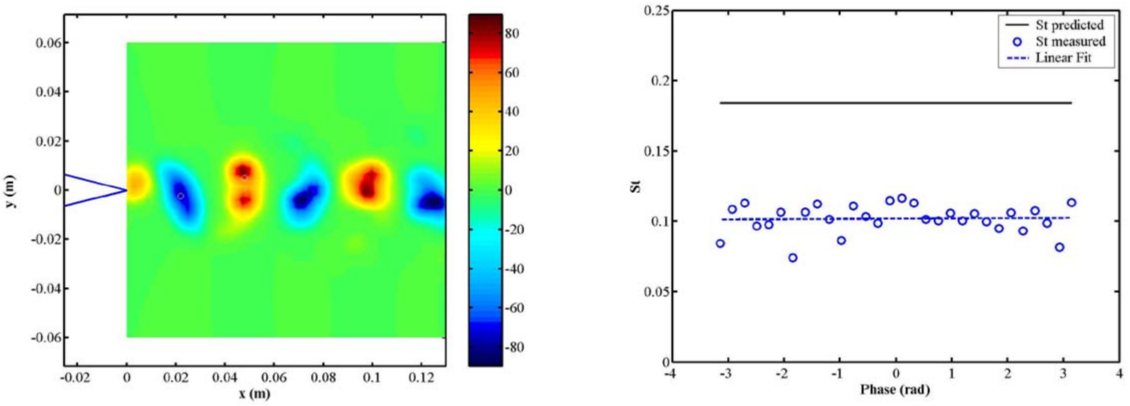

Tracked SIM vortex centers

St vs phase (rad)

Figure 5-12: St in the simulated wake for $f = 1252$ (rpm), $A = 10$ (deg), $U = 1$ (m/s)

5.3.5 Active Nonsinusoidal Tail Articulation

Nonsinusoidal tail motions are simulated for the same parameters as those in Section 4.6.5. The first simulated case is that of the Modified Sinusoid with $n = 0.25$, Figure 5-13. This simulated wake bears close resemblance to the experimentally measured wake. It is noted that the high tail velocity associated with the step like change in velocity in this motion results in the release of shed vortex pairs with relatively large γ_{net}. This causes tight vortex cores to form with relatively large spacing compared to sinusoidal motions. It is also noted that the dynamics related to steady state tail deflection discussed in Section 5.2 will be relatively more important in this case due to the long periods of time the tail spends at a quasi-steady tail deflection.

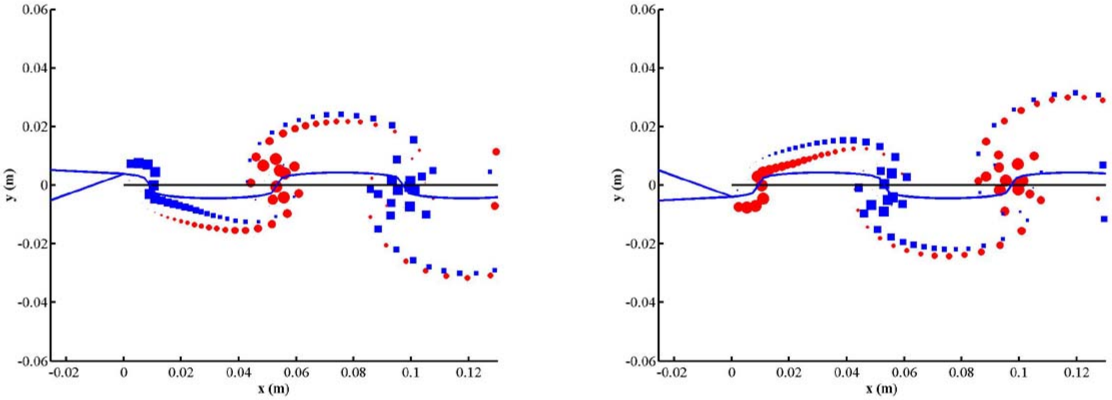

Tail phase = -π

Tail phase = 0

Figure 5-13: Vortex elements for Modified Sinusoid f = 11.36 (Hz), A = 10 (deg), U = 1 (m/s), n = 0.25

The next simulated tail motion is that of a Modified Sinusoid with n = 4, Figure 5-14. Again it is seen that four distinct large scale vortices form per period and move with transverse velocities. Equation 5.5 shows that this is due to the large spacing between impulse-like tail motions in the same direction. Therefore, shed vorticity convects downstream before more vorticity of the same sign is shed and the two patches are far enough apart to roll up into separate vortices. Equation 5.3 shows why these unevenly spaced vortex pairs induce transverse velocities on themselves.

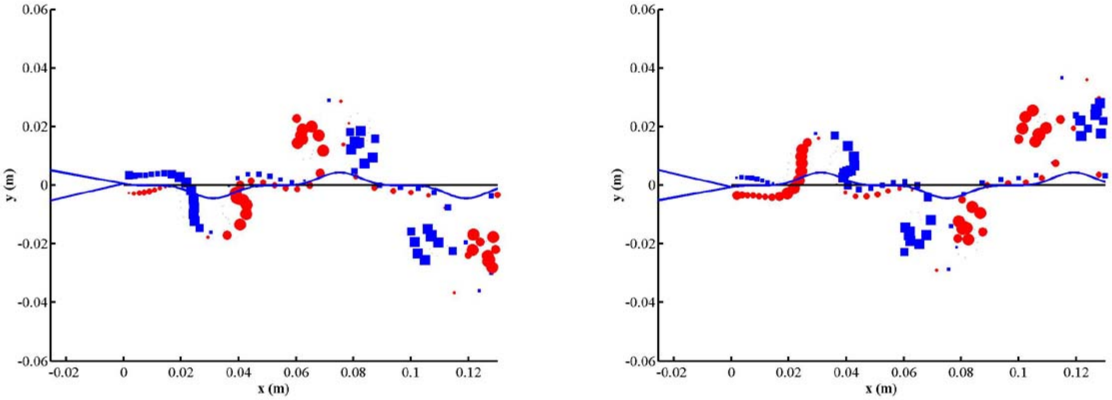

Tail phase = -π

Tail phase = 0

Figure 5-14: Vortex elements for Modified Sinusoid f = 11.36 (Hz), A = 10 (deg), U = 1 (m/s), n = 4

Simulation of the Generalized Sinusoid with $Ratio = 2$ and $Theta = 1$ also compares well to experimental data, 5-15. It is seen that the uneven velocities due to 'stretching' of the sinusoid create uneven amounts of vorticity in the wake, with the stronger vorticity rolling up more quickly.

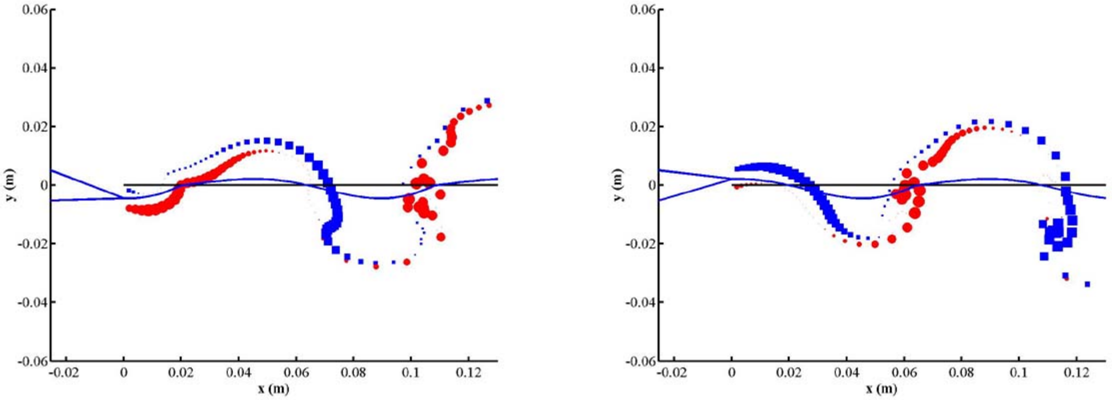

Tail phase = -π Tail phase = 0

Figure 5-15: Vortex elements for Generalized Sinusoid $f = 11.36$ (Hz), $A = 10$ (deg), $U = 1$ (m/s), $Ratio = 2$ and $Theta = 1$

Finally, simulation of the Generalized Sinusoid with $Ratio = 1$ and $Theta = 0.67$ is shown, Figure 5-16. The 'squishing' of the sinusoid creates an unequal distribution of vorticity which gives the wake it's unique shape.

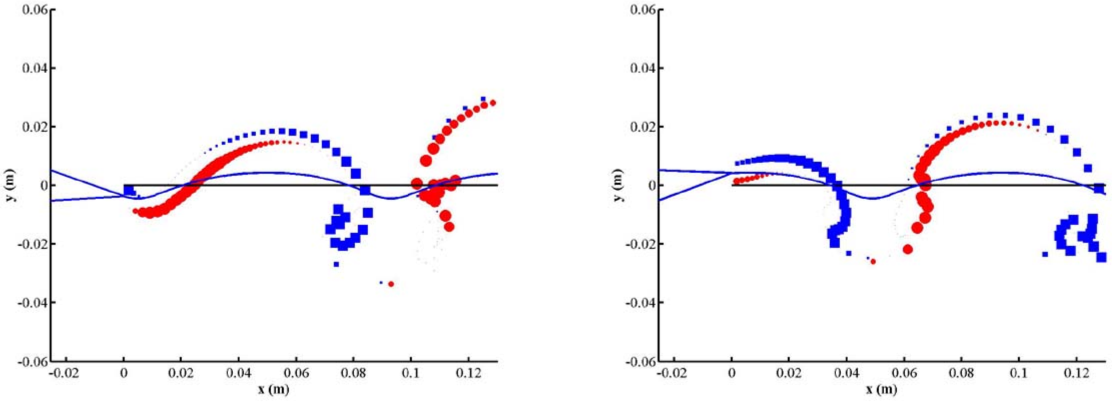

Tail phase = -π Tail phase = 0

Figure 5-16: Vortex elements for Generalized Sinusoid $f = 11.36$ (Hz), $A = 10$ (deg), $U = 1$ (m/s), $Ratio = 1$ and $Theta = 0.67$

5.4 Low Order Propeller Force Simulation

In order to quickly estimate the effect that a given tail articulation will have on radiated noise reduction an airfoil panel method is used to estimate the forces on a virtual two dimensional blade passing through the wake. These forces do not give radiated noise but the two are related by Equation 1.1. Airfoil panel theory is a numerical method, based on potential flow theory, for determining the forces on arbitrary shaped bodies which was developed in the 1960's by Hess and Smith [13], [12]. The method assumes that a lifting body may be well represented by N_{blade} discrete panels. A continuous distribution of sources and vortices line the airfoil perimeter, with source strengths constant on each panel and the vortex strength constant around the entire airfoil. There are therefore N_{blade} values for the airfoil sources and 1 value for the vortex strength. The values of these strengths are solved for at each time to enforce boundary conditions on the airfoil. Because potential flow does not include viscous effects the boundary conditions on the airfoil are no flow through each panel midpoint rather than the no-slip condition. These no flow conditions give N_{blade} constraint equations, a final constraint equation is made by the Kutta condition which requires the pressure difference across the trailing edge be zero. With $N_{blade} + 1$ unknowns and $N_{blade} + 1$ constraint equations, the source and vortex strengths are solved for at each time using LU decomposition. Once the vortex and source strengths are known the tangential velocity at each panel midpoint may be solved by integrating Equation 5.1 around the airfoil. The pressure at each panel midpoint is found by Bernoulli's equation:

$$P = \frac{1}{2}\rho\left(U_{blade}^2 - U_{tan}^2\right)$$

Pressure on each panel is integrated around the airfoil to determine the lift and pressure drag forces on the airfoil. The vortex and source strengths on each panel also induce an additional velocity on each of the free stator wake vortices, again by integrating Equation 5.1 around the airfoil. Because the airfoil's induced velocity field is solved to be tangent to the blade surface the wake vortex elements will be forced to move around the airfoil rather than pass through it. Several invalid assumptions are made in using the two dimensional panel method to predict propeller forces, the first is the two dimensional assumption. A real propeller has variable pitch so that each blade section encounters inflow at the same desired angle of attack. This introduces a significant three dimensional quality to the flow that is lost in a two dimensional analysis. Three dimensional panel methods do exist and are more appropriate to this problem. However, three dimensional simulations are much more time consuming than two dimensional simulations due to the much higher number of panels required. Therefore, the two dimension assumption will be used in order to make quick propeller force estimates and these will then be compared with results from a more appropriate three dimensional method in Section 5.5. A second invalid assumption is the disregard of unsteady effects. Unlike potential flow, real fluids cannot change velocity or pressure instantly. Unsteady lifting airfoil methods exist which do not explicitly solve for panel strengths about the airfoil at each time step but remember past values and iterate until the Kutta condition is met. Effort to include unsteady effects in the low order blade force model is not made at this time because unsteady effects are accounted for in the three dimensional propeller simulation in Section 5.5. The final incorrect assumption made is that boundary layer effects on the propeller blade are negligible. This is likely to be incorrect because the blade and its boundary layer are of similar size to the stator and it's shed vorticity. However, because the propeller inflow, $U_{blade} = \sqrt{U^2 + (r\Omega)^2}$, is generally much larger than U this assumption is more acceptable. In order to partially account for the propeller blade vortex shedding additional wake vortices are adding at the trailing edge of the propeller blade section. This is similar to the method of Basu and Hancock [5], but does not implement the shed vortex as an additional airfoil panel and does not iteratively solve for the shed vortex along with the panel strengths. Instead, the shed blade vortex is simply initialized at a location determined by the velocity at the trailing edge and it's strength is the change in Γ on the airfoil panels between time steps by Kelvin's theorem. The panel code is compared to known steady lifting airfoil data in [1] to verify its accuracy, Figure 5-17.

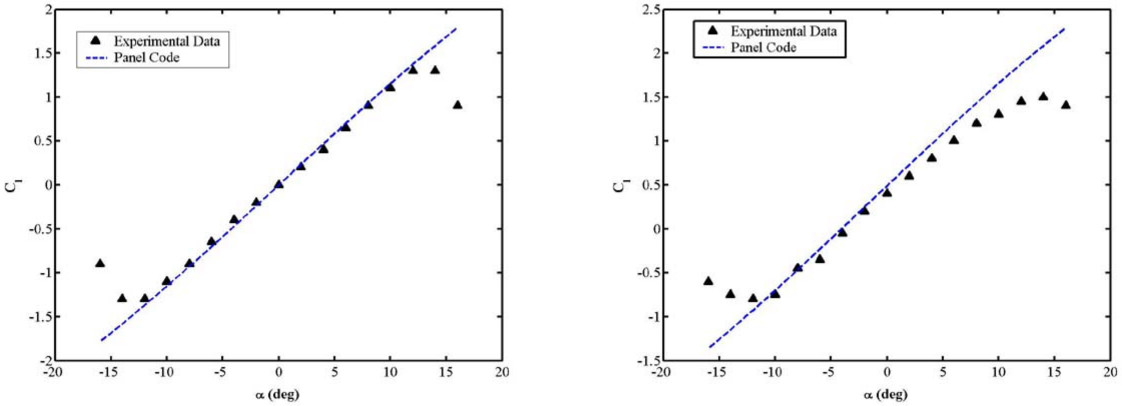

NACA 0009 NACA 4412

Figure 5-17: C_l for $Re = 3\text{E}5$

In an actual AUV a lifting propeller blade is used to produce thrust which propels the vehicle. A lifting blade has a nominal bound circulation given by Equation 5.4, which results in a nominal non-zero vortex strength on each blade panel. This vortex strength induces a velocity on all of the free wake vortices, proportional to the lift on the blade. In other words, the more lift produced by the propeller blade the more the blade will affect the wake. While this effect is accounted for in the two dimensional blade simulation it is not sufficient to describe the complex three dimensional effects of a real lifting blade wake interaction. Therefore, simulations with the two dimensional blade model will be limited to nominally non-lifting blades. Specifically, a NACA 0012 airfoil section will be used and set at $\alpha = 0$ degrees, Figure 5-18. This blade will minimally affect the wake, allowing the two dimensional assumption to remain as correct as possible. In this case any deviation of lift from 0 is an unsteady blade force. It is hoped that observations from the non-lifting case will extend to the lifting case. This will be evaluated once a three dimensional coupled blade wake interaction model is available or during experiments.

Before simulating the two dimensional propeller blade passing, the stator wake is simulated for $N_{periods} = 5$ full periods to allow start up transients to pass and the wake to come to a steady state. The tail motion is damped for the first 2 periods, which was found to help the wake come to steady state more quickly. After this start up time the blade leading edge is initialized at location $x_{start} = 0.0762$ (m) and

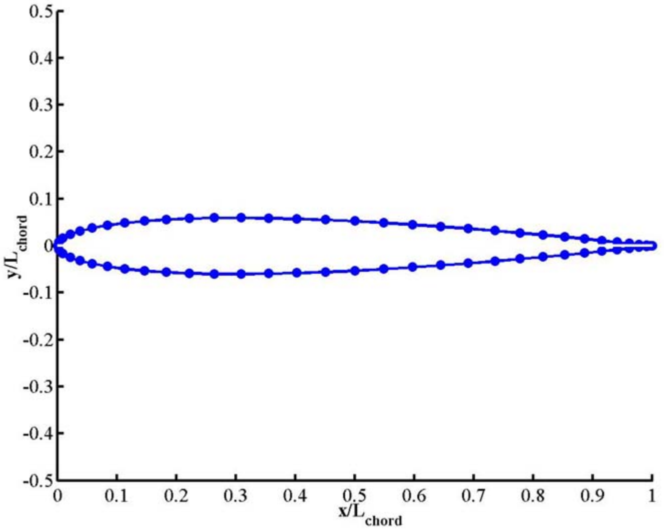

Figure 5-18: NACA0012 non-lifting propeller blade section

$y_{start} = 0.0612$ (m). The two dimensional blade section simulated is at radius $r_{blade} = 0.0762$ (m) which gives $v_{blade} = \pi r f = 3.6387$ (m/s). Because the simulation is in two dimensions the lift per span, L/S, is computed rather than L which would require three dimensional considerations. At each time step the blade section's y position is moved by $-v_{blade}\Delta t$, the wake vortex induced velocities are computed at each panel midpoint, the blade source and vortex strengths are solved for, L/S is computed, the motion of the wake vortices due to panel strengths is computed, and finally the blade trailing vortex is added. Every N_{res} time steps another vortex pair is shed from the stator trailing edge, with a total of N shed vortex pairs per stator period. The number of induced velocities that must be calculated during the blade simulation is of order N^3. The number of vortex pairs shed per period is desired to be low so that simulations may be done quickly but high enough that blade forces are captured. L/S computed as the blade passes through both the baseline wake and an unsteady wake is shown in Figure 5-19 for increasing values of N. It is seen that the L/S computed converges sufficiently after N =24, this value of N is used in the following two dimensional blade force simulations. The vortex elements and two dimensional blade section during the baseline and unsteady blade wake interaction are shown in Figure 5-20.

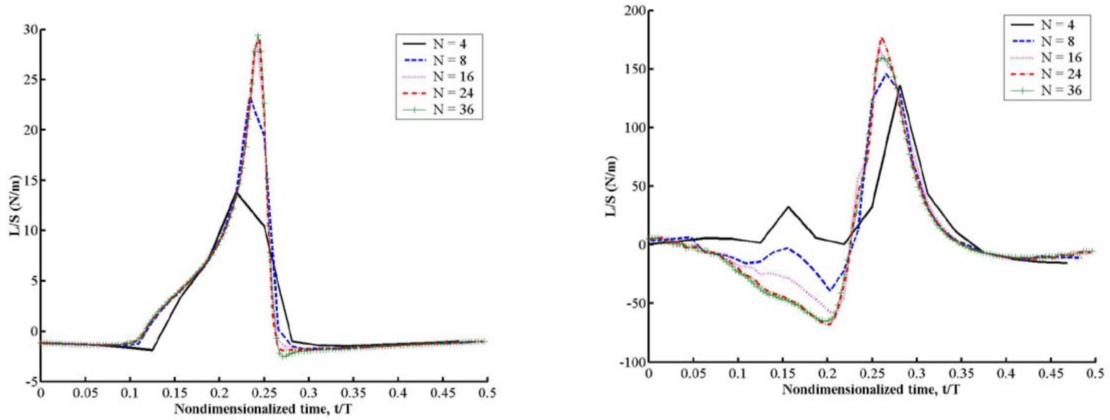

$f = 912$ (rpm), $A = 0$ (deg), $U = 1$ (m/s)

$f = 912$ (rpm), $A = 10$ (deg), $U = 1$ (m/s)

Figure 5-19: L/S (N/m) for wake blade interaction for varying N, $T = 0.1316$ (s)

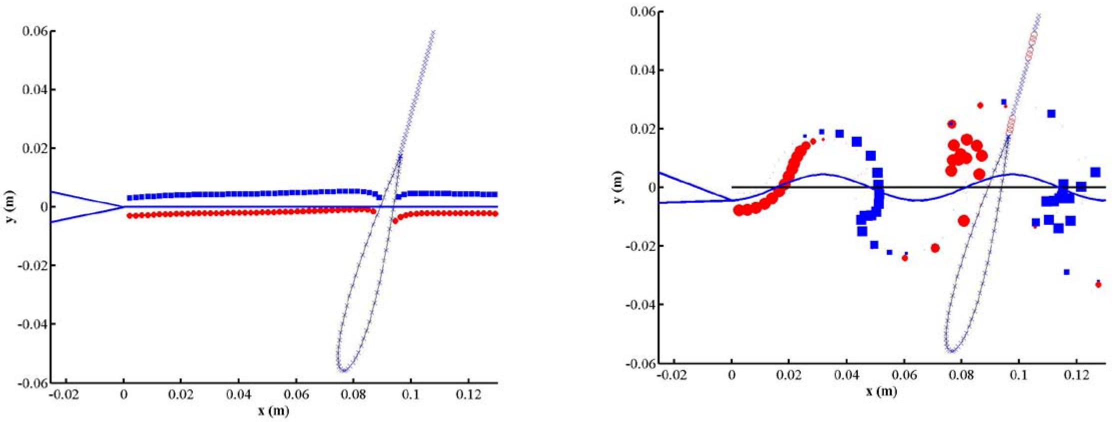

$f = 912$ (rpm), $A = 0$ (deg), $U = 1$ (m/s)

$f = 912$ (rpm), $A = 10$ (deg), $U = 1$ (m/s)

Figure 5-20: Simulated blade vortex interaction for baseline and unsteady case

5.4.1 Low Order Propeller Force Simulations in the Unsteady Wake

The number of stators and propeller blades on an actual vehicle are set by mission criteria and other design criteria. With no specific vehicle in mind, the present work is limited to the following case: a two bladed propeller rotating at one half of the stator flapping frequency, f. This ratio is chosen so that there is one flapping period per blade passing and each blade passes through the stator wake at the same phase. Setting the propeller blade frequency relative to f in different ways will result in other effects. For instance if the blade and flapping frequencies are chosen so that there is beating between them, the propeller will experience a slightly different stator wake at each passing due to the varying stator wake blade interaction. In this case, radiated tonal noise is expected at the beating frequency, which is lower than both the blade passing and flapping frequencies. However, the purpose in this work is to find an optimal wake blade interaction so these secondary effects are ignored for the present time. To further cut down the number of test cases the investigation is limited to the optimal tail motion at $U = 1$ m/s, which will be the easiest case to verify experimentally due to lower frequency requirements. The effects that changing the remaining parameters f, A, and phase have on L/S are shown in Figures 5-21 through 5-23. In Figure 5-21 notice that the baseline unsteady lift increases with f due to higher U_{blade} with increasing blade rate. However, the lift does not increase by U_{blade}^2 due to smaller changes in α at higher blade velocities.

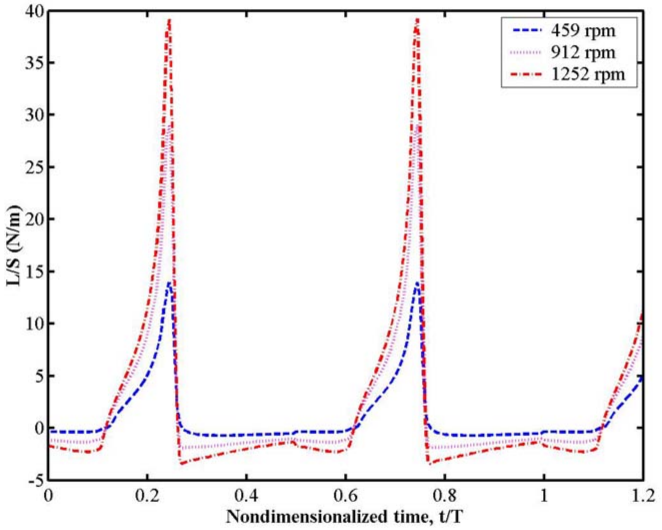

Figure 5-21: L/S as function of f (rpm), $T = 0.1316$ (s)

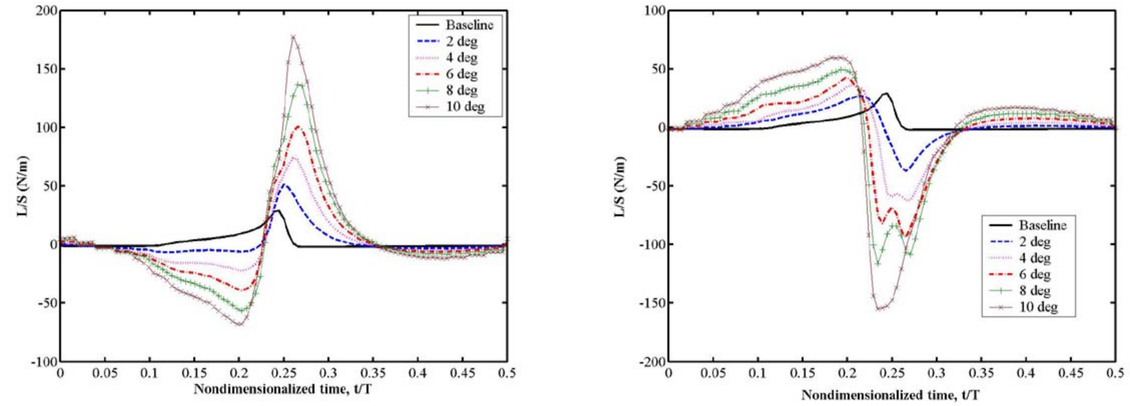

Phase = 0 rad　　Phase = π rad

Figure 5-22: L/S as function of A (deg), $T = 0.1316$ (s)

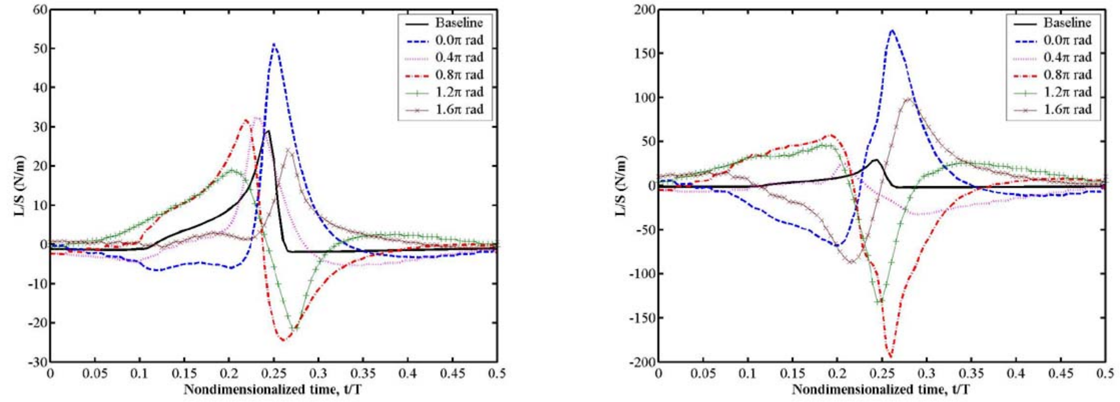

$A = 2$ (deg)　　$A = 10$ (deg)

Figure 5-23: L/S as function of phase (rad), $T = 0.1316$ (s)

5.4.2 Tail Motion Optimization

Initial attempts are made to find a tail motion which results in optimal reduction of unsteady forces. With $U = 1$ m/s, if f is set to 912 rpm and A is constrained to the range $0 < A < 10$ (deg) then the range of St $0.0 < St < 0.136$ is covered. This range of St includes all three of the noted wake regimes; quasi-steady, vortex roll up, and strong vortex wakes. This variety is ideal because it is unknown which wake regime will lead to the best reduction of unsteady blade forces. Setting one value for f is beneficial because the nominal propeller inflow velocity is constant and two dimensional forces may be compared easily. A parametric study using only sinusoidal motions is made with the two dimensional blade force simulation, Figure 5-24. At each data point the stator wake and blade passing are simulated and the maximum values of peak to peak L/S and $\dot{L}/S$ are recorded.

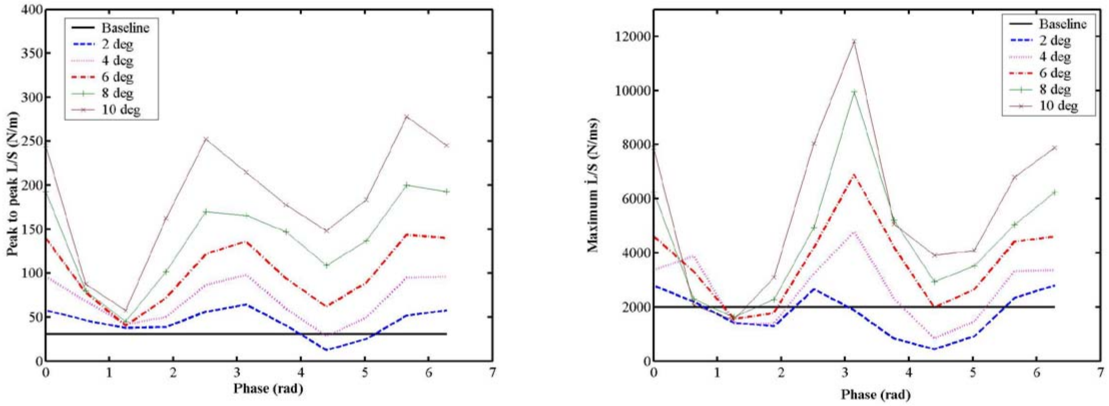

Peak to peak L/S (N/m) Maximum $\dot{L}/S$ (N/ms)

Figure 5-24: Sinusoidal parameter study for $f = 912$ (rpm), $0 < A < 10$ (deg), $U = 1$ (m/s), $0.0 < St < 0.136$

It is seen that, in general, tail articulation does not appear to lead to lower unsteady blade forces. In fact, in most cases tail articulation increases unsteady forces due to the blade wake interaction worse. However, tail articulation does seem to reduce unsteady blade forces more at certain phases than at others, with smaller amplitude motions being better overall. Specifically the case with $A = 2$ (deg) and phase $= 1.4\pi$ appears to reduce both the maximum peak to peak L/S and the maximum $\dot{L}/S$. This suggests that the wake due to this active tail motion may lead to tonal noise reduction. St for this tail motion is 0.027 and it is noted that this will be a maximum drag wake if the same C_d to St relationship shown in Figure 3-12 holds at $A = 2$ degrees.

Small parametric studies were made of the nonsinusoidal tail motions investigated in Section 4.6.5. However, there was no immediately apparent advantage of any of these motions over sinusoidal motions. It would be possible to do a very large parametric study of nonsinusoidal tail motions. However, this search would be very computationally expensive. With $N = 24$, one simulation requires approximately 300 seconds to complete. Completing a full parametric search with 7 levels of A, 10 of phase, 3 of n, 3 of $Ratio$, 3 of $Theta$, and 2 levels used to define the direction of the asymmetry in the Generalized Sinusoid would require 3780 blade simulations. This simulation would take just over 13 days to complete. This amount of time is feasible, however a tail motion optimization based on Gauss-Newton and Conjugate-Gradient methods would be more efficient. Furthermore, this type of optimization might lend itself to use in the real time control law which completely defines the optimal tail articulation. This control law could then be used in experiment. Alternatively, the definition of the tail velocity as a series of velocity impulses gives N free parameters to optimize. Restricting the search to periodic tail motions, $\sum N = 0$, would give $N - 1$ parameters to optimize. This type of search could be aided by data from the simulation about which vortex pairs where interacting in a 'good' or 'bad' way with the blade section. There is also the strong possibility that nonperiodic motions might be desirable. However, experimental verification of the accuracy of the reduced order model for transient tail motions is required before nonperiodic motions can be considered.

5.5 High Resolution Frozen Wake Propeller Unsteady Force Simulations

As previously mentioned, three dimensional vortex lattice methods have been developed and are better suited to simulating the wake blade interaction than the low order two dimensional panel method in Section 5.4. These programs are computationally advanced and writing one is beyond the scope of this project. However, a well developed code was made available by the same ONR ULI partnership with NUWC that allowed the use of the water tunnel and velocity measurement equipment in Chapters 3 and 4. The Propeller Unsteady Force code, PUF, was developed by J. Kerwin et. al. at MIT for optimizing the design of underwater propellers [17], [11]. PUF predicts unsteady blade forces and pressures due to the time varying vortex lattice method which models the blade and wake vorticity. Since its inception several improvements have been made to the PUF code including the ability to simulate turbulent and unsteady propeller inflows by S. Huyer at NUWC [15], [14]. S. Huyer helped to adapt the PUF code to this project and D. Beal developed a routine to design the three dimensional non-lifting propeller blade geometries used in these simulations. It is recommended that these same propeller designs be used in further experimental work in order to compare future results to this work. The propeller blade and swept path used in the following simulations is shown in Figure 5-25.

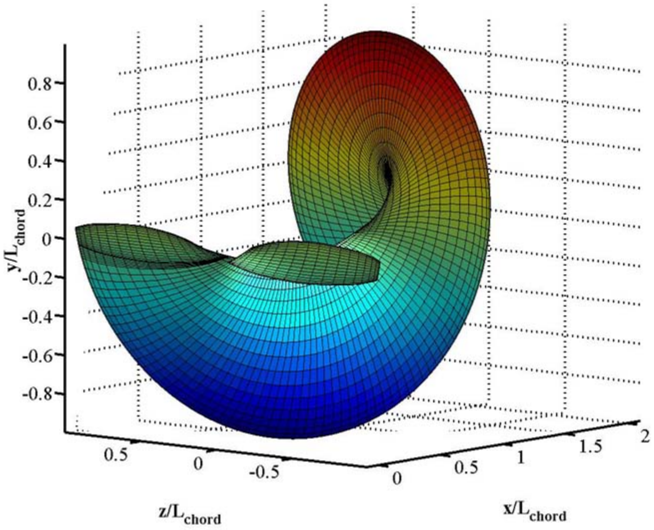

Figure 5-25: PUF blade geometry

5.5.1 Proper Orthogonal Decomposition of Vortex Modes

It would be possible to build a totally coupled Lagrangian three dimensional stator vortex shedding and blade vortex interaction simulation. This would provide the most realistic simulation of the blade vortex interaction and allow for totally automated optimization of tail motion. However, in practice three dimensional vortex filaments are much more complicated than the two dimensional point vortices used in Sections 5.1 and 5.4. Therefore, the existing PUF code was not adapted to included a coupled vortex shedding model as in the low order blade force simulations of Section 5.4. Instead, velocity data taken from PIV measurements and reduced order tail articulation simulations, noted as SIM data, is used to compute the propeller inflow in a "frozen-wake" approach. Two dimensional PIV and SIM velocity data is simply extended in the $\hat{z}$ direction by the two dimensional assumption. This inflow velocity is then used to compute the velocities on each blade panel at every time step in the PUF simulation. Three dimensional vortex strengths are then solved to enforce no flow through the blade surface conditions at each time step. Source elements are used to account for blade thickness and unsteady effects are accounted for. The propeller blade sheds vorticity into its wake which affects the lift on the blade at later time steps. However, the blade panel strengths and shed vorticity do not alter the inflow velocity data in return. This is the "frozen-wake" assumption, again partially justified by the use of non-lifting blades. With this approximation the main implementation problem in the PUF simulation became how to compute the propeller inflow velocity at each time step from the experimental or simulated data, which is known only at 30 tail motion phase values while the PUF code requires a much higher time resolution. The initial solution was to assemble a string of periodic velocity fields which would slide along in time to give the propeller inflow at all times. However, this method is unattractive because the wake behind the stator, while periodic in t, is not periodic in x. This is because vortices roll up as opposed to simply translating when they convect downstream. Instead, the proper orthogonal decomposition, POD, method known as the "method of snapshots" was used to describe the wake as a function of tail phase [31]. In this method the time varying velocity field is decomposed into a series of velocity modes and modal coefficients. The velocity field can then be reconstructed as a weighted summation of the velocity modes. If the number of modes is limited to N_{mode}, then the N_{mode} most important modes are kept which best preserve the time varying velocity field. The vorticity of the first four POD modes in the simulated wake for $f = 912$ rpm, $A = 10$ degrees, and $U = 1$ m/s are shown in Figure 5-26.

These 4 modes contain 95% of energy in the velocity field of the simulated wake, however more modes are needed to capture the smaller fluctuations in experimental data. 20 modes are used in all PUF simulations in this work, which contains at least 97% of the energy in all cases. The coefficients used to determine the value of each of

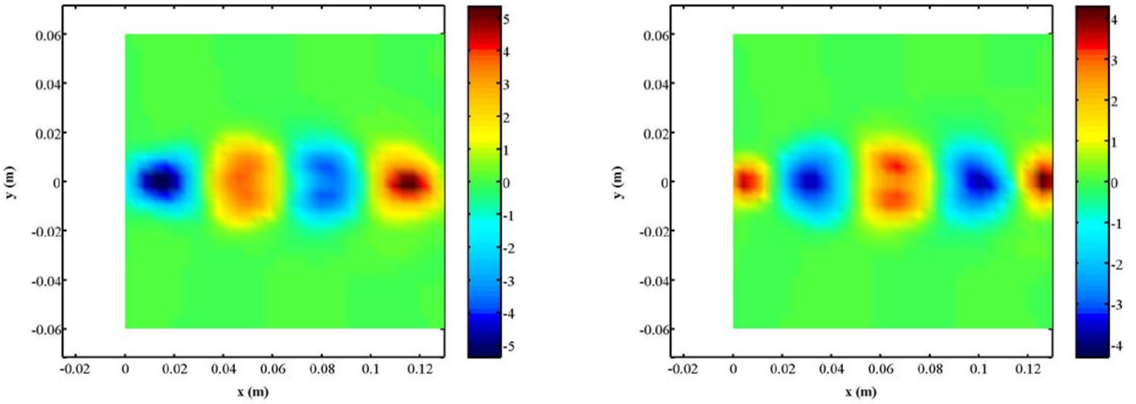

Mode 1 Mode 2

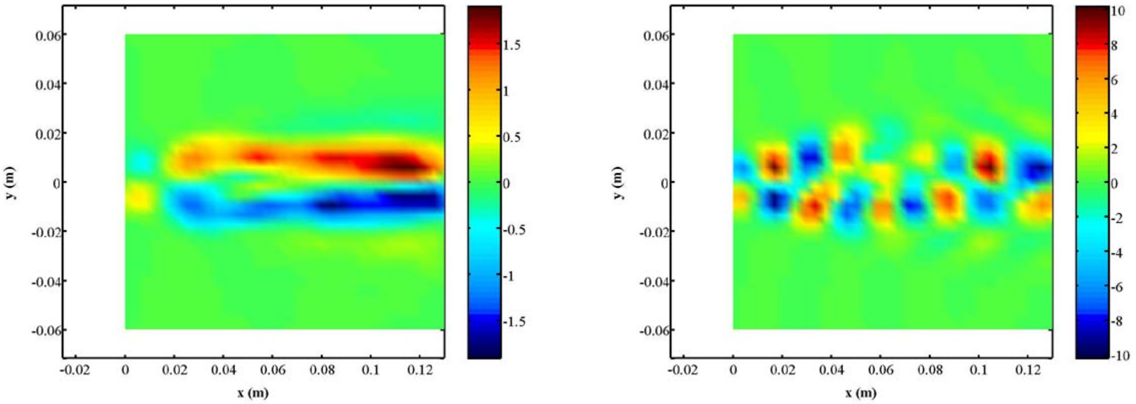

Mode 3 Mode 4

Figure 5-26: Vorticity (1/s) for POD modes of SIM data at $f = 912$ (rpm), $A = 10$ (deg), $U = 1$ (m/s), $St = 0.136$

the first four modes present at each phase in the tail motion are shown in Figure 5-27. In the PUF simulation these modal coefficients are linearly interpolated to find the wake velocity at any tail phase. Notice that the first two modes vary sinusoidally with the tail motion phase. This signifies that these two most important modes account for the convection of the main vortices. Notice also that the vorticity pattern in Mode 3, the almost steady state mode, is indicative of a thrust producing wake.

5.5.2 PUF Simulations with Baseline Wake

The PUF code is used to simulate unsteady blade forces and pressures due to the baseline blade wake deficit interaction. The far field acoustic noise, P', is computed from the PUF output by a separate program in the method of Goldstein [9]. P' is

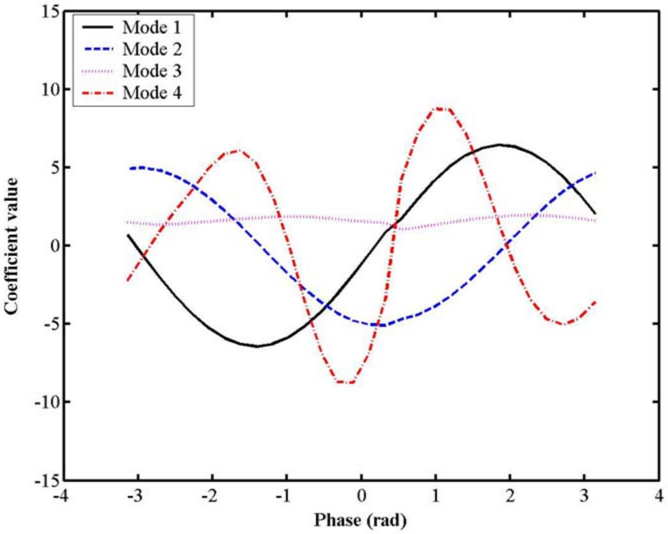

Figure 5-27: POD coefficients for SIM data at $f = 912$ (rpm), $A = 10$ (deg), $U = 1$ (m/s), $St = 0.136$

computed at the coordinates $x = 0.7833$ (m), $y = 0.7071$ (m) which is 1 meter away from the propeller blade plane. The unsteady pressure signature due to the blade passing through the baseline wake velocity deficit from PIV and SIM data is shown in 5-28. These pressure signatures are very similar except that the magnitude of unsteady pressure is slightly higher in the case simulated with PIV data.

5.5.3 PUF Simulations with Unsteady Wake

With good agreement between the pressure signature for simulations with PIV and SIM data for the baseline wake blade interaction, the PUF simulation is now repeated using unsteady wakes due to active tail articulation. Figure 5-24 implies that noise reduction may be dependant on phase and A, with $A = 2$ degrees possibly being the optimal case. Therefore, PUF simulations are performed on SIM data with $A = 2$ degrees. PIV and SIM data with $A = 10$ degrees are also investigated in order to compare how well PUF simulations using SIM data agree with those using PIV data. Phase of the propeller blade relative to the tail tip is varied from 0 to 2π by increments

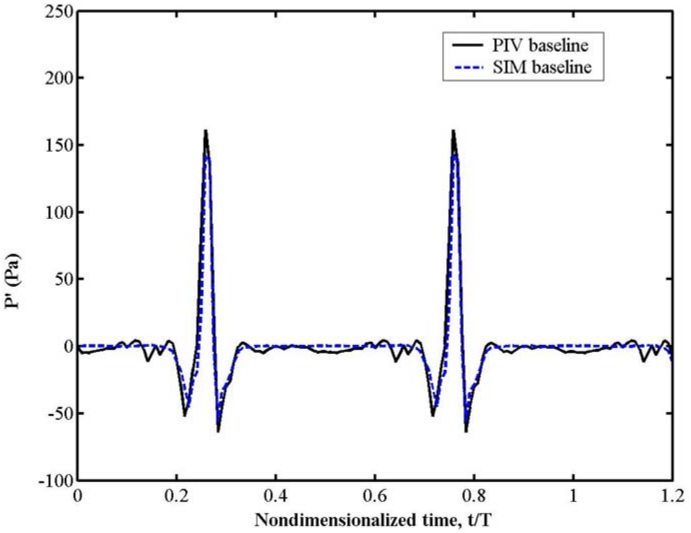

Figure 5-28: P' (Pa) computed by PUF for baseline wake at $U = 1$ (m/s), $T = 0.1316$ (s)

of $\frac{2\pi}{10}$. Comparisons of selected simulations are given in Figures 5-29 through 5-31. For clarity P' from the baseline wake deficit interaction using SIM data is plotted only against P' from the unsteady case using SIM data with $A = 2$ degrees.

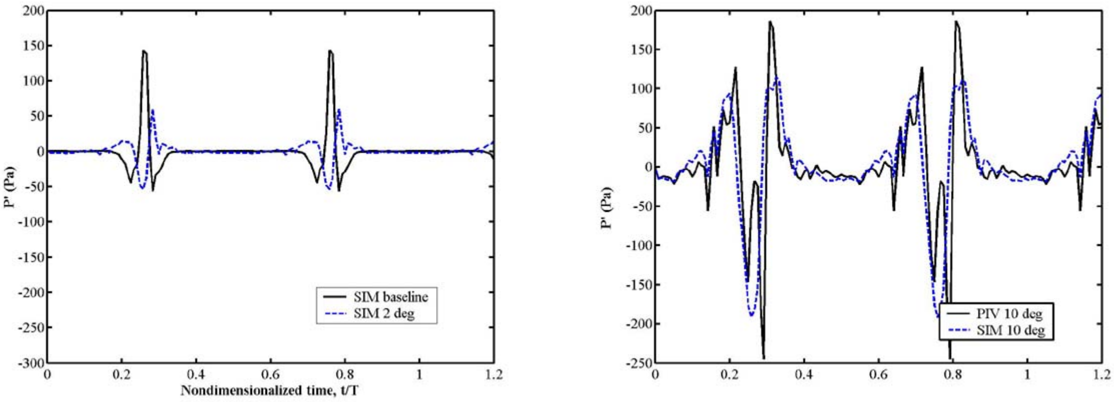

A = 2 deg

A = 10 deg

Figure 5-29: P' (Pa) computed by PUF for $f = 912$ (rpm), $U = 1$ (m/s), phase $= 0.0\ \pi$, $T = 0.1316$ (s)

The pressure signature computed with PIV inflow data is considerably more rough that from SIM data due to variations in the experimental wake from turbulence as well as experimental error. However, P' computed using SIM data agrees reasonably

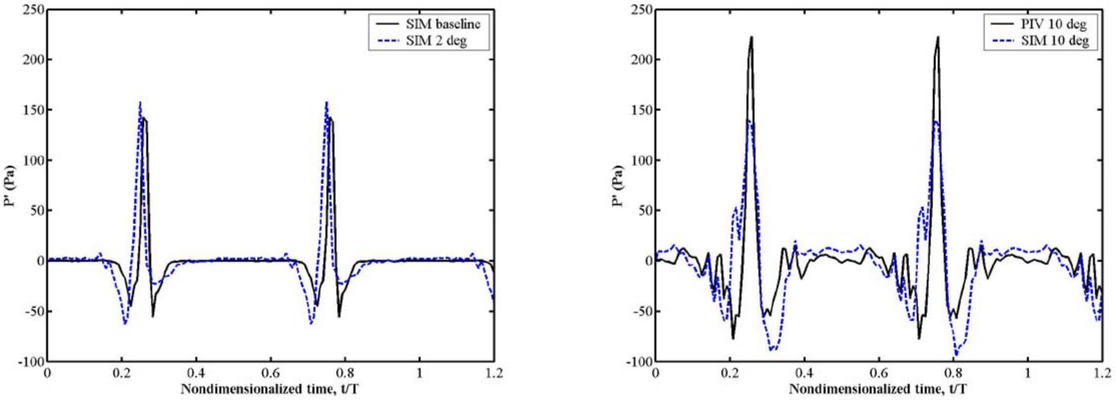

A = 2 deg A = 10 deg

Figure 5-30: P' (Pa) computed by PUF for f = 912 (rpm), U = 1 (m/s), phase = 1.0 π, T = 0.1316 (s)

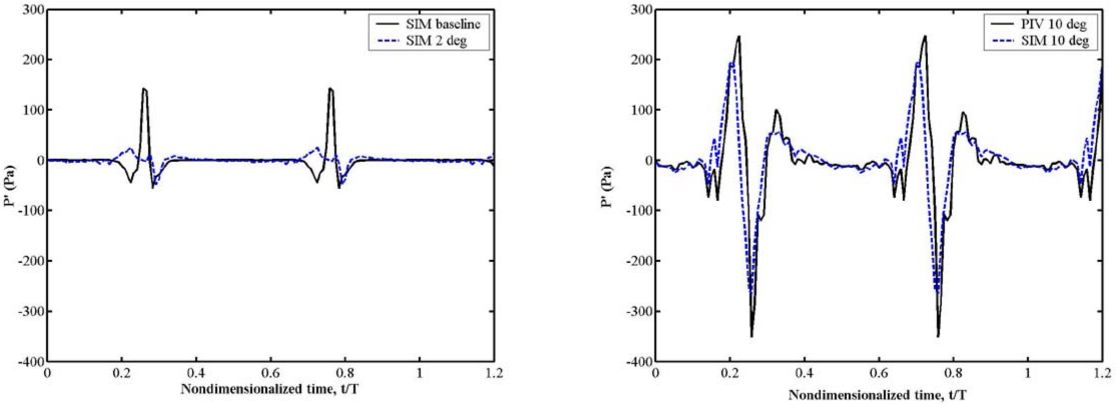

A = 2 deg A = 10 deg

Figure 5-31: P' (Pa) computed by PUF for f = 912 (rpm), U = 1 (m/s), phase = 1.8 π, T = 0.1316 (s)

well with that computed with PIV data in the $A = 10$ degree PUF simulations. This establishes reasonable confidence that PUF simulations using SIM data do agree with PUF simulations using experimental PIV data. Comparing PUF simulations at $A =$ 2 degrees it is seen that at certain phase values the magnitude of the P' is similar to the $A = 10$ degree case while at other tail phases it is significantly lower. In fact for phases 0.0 π and 1.8 π, P' radiated from the blade interaction with the active wake is less than that radiated by the baseline interaction. This result is summed up in Figure 5-32, which shows the peak to peak P' and effective sound pressure level, ESPL, for each of the cases simulated. ESPL is a decibel sound rating calculated as:

$$ESPL = 20\log_{10}\left(\frac{P'_{rms}}{P_{ref}}\right) \tag{5.7}$$

with $P_{ref} = 20\ \mu Pa$. It is noted that the phase of the noise magnitude predicted by PUF simulations using PIV data lags that from simulations using SIM data by about $\frac{2\pi}{10}$. This is most likely related to the lag noticed between PIV and SIM data in general.

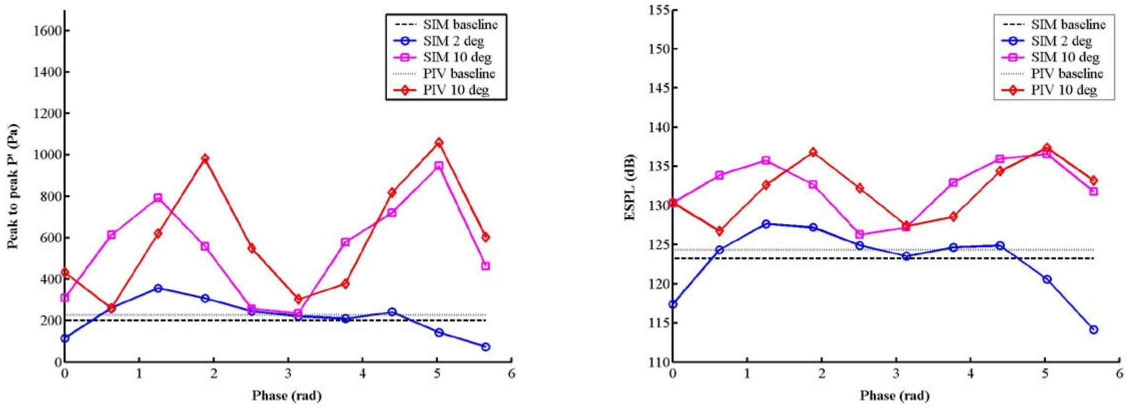

Peak to peak P' (Pa) ESPL (dB)

Figure 5-32: Study of peak to peak P' (Pa) and ESPL (dB) as predicted by PUF with PIV and SIM data for varying A (deg) and phase (rad)

5.5.4 Tonal Noise Reduction

The results shown in Figure 5-32 are promising for two reasons. First, they agree fairly well with the results in Figure 5-24. The low order force simulations suggested that smaller amplitude tail motions would be best for noise reduction, this was confirmed in the PUF simulations. The phase of the optimal tail motion computed by PUF in Figure 5-32 is slightly different than by the low order force simulation shown in Figure 5-24. However, this could be due to three dimensional or unsteady effects which are not captured in the two dimensional simulations. The second reason results in Figure 5-32 are promising is that they show tail articulation is capable of reducing the effective sound pressure radiated in the wake blade interaction. This means that tail articulation is also capable of reducing the tonal noise radiated because the total power in the time domain is related to the total power in the frequency domain by Parseval's theorem. However, it is unknown exactly how the frequency power spectrum will be affected. The noise spectrum of the baseline interaction is plotted in Figure 5-33 for PUF simulations using both PIV and SIM data. In these plots frequency is nondimensionalized by the blade passing rate which is two times the blade rate, in this case 912 rpm. Spectral power is also plotted in the decibel unit by:

$$Power_{dB} = 20 \log_{10} \left(\frac{Power}{Power_{ref}} \right)$$

with $Power_{ref} = 1$ W. It is seen that the noise spectrum for PUF simulations using PIV data and SIM data are very similar, except at the first blade harmonic where the SIM tonal power is 14 dB lower than the power at the first harmonic for PIV data. It is noted that the magnitude of P' in the baseline wake deficit interaction is higher for the simulation using PIV data than that using SIM data. This difference means that tonal power using the PIV data should be higher at some frequencies than tonal power computed using SIM data. However, the reason that this power is the most significantly different at the first tonal of the blade passing rate is not immediately clear either in Figure 5-28 or for physical reasons. It is worth noting that the noise floor in Figure 5-28 is -40 dB. Therefore the difference between 0 and 14 dB, while significant, is not as large as it initially appears to be.

In order to quantify the effect of tail articulation on the reduction of tonal noise, the change in power at each blade harmonic from the baseline noise spectrum due to tail articulation for the cases shown in Figures 5-29 through 5-31 is plotted in Figures 5-34 through 5-36. Because of the differences in spectra between PUF simulations using PIV and SIM data, the change in spectral power plotted is with the reference to the PIV baseline tonal spectrum for PIV simulations and the SIM baseline tonal spectrum for SIM simulations.

Even though the overall noise level is increased reductions in tonal noise at higher harmonics in Figures 5-34 and 5-35 may be significant if alteration of the tonal noise

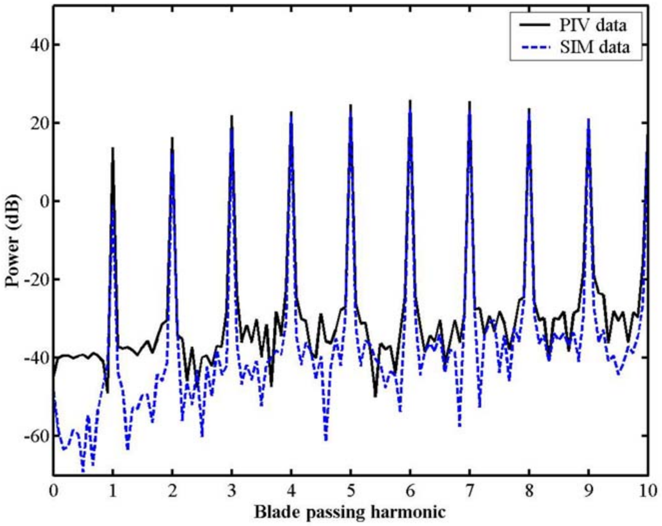

Figure 5-33: Spectral power (dB) of noise radiated by baseline wake blade interaction at $f = 912$ (rpm), $U = 1$ (m/s)

is a primary mission requirement. For the case $A = 2$ degrees and phase $= 0.0\ \pi$ tonal noise reduction is shown across all frequencies except for the first harmonic which is in question. This case shows that reductions of approximately 5 dB may be possible across all frequencies. For the case $A = 2$ degrees and phase $= 1.8\ \pi$ tonal noise is not reduced at lower blade harmonics but is reduced as much as 17 dB at higher harmonics. Note that these results should be treated with caution until the difference in tonal power noted in Figure 5-28 is adequately explained. These levels of noise radiation reduction are significant and the results are even more promising when it is noted that the $A = 2$ degree motion was found to be the optimal tail motion out of a very limited parametric search. It is expected that tail motions found in a more complete optimization process may be capable of much higher levels of noise reduction.

5.5.5 Estimate of Stator Induced Tonal Noise

In the excitement about reduction of tonal noise by tail articulation, the additional tonal noise produced by tail articulation cannot be disregarded. This additional noise is due to the unsteady forces on the active stator by Equation 1.1. If the tail motion

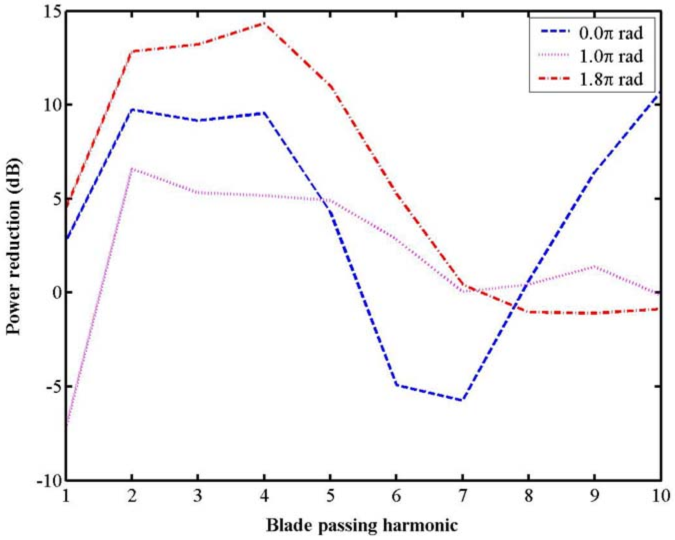

Figure 5-34: Spectral power reduction (dB) in PIV data at $f = 912$ (rpm), $A = 10$ (deg), $U = 1$ (m/s) for varying phase (rad)

is periodic with f then these forces will result in additional radiated tonal noise. To compare the estimated level of additional noise produced with the level of noise reduced, Γ about the stator is found by integrating the negative of the shed vorticity in time. Equation 5.4 is then used to estimate L/S and $\dot{L}/S$ on the active stator, Figure 5-37. It is seen that peak to peak L/S due to tail articulation is about of the same order of magnitude as that due to the blade wake interaction. However, radiated noise is proportional to $\dot{L}/S$, which is significantly lower on the stator due to the longer time scale of unsteady force. It is also noted that as A is reduced the magnitude of both peak to peak L/S and $\dot{L}/S$ are reduced. Because initial simulations have shown that lower A is desired for noise reduction to begin with, self noise radiated by tail articulation is likely to be minimal compared to noise reduction achieved in many cases.

5.5.6 Blade Forces for Future Experiment

Unsteady blade forces predicted by the PUF simulations are included to aid the design of the force instrumented propeller for future experiments studying tail articulation for noise reduction. These forces may be converted to absolute force units by multiplying

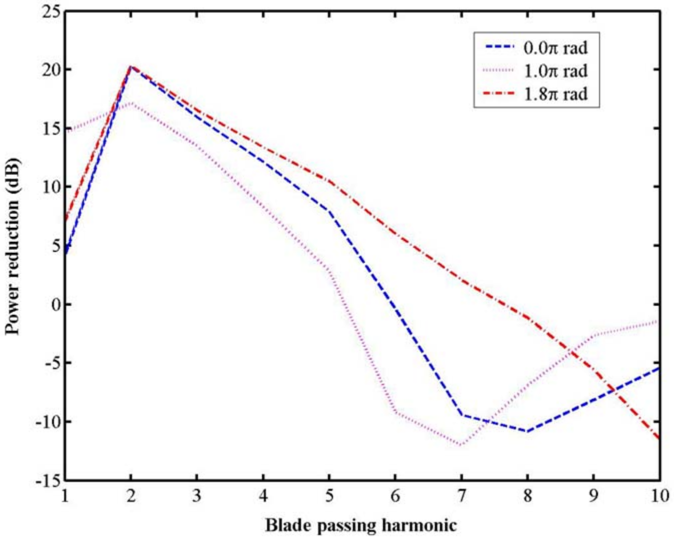

Figure 5-35: Spectral power reduction (dB) in SIM data at $f = 912$ (rpm), $A = 10$ (deg), $U = 1$ (m/s) for varying phase (rad)

by r_{blade}, which is approximately 0.0762 meters. In Figure 5-38 it is seen that a peak to peak force of approximately 2.6 Newtons occurring in a time of 0.01 seconds is expected in the baseline wake blade interaction with $f = 912$ rpm. Also presented in Figure 5-38 the minimum peak to peak force predicted by PUF for $f = 912$ rpm, $A = 2$ degrees, $U = 1$ m/s, and phase $= 1.8\ \pi$ rad is approximately 1.1 Newtons occurring in time of about 0.02 seconds. Not shown in Figure 5-38, the maximum peak to peak force of 6.0 Newtons occurring in a time of 0.01 seconds is expected in the highest force case simulated by PUF for $f = 912$ rpm, $A = 10$ degrees, $U =$ 1 m/s, and phase $= 0.8\ \pi$ rad. These calculations give an order of magnitude for the design of force and torque sensors to be used in the force instrumented propeller experiment. The sensors should be able to measure at least one order of magnitude above and below these values and the response time should be significantly faster than the time noted for changes in peak to peak force. It is seen that the forces computed by PUF are of the same order of magnitude as those computed by the two dimensional blade simulation. However, a dip in force after the blade passes through the wake is seen in PUF simulations but not in the two dimensional simulation. This indicates that unsteady effects not accounted for in the two dimensional blade force

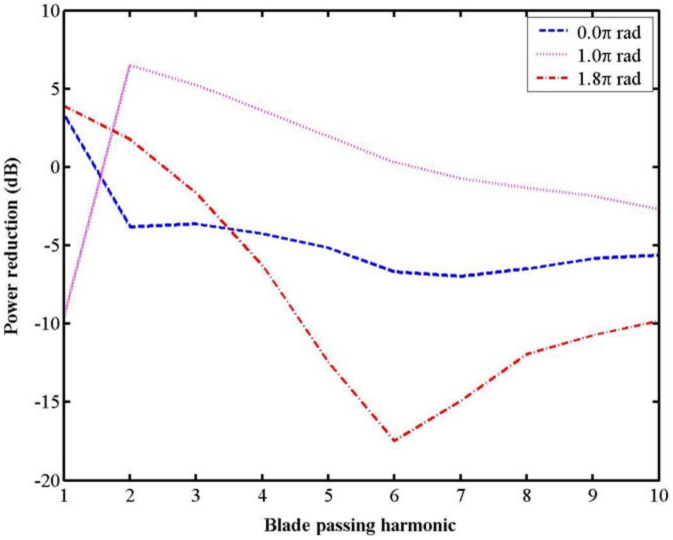

Figure 5-36: Spectral power reduction (dB) in SIM data at $f = 912$ (rpm), $A = 2$ (deg), $U = 1$ (m/s) for varying phase (rad)

model are significant.

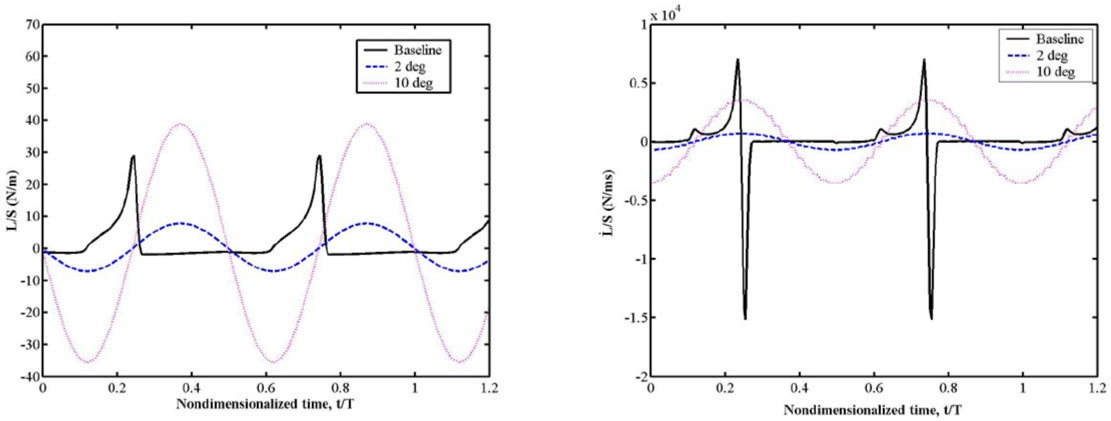

L/S $\dot{L}/S$

Figure 5-37: L/S and $\dot{L}/S$ for the baseline blade wake interaction and active stator for $f = 912$ (rpm), $U = 1$ (m/s) for varying A (deg), $T = 0.1316$ (s)

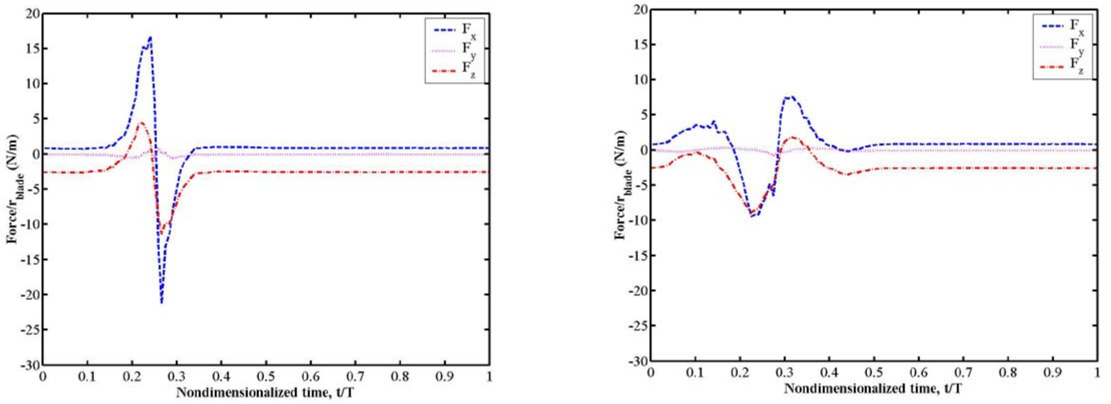

Baseline interaction $A = 2$ (deg) and phase $= 1.8\pi$ (rad)

Figure 5-38: Unsteady forces acting a single propeller blade at $f = 912$ (rpm), $U = 1$ (m/s) for varying A (deg), $T = 0.1316$ (s)

Chapter 6

Conclusion

6.1 Conclusion

The work presented in this thesis has shown a potential for the use of tail articulation in reduction of noise due to the wake deficit blade interaction. It was unknown if previous results showing wake reduction by tail articulation would apply at the higher speeds that AUV vehicles operate at. This work has confirmed the ability of tail articulation to effectively reduce the wake deficit at high Re, $75{,}000 < Re < 300{,}000$. Time mean wake velocity measurements by LDV in Chapter 3 quantify this effect with a relationship between increasing St and a decrease in C_d, Figure 3-12.

Instantaneous velocity measurements by PIV in Chapter 4 allowed for visualization of the wake due to active tail articulation. These measurements helped to shed light on the mechanisms of wake reduction by tail articulation. It was seen that roll up of an alternating vortex sheet shed by the stator is a primary descriptor of the active wake. At low St the vortex wake was seen to move in a quasi-steady manner. At moderate St the vortex sheet was found to begin to roll up. At high St the vortex sheet roll up was seen to occur quickly resulting in a strong vortex wake. Nonsinusoidal tail motions were investigated and it was found that the position of the vortex sheet shed by tail articulation is a nonlinear function of the specific tail motion. Two parametric definitions of tail motion are presented in Section 3.6.2 which may prove useful in future investigation of tail articulation for noise reduction.

A low order model of the wake due to tail articulation was constructed in Section 5.1 which was able to replicate the vortex sheet roll up observed in Chapter 4 for both sinusoidal and nonsinusoidal move profiles. This model was also able to capture the baseline wake deficit measured in Chapter 3. A simple two dimensional blade interaction was simulated in Section 5.4 using the vortex wake generated by the reduced order model of tail articulation. This simulation allowed for quick estimates of the noise reduction possible with a specific tail motion. A small parametric study of sinusoidal tail motions at $f = 912$ rpm and $U = 1$ m/s found $A = 2$ degrees to be optimal.

A three dimensional propeller unsteady force simulation was carried out using propeller inflow data from PIV experiments as well as velocity data generated by the reduced order model of tail articulation. This simulation used a "frozen-wake" approximation, which is assumed to be valid because the investigation was limited to non-lifting propeller blades. Results from PUF simulations showed that reduction in the effective sound pressure level of radiated noise of up to 5 dB is possible using tail articulation. Estimates of the self induced noise due to tail articulation showed that the additional noise radiated will most likely be less than the achieved noise reduction. Furthermore, the optimal tail motion found by the preliminary tail motion optimization by low order force simulations was found to be optimal for reduction of noise.

An interesting point was made about the sinusoidal tail motion with $f = 912$ rpm, $U = 1$ m/s, and $A = 2$ degrees which was found to best reduce noise radiated in the wake blade interaction. While it is unknown if the C_d to St relationship in Figure 3-12 will hold at $A = 2$ degrees, the current plot shows this case will be a maximum drag wake. This result is interesting in that it runs counter to the original conceptions about tail articulation. It was thought that tail articulation would reduce unsteady blade forces by eliminating the wake deficit behind the stator, which would correspond to $C_d = 0$. However, this result implies that the optimal tail motion for noise reduction incurs the highest effective stator drag. Therefore, reduction in radiated noise may come at the cost of extra drag induced on the vehicle. It is unknown if the relationship between this extra drag penalty and the reduction of noise is meaningful in some way or if it is simply a coincidence in the specific case tested.

6.2 Recommendations for Future Work

While the present work has made several successful advancements towards using tail articulation for noise reduction, several improvements should be made in continuing work.

- The next case to be experimentally investigated should be the sinusoidal motion with $f = 912$ rpm, $U = 1$ m/s, and $A = 2$ degrees. LDV measurements should be taken in order to investigate the relationship between St and C_d at $A = 2$ degrees to determine whether the relationship in Figure 3-12 remains valid. This investigation will require the input link in crank rocker mechanism to be reworked or possibly rebuilt in order to provide 2 degree flapping. For $A = 2$ degrees the input link length is $d = 0.1$". A five fold increase in frequency will be required to test the same values of St with $A = 2$ degrees as were tested with $A = 10$ degrees. Therefore, any improvements which can be made to the crank rocker mechanism to allow for higher frequencies are advised. PIV measurements of the wake for this case are also recommended. These measurements should be used to check the validity of the reduced order tail articulation simulation for small A. PUF simulations with the simulated data show reduction in noise but the simulated wake must be compared to experiment before these results can be trusted.

- The apparent phase lag noticed between the tail motion and active wake when measured by PIV should be investigated. It is unknown if this lag is due to systemic experimental error due to timing in the PIV capture software, PIV post processing software or to physical phenomena related to viscous forces. This effect should be resolved so the reduced order model of tail articulation can be improved upon. To do this PIV data should be collected to rule out errors in the PIV apparatus, possibly by including portions of the tail in the PIV image region. Also, it is noted that the interval between PIV frames at $U = 1$ m/s should be increased to give larger particle displacements. A time interval in the range 400 μs<dt<800 μs is recommended by this author.

- Phase between propeller blade and tail motion is currently defined at the tail tip. This phase would be better defined at the blade passing plane. This definition would allow more consistent comparisons of blade passings at different frequencies. The investigator would then be better able to decide if there is any optimal phase for the blade wake interaction throughout all blade rates.

- As noted in Section 5.1 boundary layer effects and increased shed vortex strength due to tail displacement are not accounted for in the current model of tail articulation. These effects are significant in steady state deflections of the tail and their behavior is unknown for active tail displacement. Once the PIV system phase lag problem has been identified, PIV data should be used to generate a simple dynamic model of how boundary layer vortex shedding changes with tail motion. This model will likely be applicable to tail articulation on the cambered stators used in SISUP propulsion, which are effectively the same as a stator with static tail deflection. Numerical implementation of core spreading, the time scale of vorticity diffusion into the stator wake, and turbulent diffusion should also be considered in the low order model of tail articulation.

- The low order model of transient tail motions, such as start up and nonperiodic tail motions, should be compared to PIV measurement of the same transient motions. Acquiring transient PIV data with the equipment at NUWC will be considerably more difficult than acquiring steady state data. However, this step will be necessary if tail motion is to be completely defined in real time by a final control system or if optimization is to consider nonperiodic tail motions.

- Unsteady velocity and pressure effects should be incorporated into the two dimensional blade force model in Section 5.4. Significant unsteady force and pressure effects were seen in PUF simulations but were not captured by the current two dimensional panel method. While the current model was able to predict the tail motion which PUF found to optimally reduce radiated noise, unsteady effects will become more important as optimization proceeds with higher resolution.

- Propeller simulations with the three dimensional unsteady PUF code provide close approximations of blade forces and noise radiated in the vortex blade interactions. However, the ”frozen-wake” assumption limits these tests to non-lifting propeller designs. A test with a real non-lifting force instrumented propeller in the wake of the active stator will verify the PUF results and show real noise reduction by tail articulation. This test setup will also be used to verify that tail motions found by the optimization process do result in lower unsteady blade forces. This equipment should be designed to accommodate lifting propeller blades, which will show the potential for noise reduction by tail articulation in real vehicles with higher three dimensional effects. Furthermore, data from experimental tests with lifting propellers will help to determine the wake regimes for which the ’frozen-wake’ assumption remains valid.

- Once optimal tail motions have been identified and verified experimentally, a preliminary control system should be designed which is capable of maintaining the optimal wake blade interaction under small disturbances, such as changing freestream velocity.

Appendix A

Software Reference

A.1 Matlab Routines

A.1.1 Dual Vortex Simulation Routines

[tailv, taild0] = makesin(N, f, A, phase)

[tailv, taild0] = makesinpow(N, f, A, n, phase)

[tailv, taild0] = maketransient(N, f, A, ratio, theta, phase): These functions define the periodic tail motion as a series of velocity impulses, which correspond to discrete steps in the tail displacement. N is the number of discrete tail positions per period, f is the base frequency of the motion in Hz, A is the maximum tail displacement, phase is the phase of tail tip. Tailv is the Nx1 vector of velocity impulses and taild0 is the initial tail position which are used to in the low order tail articulation model in **dualvortexwake** and **MakeSimPUF**.

[time, Cl, lift] = dualvortexwake(f, tailv, taild0): This function generates the wake behind the active stator with the dual vortex shedding method. After a certain number of flapping periods the wake is assumed to be well developed and the blade vortex interaction is simulated. The function inputs are; f the base flapping frequency, tailv is the vector defining the impulse velocity at N points in the flapping period, taild0 the initial tail displacement. Note, if the sum of tailv is not zero the tail's mean position will drift from period to period. The function outputs are; time is the simulation time in seconds, Cl is the coefficient of lift for the blade at each time, lift is the blade lift per span at each time. Several important constants are set within the function including; U the freestream velocity, Nres the number of time steps between each vortex pair shedding, damped is a switch which damps the start up tail motion for damped_periods to allow the wake to converge to steady state more smoothly.

MakeSimPUF(f, tailv, taild0, bins): This function uses the dual vortex shedding method to simulate the wake behind the active stator similarly to **dualvortexwake**. After the wake has converged to steady state the u and v velocities are measured at grid points and saved in the same fashion as experimental PIV data. This data can then be used by **MakeUnsteadyPIVPUF** to generate inflow files for the PUF program.

[node_x, node_y, xmid, ymid, dx, dy, l, costheta, sintheta, tangent, normal, A, C] = makenaca4(NACA, N, b, Chord, sig2, flapC, flapA): This function defines a NACA four digit airfoil to be used by the panel code. NACA is a 1x3 vector of the NACA four digit number (ie: [0 0 12]), N is the number of panels, b is the blade pitch angle in rad, Chord is the chordlength in meters, sig2 is the smoothing kernel length, flapC is the nondimensionalized length where a trailing edge flap is hinged (ie: 2/3), flapA is the flap deflection if any in rad. Node_x and node_y are the x and y coordinates of the N+1 panel nodes, xmid and ymid are the x and y coordinates of the N panel midpoints, l is the length of each of the N panels in meters, costheta and sintheta are the orientation of each panel in rad, tangent and normal are the unit tangent and normal vectors for each panel, A and C are panel source and vortex incidence matrices.

[strengths, Cp, Cl, Cd] = solve_lift(N, A, LL, UU, C, node_x, node_y, xmid, ymid, dx, dy, costheta, sintheta, Uinf, u, v, b, Chord): This function uses the airfoil parameters defined by **makenaca4** to solve for the flow around the airfoil. The parameters are the same as in **makenaca4**, LL and UU are the LU decomposition of the A matrix. Strengths is an N+1x1 vector, the first N entries are the N panel source strengths and the final entry is the airfoil vortex strength. Cp is an Nx1 vector with the coefficient of pressure evaluated at each panel midpoint, Cl and Cd are the airfoil coefficient of lift and drag respectively.

A.1.2 LDV Data Processing Routines

LDVplot(RPMS, DEGS, TUNNELS, SORTBY): This function is used to plot a selection of all of the LDV data in a directory on the same plot. The data must be named as the *rpm*deg*tunnel.txt file (sorry it doesn't work for all file names). The program will find all files which match any combination of the values of RPMS, DEGS and TUNNELS. For example to plot all data at any rpm, 10 degrees, either 75 or 150 tunnel speed, and sort the data into series by tunnel speed you would call this function as: LDVplot([], 10, [75, 150], 'tunnels').

CDplot(RPMS, DEGS, TUNNELS, OuterRegion): This function is similar to **LDVplot** but rather than plot wake profiles it is used to plot the relationship between C_d and St. To plot the C_d versus St for all data in a directory call this function as: CDplot([], [], []).

CompareToPiv(basename): This function is used to compare the normalized wake for the same case as measured by PIV and LDV. The function compares LDV data stored in the filename given by basename to data PIV data stored in a file named 'PIVtoLDV.mat'. This file is created by the function **MakePIVtoLDV**.

A.1.3 MatPIV Processing Routines

Definewoco(filename,typ): This function is used to examine the calibration image and create a pixel to world map. Filename is the name of the calibration photo and typ is the marking used on the calibration plate. The function correlated the calibration picture with an image of a cross to find the location of the crosses in pixel coordinates. There are two working methods available, linear or polar. Linear performs a least square fit between the pixel coordinates and defined world coordinates, accounting for both a translation and rotation of the pixel frame. The polar method transforms both coordinate systems into a polar frame, which is not necessarily centered on the pixel frame center in an attempt to account for nonlinear effects such as index of refraction. The polar calibration is used in this thesis. Call as Definewoco('cal.tif','+').

Mask(ima,wocofile,x,y,u,v): This function allows the user to block out a region of the pixel frame from processing. Ima is the name of the photo to lead for reference when defining the region, wocofile is the world coordinate matrix created by Definewoco. This might be a good idea for example to block out solid areas when investigating flow around a solid body. The mask saves processing time and improves accuracy, because the zero velocity computed in the solid affects neighboring windows during filtering. If no mask is desired simply click outside the view area. This function creates the file 'polymask.mat'. Call as Mask('cal.tif','worldco1.mat').

[du,dv,stream]=streamfilt(x,y,u,v,factor,maske): This filter finds a stream function which describes the level curves of vorticity in PIV data. This stream function can either be found with fixed, zero-slope, or periodic boundary functions. Once the stream function is found it is differentiated to give a divergence approximation of the actual flowfield.

A.1.4 PIV Data Processing Routines

CheckData(basename, movetype, rpm, max_encoder, min_encoder, silent): Each series of PIV images captured during PIV measurements is given a separate basename which starts at 'a' then continues in increasing order through to 'aa', 'ab' and beyond. A PIV synchronizer timing record 'a000.tim' and a NI motion control timing record 'a.txt' are created in each data run. **Checkdata** reconciles these data records so that the tail position is determined at each image capture time. It should be noted that if **Checkdata** detects a blip in the PIV timing file indicative of a bad PIV pair it will delete the bad image pair and all subsequent image pairs with the same basename. Basename is the basename of the current measurement, movetype is the type of motion investigated ('baseline', 'sin', 'transient'), rpm is the motion frequency in rpm, max_encoder and min_encoder are the maximum and minimum tail positions in encoder counts, silent determines whether or not to suppress printing messages during processing. This function writes out a file for each basename processed, 'adata.mat', as well as adds the timing information to a global file for all measurements in the directory, 'AllPhases.mat'.

MakeAllPhase(movetype, rpm, max_encoder, min_encoder, silent): This function is used to call **Checkdata** for each basename in the current directory. Calling this function is preferred to repeatedly calling **Checkdata** because the user does not have to call **Checkdata** separately for each case and because it eliminates errors in 'AllPhases.mat' due to **Checkdata** being called twice for a given basename.

StatorPIVRunfile(basename): This is the function which determines the operation of the MATPIV processing. When **StatorPIVRunfile** is called for a given basename processes the world coordinate file defined by **Definewoco**, the mask file written by **Mask**, and all of the image pairs with the basename to write out a filtered velocity file which gives the velocity field measured from each image pair.

BatchPIVProcess(): This is the upper most function used in PIV processing. This function will identify all of the available data series in the current directory and then call **StatorPIVRunfile** for each data series.

RunThroughData(bins, showplots, showbins, startfile): Once all of the PIV images in the directory have been processed **RunThroughData** is used to sort the filtered velocity fields written by **StatorPIVRunfile** into bins sorted by phase of the tail motion computed by **CheckData**. All velocity fields in each bin are averaged together. Bins is the number of phase bins to separate data into, showplots is set to 1 to show all individual velocity plots or 0 to not, showbins is set to 1 to show all phase averaged velocity bins or 0 to not, startfile determines at which basename the function starts at (this is 1 unless debugging). The phase average velocities are written to 'Phase_Average_Velocities.mat'.

PhaseMakeMovie(moviefile, movetype, rpm, deg): This function is used to create movies of the active wake behind the stator. The function loads 'Phase_Average_Velocities.mat' and there is one movie frame for each phase bin with the frame being the phase averaged vorticity for the current bin. Moviefile is the name of the movie file to be written, movetype is the type of motion investigated ('baseline', 'sin', 'transient'), rpm is the tail frequency in rpm, and deg is the maximum tail deflection in degrees.

MakeBaseline(tunnelspeed): This function is used to make a 'Baseline.mat' file from 'Phase_Average_Velocities.mat'. Tunnelspeed is the tunnel prop rotation rate in rpm. The baseline file is simply the average of all of the phase averaged data. This file is useful for comparing the wake of an active stator to the baseline wake deficit at the same tunnel speed.

MakePIVtoLDV(tunnelspeed): This function reads in the velocity data from 'Phase_Average_Velocities.mat' and then averages the data from all bins to create a velocity data similar to that which would be measured by LDV. Tunnelspeed is the tunnel prop rotation rate in rpm. The data is written to the file 'PIVtoLDV.mat' which can then be used by **CompareToPiv**.

POD(modes): This function is used to decompose the PIV measured velocity in the series of modes and coefficients by POD. Modes is the number of modes to be computed.

MakeUnsteadyPIVPUF(basename, rpm, deg): This function creates the POD mode files used as input to PUF simulations from the unsteady velocity data in 'Phase_Average_Velocities.mat'. Basename is the basename of the PUF input files ('912rpm10deg75'), rpm is the tail frequency in rpm, and deg is the maximum tail deflection in degrees. Four output files are created which are the POD modes and coefficients for both the u and v components of velocity.

A.2 PUF

puf_uli.exe: The PUF-14 code has been adapted to this project by Stephen Huyer at NUWC. The program simulates the three dimensional, unsteady propeller blade wake interaction as described in Section 5.5. The propeller geometry is defined by the propeller files 'Prop1.avg.dat'-'Prop9.avg.dat' and can be selected in the file 'prop.puf'.

The number of time steps per revolution, NTSR, the number of revolutions simulated, NREV, and advance coefficient, ADVCO, are also set in the file 'prop.puf'. A file called 'FLAP_FOIL.INPUT' is used to set parameters related to the unsteady stator wake. The filenames of the u and v velocity POD modes and coefficients, relative phase between propeller blade and tail motion, and the flapping foil reduced frequency are set in this file.

propnoise.exe: Calculations by PUF give blade forces and pressure, to convert these into far field P' the program **propnoise.exe** is run once the PUF program has terminated. This program uses an input file named 'PropNoise.adm' which defines the absolute value of fluid density, freestream velocity, blade rotation rate, and field coordinate point in order to convert the PUF simulation into real world units.

[Power, Freq, Pressure, Time] = TonalPowerSpectra(filename, NTSR, average, plotfigs): This function is used to read the pressure signature and estimated spectral density of the noise predicted by PUF simulations. This function may be called as TonalPowerSpectra('PropNoise.out', 120, 1, 0)

[BP, FX, FY, FZ, FMag] = ReadBladeForces(filename): This function is similar to **TonalPowerSpectra** except that blade forces predicted by PUF are read. These forces are not in real world units but nondimensionalized as $\frac{F}{U_{blade}^2 r_{blade}^2}$.

PUF Configuration Notes: The following is a list of parameters to be set for various common test cases.

1) Prop1.avg.dat, Flapper 459 rpm, Prop 229.5 rpm or 3.8250 Hz, J or ADVCO = 1.7155, two-bladed prop will interact once per flapping cycle, 1flap-1prop, (U = 1, freduced = 0.5829), (U = 2, freduced = 1.1659), (U = 3, freduced = 1.7488).

2) Prop2.avg.dat, Flapper 459 rpm, Prop 459 rpm or 7.6500 Hz, J or ADVCO = 0.8577, two-bladed prop will interact twice per flapping cycle, 1flap-2prop, (U = 1, freduced = 0.5829), (U = 2, freduced = 1.1659), (U = 3, freduced = 1.7488).

3) Prop3.avg.dat, Flapper 459 rpm, Prop 918 rpm or 15.300 Hz, J or ADVCO = 0.4289, two-bladed prop will interact 4 times per flapping cycle, 1flap-4prop, (U = 1,

freduced = 0.5829), (U = 2, freduced = 1.16590, (U = 3, freduced = 1.7488).

4) Prop4.avg.dat, Flapper 912 rpm, Prop 456 rpm or 7.6000 Hz, J or ADVCO = 0.8634, two-bladed prop will interact once per flapping cycle, 1flap-1prop, (U = 1, freduced = 1.1582), (U = 2, freduced = 2.3165), (U = 3, freduced = 3.4747).

5) Prop5.avg.dat, Flapper 912 rpm, Prop 912 rpm or 15.200 Hz, J or ADVCO = 0.4317, two-bladed prop will interact twice per flapping cycle, 1flap-2prop, (U = 1, freduced = 1.1582), (U = 2, freduced = 2.3165), (U = 3, freduced = 3.4747).

6) Prop6.avg.dat, Flapper 912 rpm, Prop 1824 rpm or 30.400 Hz, J or ADVCO = 0.2158, two-bladed prop will interact 4 times per flapping cycle, 1flap-4prop, (U = 1, freduced = 1.1582), (U = 2, freduced = 2.3165), (U = 3, freduced = 3.4747).

7) Prop7.avg.dat, Flapper 1252 rpm, Prop 626 rpm or 10.433 Hz, J or ADVCO = 0.6289, two-bladed prop will interact once per flapping cycle, 1flap-1prop, (U = 1, freduced = 1.5900), (U = 2, freduced = 3.1801), (U = 3, freduced = 4.7701).

8) Prop8.avg.dat, Flapper 1252 rpm, Prop 1252 rpm or 20.867 Hz, J or ADVCO = 0.3145, two-bladed prop will interact twice per flapping cycle, 1flap-2prop, (U = 1, freduced = 1.5900), (U = 2, freduced = 3.1801), (U = 3, freduced = 4.7701).

9) Prop9.avg.dat, Flapper 1252 rpm, Prop 2504 rpm or 41.733 Hz, J or ADVCO = 0.1572, two-bladed prop will interact 4 times per flapping cycle, 1flap-4prop, (U = 1, freduced = 1.5900), (U = 2, freduced = 3.1801), (U = 3, freduced = 4.7701).

A.3 Labview Modules

Current software version 4.

Trigger_test.vi: This module is useful for initializing the trigger communication between the motion control card and the PIV synchronizer. Often the Labview programs will not correctly trigger the synchronizer to begin PIV measurements until this program is used. Simply toggle the first channel up and down, if this does not start PIV measurements check the trigger connection. Be very careful that the laser is not in operation when this trigger program is used.

clear_buffers.vi: This program should be used to clear the buffers in the motion control card in between runs using buffered control when the motor is directly coupled to the tail shaft. If these buffers are not cleared bad things may happen.

Sine_w_camera_control.vi: This program is the basic program used to control PIV measurements of tail articulation by the crank rocker. The motor velocity and acceleration are set and the output file name, ie. 'a.txt', and base directory are set. When the run button is pressed on the VI the motor will start, when it has come up to speed the "Full Speed" light will activate. At this point the "Run PIV" button may be pressed. This will trigger the synchronizer to begin PIV measurements. After this the larger green indicator at the bottom of the will flash as PIV triggers are received from the synchronizer. When the PIV measurement has ended the "Stop" button is pressed. This will trigger the synchronizer to stop laser pulsing, bring the crank to a stop and write the necessary output data file to the current directory.

Baseline_w_camera_control.vi: This program works much the same as **Sine_w_camera_control** but it does not move the tail. This is useful for PIV measurements of static tail positions.

LDV_Buffered_Control.vi: This program works much the same as **Sine_w_camera_control** but it does not move the tail in the crank rocker configuration. Instead it requires buffered control with the motor directly coupled to the tail shaft. Rather than input a velocity and acceleration the inputs to this function are the number of points per buffered move, N, and the requested time interval between points. When the run button is pressed a dialog box is opened which requests the input file defining the control points in the buffered move.

Buffered_Control.vi: This program moves the tail with buffered control but does not interface the PIV system. This function is useful for LDV measurements that require nonsinusoidal motions.

NI controller gains for crank motions:

KP - 150, KD - 300, KI -120, KV - 0, Td - 3, Ilim - 1000, Vfb - 0, Vff - 0, Aff - 0, Primary DAC - 0, Secondary DAC - -1

NI controller gains for directly coupled motions:

KP - 600, KD - 200, KI - 0, KV - 0, Td - 2, Ilim - 1000, Vfb - 0, Vff - 0, Aff - 0, Primary DAC - 0, Secondary DAC - - 1

AMC Drive Settings:

8192 Counts/index

Velocity Loop: P - 2.0, I - .01, D - .04, Feed Forward - 0, Filter - 150 Hz

Position Loop: P - 150, I - .0001, D - 1.0, Vff - 0, Aff - 0

Current Loop: P - 2.8439, I - .6543

Appendix B

Apparatus Prints

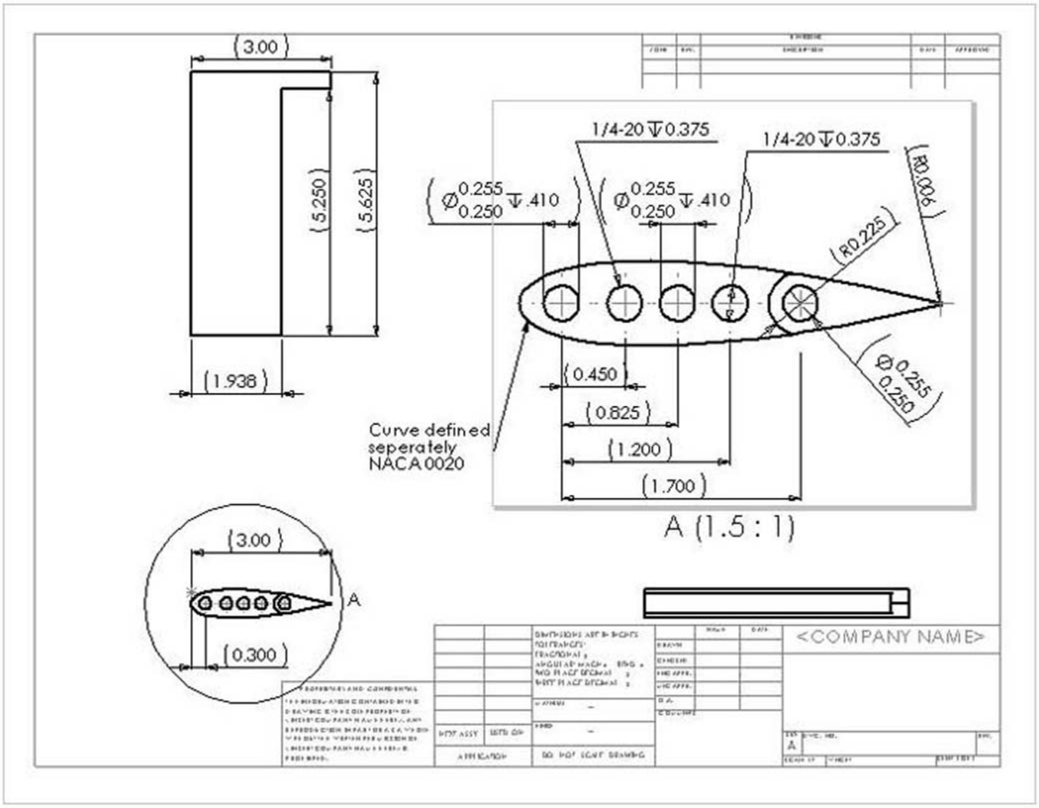

Figure B-1: Airfoil Body Part A

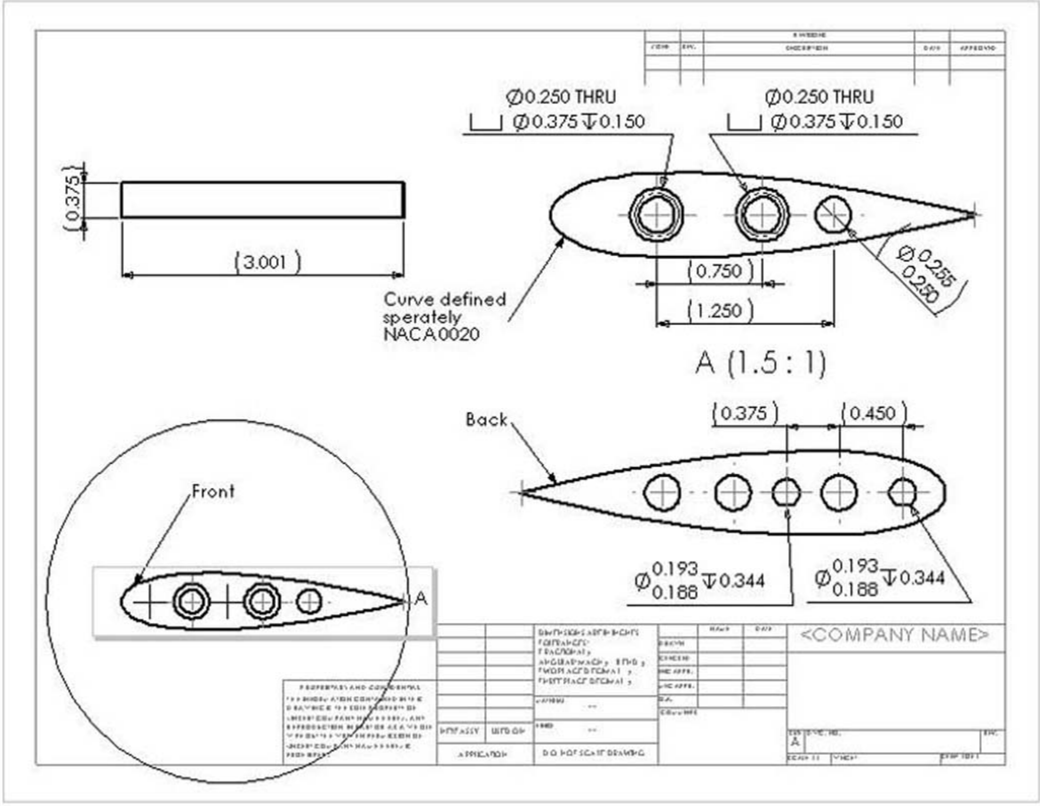

Figure B-2: Airfoil Body Part B

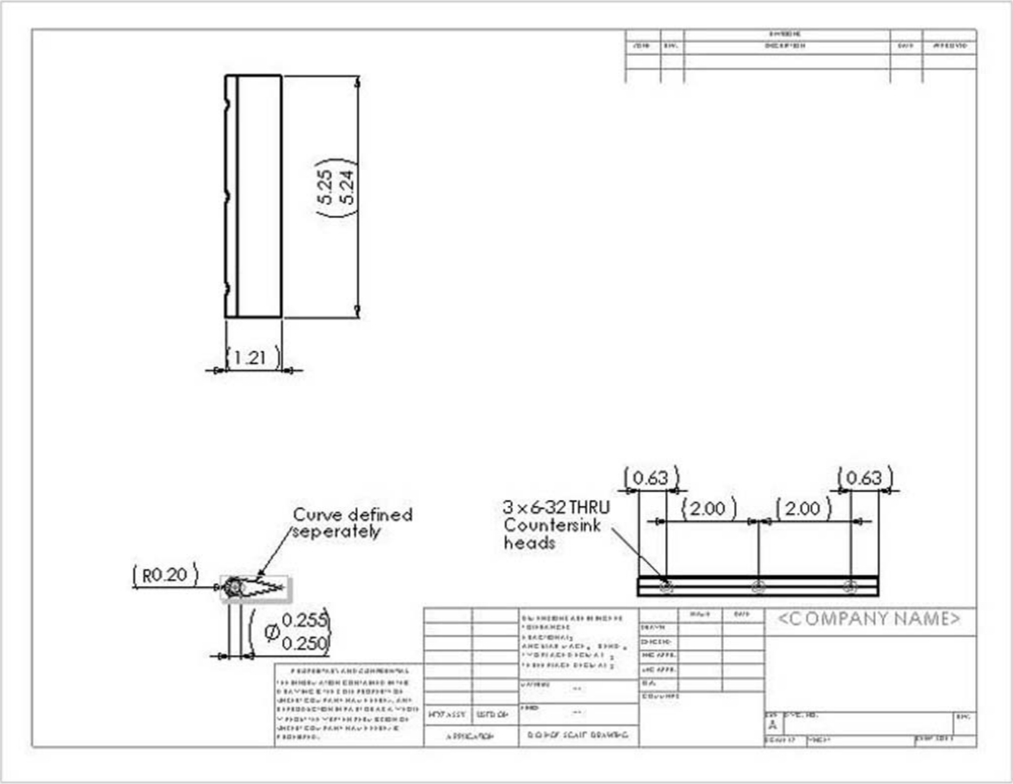

Figure B-3: Flapping Tail

Appendix C

PIV Setup Instructions

The camera generates the timing signal. The synchronizer uses the camera signal to determine when to pulse the lasers so as to frame straddle the camera frames. Before the signals from the synchronizer can be used by the lasers, they must be inverted. The 4 signal generators do this. When set correctly, they invert and delay in a known way, allowing the laser-camera synchronization to occur.

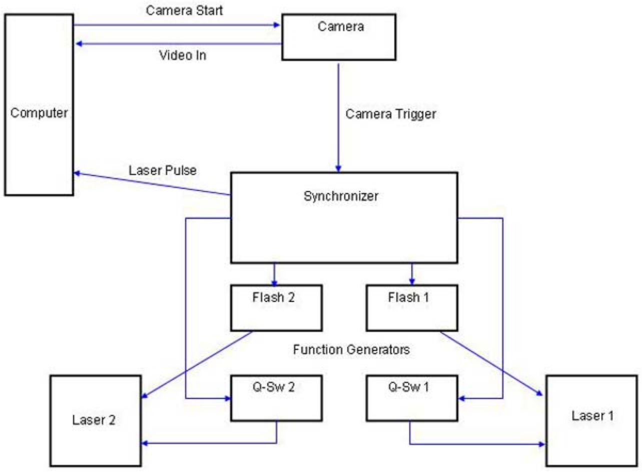

Figure C-1: Schematic of the PIV measurement system

The following settings on the function generators are required:

Flashlamp 1 (HP Programmable Signal Source): Freq = 660Hz, Offset = 1.25V, Amp = 2.5V, Duty = 20%, Function = Square, Input Mode = Trig, Note that this model of function generator is enabled when the Enable/Disable light is OFF.

Q-Switch 1 (HP Programmable Signal Source): Settings same as above.

Flashlamp 2 (Wavetek Sweep Generator Model 185): Freq = 5, Sweep Start, 10ms, x100, symmetry normal, Trig mode, Squarewave w/ no offset, 0 amp variable

Q-Switch 2 (Wavetek Sweep Generator Model 145): Freq = .4, Trig mode, Pulse Delay blank, Pulse width off, Delayed normal, Freq multiplier 1K, Trigger start off, square wave, Attenuation 0.

Laser Pulse Synchronizer (TSI 610030): YAG Rate 10Hz, Internal, Start and Stop delays = 0 seconds, Mode = Video Camera Triggered, # Frames = 0, Q-Switch Divide = 02, Pulse delay = 65.760 ms, YAG pulse = Double Pulse, YAG separation = 0.0002000 sec, Q-Switch 1 = 200 μs, Q-Switch 2 = 200 μs

The following settings relate to the Insight Software, (requires hardware key)

Camera Dialog Box: Sequence Memory = System, Sequence, Locked, Frame Straddle

Timing Tab: Pulse Separation = 200 μs, 0 vector fields, 7.500Hz repetition, 65.76 Pulse delay (auto), 0 ms Camera Trigger, 0 FG Trigger, 0 Image Shift

Components Tab: 630045 PIVCAM 10-15, Other YAG Lasers, Image Shifter None, Synchronizer 610030, Frame Grabber 600066 PCI, No Realtime Arrows

Setup: Pixels 1018 x 1008, Spacing 9 x 9, Crosscorrelation CCD checked, Delay 65.76 ms, Min 0.025 ms, Progressive Scan, Beam 6mm, Flashlamp 10Hz, Min 0.1, Max 100

Operating Mode: Nd:YAG Double Pulse, Video Camera Timing (No external trigger), 2-frame image capture

YAG Power: Q-Switch1 = Q-Switch2 = 200, Preset off

Pulse Energy Selection: Yag1 = Yag2, High = 170, Medium = 125, Low = 100

Other Notes: To turn synchronizer from Running Sequence to Stopped and back give a low pulse on the External Trigger In line on the synchronizer. Press start on the camera dialog first, then turn the synchronizer to Running Sequence, then wait until the insight software is finished before stopping.

Note that the Insight PIV software frames do not always make nice pairs (that is the frame straddling did not work correctly and the second frame in the pair is not 200 μs after the first). When analyzing it will be obvious when this happens (the vectors will go everywhere at crazy amplitudes). However, we found that a perusal of the timing file written with each sequence (*.tim) will show a clue when this happens. The difference between each pair should be around 540 ms. If much different from this (ie 600 or 700 ms) the pair will often be bad. Must be the computer can't keep up with the data collection, or the synchronizer burped. This happens once every 4 or 5 sequences, and we threw out any data in the sequence after the bad pair (because we were synchronizing the timing with an external device with its own clock, and felt we couldn't trust any timing after a bad pair). This problem becomes much worse if the PIV computer is doing anything other than PIV (writing or reading from disc, running other programs).

Bibliography

[1] I.H Abbott, A.E. Doenhoff, and L. Stivers Jr. Summary of airfoil data. Report 824, NACA, 1945.

[2] Jamie M. Anderson. *Vorticity Control for Efficient Propulsion.* Ph.d. thesis, Massachusetts Institute of Technology, 1996.

[3] J.M. Anderson and P.A. Kerrebrock. The vorticity control unmanned undersea vehicle (vcuuv) performance results. *Eleventh International Symposium on Unmanned Untethered Submersible Technology*, pages 360–369, 1999. Lee, New Hampshire.

[4] J.M. Anderson, K. Streitlen, D.S. Barrett, and M.S. Triantafyllou. Oscillating foils of high propulsive efficiency. *J. Fluid Mech.*, 360:41–72, 1998.

[5] B.C. Basu and G.J. Hancock. The unsteady motion of a two-dimensional aerofoil in incompressible inviscid flow. *Journal of Fluid Mechanics*, 87(1):159–178, 1978.

[6] R.E. Caflisch and J.S. Lowengrub. Convergence of the vortex method for vortex sheets. *SIAM J Numerical Analysis*, 26:1060–1080, 1989.

[7] G.H Cottet and P.D. Koumoutsakos. *Vortex Methods: Theory and Practice.* Cambridge University Press, 2000. Section 4.3.7.

[8] Dantec Dynamics, P.O. Box 121, Tonsbakken 18, DK-2740 Skovlunde, Denmark. *BSA Flow Software v 2.1 Installation and User's Guide*, 8th edition, 2003.

[9] M.E. Goldstein. *Aeroacoustics.* McGraw-Hill, New York, 1976.

[10] Triantafyllou G.S., Triantafyllou M.S., and Grosenbaugh M.A. Thrust development in oscillating foils with application to fish propulsion. *Journal of Fluids and Structures*, (7):205–224, 1993.

[11] N.J. Hahn, D.H. Renick, and T.E. Taylor. Puf-14.4: An unsteady analysis code for wake-adapted, multi-stage ducted propulsors. *Massachusetts Institute of Technology Department of Ocean Engineering*, December 2000.

[12] J.L. Hess. Calculation of potential flow about arbitrary 3-d lifting bodies. Technical Report Douglas Report MDC-J5679-01, Douglas Aircraft Company, 1972.

[13] J.L. Hess and A.M.O Smith. Calculation of nonlifting potential flow about arbitrary three-dimensional bodies. Technical Report Douglas Report ES40622, Douglas Aircraft Company, 1962.

[14] S.A. Huyer and S.R. Snarski. Unsteady propulsor force prediction for spatially and temporally varying inflow. *ASME Fluids Engineering Division Summer Meeting*, July 2002.

[15] S.A. Huyer and S.R. Snarski. Analysis of turbulent propeller inflow. *ASME Journal of Fluids Engineering*, May 2003.

[16] K.D. Jones, C.M Dohring, and M.F. Platzer. An experimental and computational investigation of the knoller-betz effect. *AIAA*, 36(7):1240–1246, 1998.

[17] J.E. Kerwin and C.S Lee. Prediction of steady and unsteady marine propeller performance by numerical lifting surface theory. *Society of Naval Architects and Marine Engineers*, 86, 1978.

[18] R. Krasny. A vortex-dipole sheet model for a wake. *Physics of Fluids*, A(1):173–175, 1989.

[19] R. Krasny. Vortex sheet roll-up. *World Scientific*, pages 43–49, 1993. Proceedings of the RIMS Workshop on Unstable and Turbulent Motion of Fluid.

[20] W.P. Krol, A.M. Annaswamy, and P.R. Bandyopadhyay. A biomimetic propulsor for active noise control: Theory. Technical Report 11,350, NUWC-NPT, February 2002.

[21] C.C. Lindsey. Form, function and locomotory habits in fish. *Fish Physiology*, VII:1–100, 1978.

[22] H.J. Lugt. *Introduction to Vortex Theory*. Vortex Flow Press, 1996.

[23] Munson, Young, and Okiishi. *Fundamentals of Fluid Mechanics*. John Wiley and Sons, 3 edition, 1998.

[24] J.N. Newman. *Marine Hydrodynamics*. The MIT Press, 1977.

[25] K. Okamoto, S. Nishio, T. Saga, and T. Kobayashi. Standard images for particle-image velocimetry. *Meas. Sci. Technology*, 11:685–691, 2000.

[26] Daniel F. Opila. Active control of underwater propulsor noise using polypyrrole conducting polymer actuators. Master's thesis, Massachusetts Institute of Technology, 2003.

[27] D.F. Opila, A.M. Annaswamy, W.P. Krol, and S. Raghu. Biomimetic reduction of wake deficit using tail articulation at low reynolds number. *IEEE Journal of Oceanic Engineering*, 29(3):766 – 776, July 2004.

[28] D.A. Read, F.S. Hover, and M.S. Triantafyllou. Forces on oscillating foils for propulsion and maneuvering. *Journal of Fluids and Structures*, (17):163–183, 2003.

[29] Donald Ross. *Mechanics of Underwater Noise*. Peninsula Publishing, 1987.

[30] J. K. Sveen. An introduction to matpiv v.1.6.1. Eprint no. 2, **ISSN** 0809-4403, Dept. of Mathematics, University of Oslo, 2004. http://www.math.uio.no/~jks/matpiv.

[31] D. Tang, D. Kholodar, J.N. Juand, and E.H Dowell. System identification and proper orthogonal decomposition method applied to unsteady aerodynamics. *AIAA*, 39(8):1569–1576, 2001.

[32] Graham K. Taylor, Robert L. Nudds, and Adrian L.R. Thomas. Flying and swimming animals cruise at a strouhal number tuned for high power efficiency. *Nature*, (425):707 – 711, October 2003.

[33] Elizabeth A. Thomson. Penguin boat plies the charles. *MIT Tech Talk*, 41(25), April 1997.

[34] M. Triantafyllou and G. Triantafyllou. An efficient swimming machine. *Scientific American*, 272:64–70, March 1995.

[35] J.J. Videler. *Fish Swimming.* Chapman and Hall, 1993.

[36] Daehyun Wee. Numerical modeling of vortex shedding in a biomimetic propulsor. Personal Correspondance, October 2004.

[37] J. Westerweel, D. Dabiri, and M. Gharib. The effect of a discrete window offset on the accuracy of cross-correlation analysis of digital piv recordings. *Experiments in Fluids*, 23:20–28, 1997.

[38] C. E. Willert and M. Gharib. Digital particle image velocimetry. *Experiments in Fluids*, 10:181–193, 1991.